Brigham Young University

BYU ScholarsArchive

2020-06-04

Electrochemical Sensors Enhanced by Convection and by 3D Arrays of Vertically Aligned Carbon Nanotubes

Benjamin James Brownlee
Brigham Young University

Follow this and additional works at: https://scholarsarchive.byu.edu/etd

Part of the Engineering Commons

Electrochemical Sensors Enhanced by Convection and by 3D Arrays of

Vertically Aligned Carbon Nanotubes

Benjamin James Brownlee

A dissertation submitted to the faculty of
Brigham Young University
in partial fulfillment of the requirements for the degree of

Doctor of Philosophy

Brian D. Iverson, Chair
Brian D. Jensen
Julie Crockett
John N. Harb
Richard K. Watt

Department of Mechanical Engineering

Brigham Young University

ABSTRACT

Electrochemical Sensors Enhanced by Convection and by 3D Arrays of
Vertically Aligned Carbon Nanotubes

Benjamin James Brownlee
Department of Mechanical Engineering, BYU
Doctor of Philosophy

Early and accessible diagnostics are important elements to reducing the negative side-effects of untreated disease. One key advancement in diagnostic monitoring is through the development of highly sensitive sensors that have the capability to detect lower concentrations, while still remaining accessible for point-of-care use. This dissertation characterizes electrochemical sensing platforms that are enhanced by convection and by 3D electrodes made from high surface area, vertically aligned carbon nanotubes (VACNTs).

Free-standing VACNTs were patterned into microchannel arrays for flow-through amperometric sensing. Convective mass transfer enhancement was shown to improve sensor performance in amperometric sensing through the use of high surface area to fluid volume structures and concentration boundary layer confinement. Through-flow sensing of hydrogen peroxide produced drastically higher signals than stirred sensing, with over 90% of the hydrogen peroxide being oxidized as it passed through the channels. Non-enzymatic sensing of glucose was achieved by chemical reaction of glucose with methyl viologen to produce on average 3.4 electrons per glucose molecule, significantly higher than that obtained with enzymatic sensing with glucose oxidase. A scaled down sensor enabled detection from 200 µL of glucose by flow injection analysis with a limit of detection of 360 nM and a linear sensing range up to at least 150 µM glucose. Such sensing range offers the potential to measure glucose levels found in saliva. This work demonstrates the utility of high aspect ratio electrodes made of VACNTs. Convection and surface area are shown to enhance the sensitivity of flow-through VACNT amperometric sensors by effectively utilizing the available analyte to increase the measured current density.

Advances in nanomaterials, combined with electrochemical impedance spectroscopy, have allowed impedimetric biosensors to have high sensitivity while remaining label-free, pushing towards enabling portable diagnosis at the point-of-care. Porous, 3D VACNT electrodes for impedance-based biosensing were fabricated with different electrode height, gap width, and configuration. Sensitivity was characterized by functionalizing the representative protein streptavidin onto VACNT electrodes for detection of biotin. Tall, closely-spaced VACNT interdigitated electrodes are shown to have the highest electroactive surface area (15x the 2D geometric area) and the highest sensitivity, allowing for a 1 ng/mL limit of detection. Aspect ratio and surface area are shown to be important factors in determining the sensitivity of 3D VACNT interdigitated electrodes for impedimetric sensing of biomolecules bound to electrode surfaces. Although this biosensing platform is shown with streptavidin and biotin, it could be extended to other proteins, antibodies, viruses, and bacteria.

Keywords: carbon nanotubes, electrochemical sensing, interdigitated electrode, flow sensing, convection

ACKNOWLEDGEMENTS

TABLE OF CONTENTS

LIST OF TABLES

LIST OF FIGURES

1   INTRODUCTION

1.1   Motivation

Quality of life is improved when people have control over their physical health. While certain efforts can be made for individuals to remain healthy, unexpected or prolonged diseases affect the lives of millions of people around the world. Diagnosis and monitoring of disease often requires laboratory equipment and expertise that limits accessibility and timeliness of results. Ongoing efforts are being made to expand access to diagnostic tools that allow quick and convenient results that enable people to better monitor their own health.

One prevalent example is that of diabetes mellitus, a metabolic disorder that is caused when glucose is not broken down by the body efficiently and levels of glucose in the blood stream rise. Over 400 million people have diabetes worldwide [1], and there exist many health risks involved if diabetes is not properly diagnosed and treated. Thus, early and accessible diagnostics are important in reducing the negative side-effects of untreated diabetes. The development of at-home glucose monitors (see Figure 1-1) has greatly enhanced the ability of diabetics to track their health, by having results easily accessible in their own home. Research to improve the traditional blood-prick test have resulted in alternative approaches such as continuous glucose monitoring [2] and non-intrusive monitoring methods [3]. Use of saliva as an accessible bodily fluid for glucose monitoring has been investigated as a non-intrusive way to monitor glucose levels [4]. However, the glucose concentration in saliva is significantly lower than that of blood, requiring a more

sensitive sensor than that used in a traditional glucose meter. Therefore, one path to providing accessible glucose monitoring could be through a sensor capable of detecting the concentrations of glucose found in saliva.

Figure 1-1: At-home glucose meter requiring a finger prick to measure the glucose concentration in blood [5].

Broadly speaking, one way to enable advances in diagnostic monitoring, including glucose monitoring, is to develop sensors with higher sensitivity that have the capability to detect lower concentrations. Using sensors for accurate, low concentration detection could potentially open the door for new diagnostic approaches and provide accessibility to key health monitoring information that would otherwise be difficult to obtain. A portable sensor with high sensitivity and fast results would be conducive for point-of-care use and allow people to more easily monitor their health.

1.2   Electrochemical Sensors

Sensors that detect biological species are often referred to as biosensors and can be classified as optical, thermal, piezoelectric, or electrochemical [6]. Optical sensors measure a change in absorbed or emitted light, thermal sensors measure a change in temperature, and

piezoelectric sensors measure a change in mass, each in response to a target analyte [7]. Each of these sensors have challenges and limitations; e.g., optical sensors may be impeded by turbid, optically dense or autofluorescent biological samples [8]. Electrochemical sensors react with a chemical solution to produce a measurable electrical signal or change that is proportional to the analyte concentration. Electrochemical sensors offer advantages such as good repeatability, affordability, ease of use, and digital output that allows measurement of concentration levels even in turbid solutions [9]. The modes of measurement for electrochemical sensors include amperometric, impedimetric/conductometric, potentiometric, and field effect [10]. Both amperometric and impedimetric electrochemical sensors are implemented in this dissertation and their function will be discussed further below.

1.2.1   Amperometric Sensors

Amperometry is the monitoring of electron transfer as measured by electrical current as a function of time. Amperometric sensors are typically used when a target analyte is able to electrochemically react at a sensing surface. Biological elements often need the aid of an enzyme to electrochemically react at the electrode surface. For example, traditional blood glucose sensors are amperometric sensors that use the enzyme glucose oxidase to convert glucose into hydrogen peroxide, which in turn reacts at the surface of the electrode and gives off two electrons measured as current. In this manner, the glucose concentration in a sample can quickly be determined and reported to a digital display.

An amperometric system typically has three electrodes (working, counter, and reference) in contact with an ion-conducting electrolyte. The electrodes are connected to a potentiostat which maintains a fixed potential between the working electrode and the reference electrode, while also measuring the electrical current that flows between the working electrode and the counter

3

electrode. The analyte of interest reacts at the surface of the working electrode, which is the driving force of amperometric sensors. The working electrode acts as an anode if analyte are oxidized at the surface (electrons taken by electrode), or as a cathode if analyte are reduced at the surface (electrons given by electrode). To oxidize an analyte, the potential at the working electrode surface must be above the equilibrium potential of the analyte.

A constant potential at the working electrode is applied relative to a known potential given by a reference electrode. A common reference electrode consists of silver (Ag) and silver chloride (AgCl), which react at a fixed potential within a saturated potassium chloride (KCl) solution. However, essentially no current passes between the working electrode and the reference electrode. Instead, current is passed from the working electrode through the potentiostat to the counter electrode to balance the change in the system. Current generated from the analyte at the working electrode is measured by the potentiostat and the change in current can be directly correlated with the concentration of analyte in solution.

1.2.2 Impedimetric Sensors

Impedimetric sensors can be used to detect analyte that may not electrochemically react, as it relies on molecules being bound to a sensing surface instead of generating current at the surface. An example application for impedimetric sensors is the diagnosis of cancer. The human body creates oncoproteins in response to the presence of cancer and detection of these proteins would be indicative that cancer exists in the patient. An impedimetric sensor could be used to detect a specific oncoprotein by selectively binding and holding these molecules at an electrode surface. The presence of these oncoproteins would cause a change in the impedance measured across a pair of electrodes, which change in impedance would indicate the presence of the targeted

oncoprotein. The magnitude of the change in impedance could be correlated to the concentration of the oncoprotein and could inform how advanced the cancer has progressed.

Electrochemical impedance spectroscopy (EIS) is used to measure changes in impedance rather than directly measuring changes in current (as for amperometric sensors). A sinusoidal AC potential with a small amplitude (typically 5-10 mV) is applied to the electrochemical system and the resulting magnitude and phase shift of the current are measured. The potential and current are used to calculate the overall impedance of the system (a complex number) at a specific frequency. A Nyquist plot can then be used to present impedance data from a range of frequencies, where the real component of impedance is plotted on the x-axis and the imaginary component of impedance is plotted on the y-axis.

The small input potential used during EIS produces a small current, such that two electrodes can be used without needing a third reference electrode. A reference electrode is mainly used to reduce variability in an electrode potential when conducting high amounts of current. It is, however, important that the two electrodes are close together. An example of an impedimetric electrochemical sensor is the interdigitated electrode (IDE) design with many fingers that alternate with the fingers of another electrode, creating an electrode array that exhibits low ohmic drops, high signal-to-noise ratios, and fast response times [11].

1.3   Convection

The current that is measured by amperometric sensors is directly proportional to the mass transfer rate (N), which can be calculated using Equation 1-1,

$$N = h_m A_s (C_s - C_\infty) \tag{1-1}$$

where h_m is the mass transfer coefficient, A_s is the electrode surface area, C_s is the surface concentration, and C_∞ is the bulk concentration. To increase the output signal from a sensor, one

5

must increase the mass transfer rate of analyte to the electrode by increasing the mass transfer coefficient and/or the surface area, as there is little control over concentration which is dependent on the sample being measured. Increasing surface area to increase the mass transfer rate using nanomaterials is an approach that has gained recent momentum and is discussed further in Section 1.4.

The mass transfer coefficient is related to the motion of the fluid around the sensor. As the motion of analyte is increased, the rate at which analyte comes into contact with the electrode surface also increases. A good example is a rotating disk electrode, where the introduction rate of analyte to the surface increases as the rotation rate increases [12]. Although this approach is straightforward, the impact of convection is often overlooked or its effect disregarded when stir speeds or flow rates are not provided with electrochemical or amperometric sensing results.

As opposed to increasing analyte flow, another approach is to use geometry to maintain analyte close to the electrode. For flow in a confined geometry such as a channel represented in Figure 1-2, concentration boundary layer growth is limited once the boundary layers have merged, resulting in a maximum transport distance of half the channel diameter. The mass transfer coefficient (h_m) for channel flow is given by Equation 1-2,

$$h_m = \frac{D \cdot Sh}{d_h}$$

(1-2)

where D is the mass diffusion coefficient, Sh is the Sherwood number, and d_h is the hydraulic diameter of the channel. The Sherwood number is a non-dimensional number analogous to the Nusselt number in heat transfer and is constant for fully-developed, laminar flow typical of microfluidics. Thus, the mass transfer coefficient can be increased when reducing the channel size. This is a key benefit of microfluidic systems, where very small channel diameters force close contact of analyte with the electrode surface and increase sensor sensitivity. The ability to use a

sensor in a microfluidic channel is also a feature that promotes point-of-care diagnosis, as microfluidics-based detection is easier, faster, and more convenient than traditional macroscopic platforms [13].
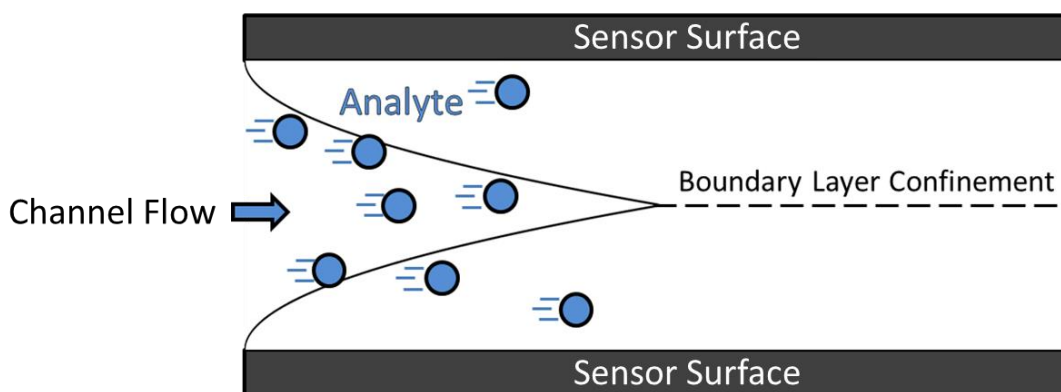
Figure 1-2: Schematic representation of flow within a channel where mass transfer is enhanced by limiting the growth of the concentration boundary layer.

While planar electrodes may be placed in channels to increase mass transfer, it is also possible to flow solution through channels or pores of the electrode itself. Such electrodes are known as flow-through electrodes and have origins in the 1970s [14-16], with application to hydrogen peroxide sensing beginning in the 1990s [17, 18]. Flow-through sensors take advantage of convection to more efficiently react analyte at the electrode surface. A flow-through array of microchannels was shown to be very effective at decomposing high concentrations of hydrogen peroxide for underwater vehicle propulsion [19]. With recent developments in microfabrication and materials science the ability to sense target analyte has greatly increased, yet most sensors have not taken advantage of flowing analyte through the sensor. Flow-through sensors also have the potential for flow injection analysis, which enables fast response times with much smaller sample volumes [20].

1.4   3D Nanomaterials

1.4.1   High Surface Area

With recent advances in nanomaterials, many electrochemical sensors have been able to greatly lower their detection limits. Microstructures such as three-dimensional (3D) graphene [21-23], magnesium oxide [24-26], and zeolites [27-29], all possess large surface area to volume ratios that allows for more analyte to interact with the electrode. Micro and nanostructured surfaces with increased electrode surface area have outperformed smooth, planar geometries [30, 31]. Metal and metal oxide nanoparticles [21], along with carbon nanomaterials such as carbon nanotubes (CNTs) [8, 32, 33], graphene [23, 34, 35], and graphene oxide [36] have been shown to be effective at increasing sensor sensitivity [37].

The high electrical conductivity, mechanical strength, and surface area of CNTs make them attractive as an electrode nanomaterial [38]. Many CNT sensors incorporate randomly dispersed CNTs that are cast on an electrode surface [39], but nanostructures grown from an electrode surface have been shown to offer greater stability and increased exposed surface area [40]. Particularly, vertically aligned carbon nanotubes (VACNTs) provide an ordered, preferential orientation of CNTs that are grown from the substrate. The high surface-area-to-volume ratio that comes from the 3D, porous VACNT electrodes can enable high protein capture capacity relative to planar electrodes, leading to the potential for improved sensitivity [41].

1.4.2   3D Structures

High aspect ratio geometries are possible through patterning VACNT forests, offering the potential for 3D, porous electrodes that may be exploited for concentration measurement of proteins, antibodies, or other molecules. Typical planar electrodes have a thickness that is on the

order of 10s to 100s of nanometers. While an electrode height (thickness) of a few micrometers may be considered 3D, patterned VACNTs offer the potential to increase the electrode thicknesses to greater than 100s of micrometers.

CNTs have previously been used with flow-through electrodes for electrochemical filtering [42] and for electrochemical sensing [43] by casting randomly oriented CNTs onto supporting membranes. A free-standing VACNT structure (without a supporting membrane) consisting of an array of micron-scale channels was used for the decomposition of hydrogen peroxide (H_2O_2) at high concentrations for underwater vehicle propulsion [19]. In this dissertation, a similar microchannel array made from VACNTs, as schematically represented in Figure 1-3A, is characterized for convection-enhanced amperometric electrochemical sensing.
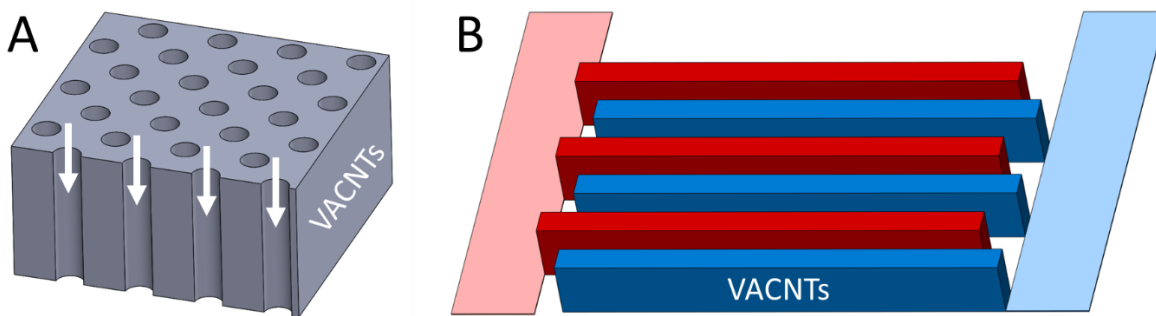
Figure 1-3: (A) Schematic representation of a flow-through electrode consisting of an array of microchannels. (B) Schematic representation of a 3D IDE with planar electrical leads.

VACNTs have also previously been used as IDEs for capacitors with VACNT heights ranging from $34 – 70$ µm with a $20 – 35$ µm gap between electrodes [44-46], but such tall heights have not been reported for electrochemical biosensors. Others have shown that an electrical connection can be made from VACNTs through an insulating aluminum oxide layer to an

underlying metallic electrical lead [47]. This approach offers a way to isolate electrical leads from the sensing region and enables access to the sensor when used within a microfluidic cavity. This dissertation presents 3D VACNT IDEs with underlying metallic electrical leads for impedimetric sensing, similar to Figure 1-3B.

1.4.3   Functionalization

Advances in nanomaterials have also led to improved functionalization capabilities of sensors. The ability to functionalize enzymes and proteins is one of the key ways that biosensors are able to detect a specific analyte. For sensing glucose, the enzyme glucose oxidase is typically bound to the electrode surface, and it has been shown that the functionalization technique greatly impacts the sensitivity, selectivity and longevity of such sensors [48]. Shi et al. have provided a comparison of functionalization methods for sol-gel encapsulation and glutaraldehyde cross-linking [49], but there lacks a comparison between different functionalization methods for high-aspect-ratio microstructures, where the functionalization needs to penetrate far beyond the easily accessible outer surface.

Non-enzymatic glucose sensors have risen in popularity due to their ease of manufacturing and because they do not have the same stability concerns common to enzymatic sensors [50]. Methyl viologen is a chemical that can chemically react with glucose (non-enzymatically) at a sufficiently high temperature and pH for potential use in fuel cell applications [51]. This same chemical reaction could also be used for glucose detection by correlating the oxidation of reduced methyl viologen to the glucose concentration.

For impedance-based sensors, a specific protein or antibody can be functionalized to the sensor electrode to allow further binding with a target analyte. Electrochemical impedance spectroscopy offers the potential for label-free and real-time detection of various analytes [52, 53].

10

Eliminating the need to label the analyte is another way that impedimetric biosensors enable diagnosis at the point-of-care.

1.5   Dissertation Organization

This dissertation characterizes electrochemical sensing platforms that are enhanced by convection and by 3D electrodes made from high surface area, vertically aligned carbon nanotubes (VACNTs).

Amperometric Sensors – Chapters 2 and 3 develop flow-through amperometric sensors made of VACNTs that form arrays of aligned, parallel microchannels. This VACNT architecture capitalizes on enhancing mass transport through high flow rate, large electroactive surface area, and concentration boundary layer confinement. Specifically, Chapter 2 experimentally compares traditional stirred environments and flow-through environments for sensing hydrogen peroxide. High sensitivity and a detection limit of 30 nM were made possible by flow-through sensing because over 90% of the hydrogen peroxide reacted as it passed through the VACNT channels. Chapter 3 builds upon the same sensor architecture using a unique non-enzymatic method for the detection of glucose with the chemical methyl viologen, which is compared to traditional enzymatic VACNT electrodes functionalized by different strategies. Sensors using methyl viologen have a higher sensitivity and are tested with a small flow cell, demonstrating the potential to measure glucose levels with 200 µL samples in the concentration range typical of saliva.

Impedimetric Sensors – Chapter 4 characterizes 3D VACNT electrodes with planar metallic electrical leads for impedimetric biosensing by measuring the change in electrochemical impedance with the protein streptavidin functionalized to the electrode for detection of biotin. VACNT height and electrode geometry are shown to influence biosensor sensitivity, with tall, closely-spaced IDEs having the highest sensitivity. Although the biosensing platform is shown

with streptavidin and biotin, it could be extended to other proteins, antibodies, viruses, and bacteria by functionalizing with another molecule with a selective binding mechanism.

Finally, Chapter 5 summarizes important conclusions from the dissertation and discusses potential future work. This work demonstrates the utility of high aspect ratio electrodes made of VACNTs. Convection and surface area are shown to play key roles in enhancing the sensitivity of flow-through VACNT amperometric sensors by increasing the measured current density for a given analyte concentration. Aspect ratio and surface area are shown to be important factors in determining the sensitivity of 3D VACNT interdigitated electrodes for impedimetric sensing of biomolecules bound to electrode surfaces.

2   IMPROVING SENSITIVITY OF ELECTROCHEMICAL SENSORS WITH CONVECTIVE TRANSPORT IN FREE-STANDING, CARBON NANOTUBE STRUCTURES

This chapter demonstrates the utility of high aspect ratio electrodes made of VACNTs. Convection and surface area were shown to play key roles in enhancing the sensitivity of flow-through VACNT amperometric sensors by increasing the measured current density for a given analyte concentration. Hydrogen peroxide was used to demonstrate sensor sensitivity improvement in flow-through environments which enable a low detection limit. This chapter is published in Sensors and Actuators B: Chemical [54] and the format has been modified here to meet the stylistic requirements of this dissertation.

2.1   Contributing Authors and Affiliations

Benjamin J. Brownlee, Kevin M. Marr, Jonathan C. Claussen,* and Brian D. Iverson

Department of Mechanical Engineering, Brigham Young University, Provo, UT, 84602

*Department of Mechanical Engineering, Iowa State University, Ames, IA, 50011

2.2   Abstract

High-aspect-ratio, porous membrane of vertically-aligned carbon nanotubes (CNTs) were developed through a templated microfabrication approach for electrochemical sensing. Nanostructured platinum (Pt) catalyst was deposited onto the CNTs with a facile, electroless

deposition method, resulting in a Pt-nanowire-coated, CNT sensor (PN-CNT). Convective mass transfer enhancement was shown to improve PN-CNT sensor performance in the non-enzymatic, amperometric sensing of hydrogen peroxide (H_2O_2). In particular, convective enhancement was achieved through the use of high surface area to fluid volume structures and concentration boundary layer confinement in a channel. Stir speed and sensor orientation especially influenced the measured current in stirred environments for sensors with through-channel diameters of 16 µm. Through-flow sensing produced drastically higher signals than stirred sensing with over 90% of the H_2O_2 being oxidized as it passed through the PN-CNT sensor, even for low concentrations in the range of 50 nM to 500 µM. This effective utilization of the analyte in detection demonstrates the utility of exploiting convection in electrochemical sensing. For through-flow at 100 µL s^{-1}, a sensitivity of 24,300 µA mM^{-1} cm^{-2} was achieved based on the frontal projected area (871 µA mM^{-1} cm^{-2} based on the nominal microchannel surface area), with a 0.03 µM limit of detection and a linear sensing range of 0.03-500 µM.

2.3   Introduction

Transport in chemical reactions can play a critical role in introducing reactants to or removing products from the surface where the reaction takes place. In fact, mass transport is cited as having a major influence on the performance of many chemical technologies, including chemical reactors [55-57], lithium-oxygen batteries [58], and fuel cells [59]. In sensor applications where the target analyte may occur in low concentrations, transport of the analyte to the reacting surface can be the primary limitation of the sensor approach (i.e. "transport-limited" sensors). With the prominent reduction in feature sizes and corresponding reduction in sensing surface area available with microelectromechanical systems, some sensor platforms can suffer from a significant limitation in mass transfer rates to the sensing surface (e.g. micro-cantilevers). In cases

where the analyte concentration is low, transport must be efficient to capitalize on the sparsely available target. Increasing the flow rate, increasing the surface area, and/or limiting growth of the concentration boundary layer are techniques that can be exploited to increase the convective transport of the analyte. This work demonstrates an effective platform to increase convective transport with applications in chemical sensing.

Enhancement of the analyte introduction rate can be achieved by increasing the flow rate of the analyte in solution. As the motion of the analyte is increased, the probability of analyte reaching a reacting surface increases and results in an overall increase in introduction rate. A good example of increased analyte flow is the rotating disk electrode, where the introduction rate of analyte to the surface increases as the rotation rate increases [12]. Several recent studies have also investigated catalytic structures which move through the analyte solution [60-65], thereby increasing the *apparent* analyte flow and enhancing the chemical introduction rate. Although this approach is straightforward, the impact of convection is often overlooked or its effect disregarded when stir speeds or flow rates are not provided with electrochemical or amperometric sensing results.

Enhancement of the analyte introduction rate can also be achieved for diffusive or convective environments by increasing the exposed catalytic surface area. High surface area microstructures promote intimate contact between the analyte and the catalytic surfaces while minimizing the structure's spatial footprint. Microstructures such as three-dimensional graphene [21-23], magnesium oxide [24-26], and zeolites [27-29], all possess considerably large surface area to fluid volume ratios and can be appropriately functionalized for specific chemical reactions. In particular, high-aspect-ratio microstructures (pillars, channels, *etc*.) allow for large exposure of surface area to chemical volume and facilitate enhanced mass transport, much in the same way fin

arrays are used to enhance heat transfer [66, 67]. The utility of enhanced surface area structures in the literature have been shown to outperform similar planar geometries [30, 31].

While external flow *past* microstructures can provide enhanced mass transport, internal flow *through* high-aspect-ratio microstructures allows for a third transport enhancement method: boundary layer confinement. For flow in a confined geometry such as a channel, concentration boundary layer growth is limited once the boundary layers have merged, resulting in a maximum transport distance of half the channel diameter. These short transport lengths result in high mass transport coefficients, especially as the channel diameter is reduced. The concept of flow-through electrodes originates in the 1970s [14-16], with application to hydrogen peroxide sensing beginning in the 1990s [17, 18]. However, with recent developments in microfabrication and materials science, the ability to sense target analyte has greatly increased, yet many sensors have not taken advantage of flowing analyte through the sensor. For example, carbon nanotubes (CNTs) have been widely used in electrochemical sensing because of their unique structural, mechanical, and electronic properties [68]. CNTs on supporting membranes have been used as flow-through electrodes for electrochemical filtering [42], but only recently have membrane-supported CNT flow-through electrodes been used for electrochemical sensing [43]. The present work describes a free-standing CNT sensor with an array of micron-scale channels (2,000-32,000 channels per mm^2), a structure we previously used for the decomposition of hydrogen peroxide (H_2O_2) at high concentrations for underwater vehicle propulsion [19]. Such a multi-channel CNT structure presents a departure from previous work as it is the first time CNTs have been arrayed in controlled patterns with flow through micron channels developed within the CNT membrane itself. Thus, this works presents the first steps in developing a more controlled CNT membrane for flow-through electrochemical microfluidic sensing devices (EMSDs) applications where the CNT membrane

itself acts *both* as the highly catalytic working electrode and as the structure used to induce tunable microfluidic transport. These multi-channel CNT structures could also be fitted and placed within various sized flow channels including conventional microfluidic channels.

The importance of microfluidic transport in the context of electrochemical sensing/biosensing has shown to be tremendous promising in achieving efficient catalysis and low detection limits [69]. Such microfluidic sensing devices produce fast analysis times with extremely low sample and reagent volumes which is well-suited for point-of-service detection that circumvents the costs associated with conventional laboratory analysis (e.g., shipping/handling costs, highly trained technicians to operate polymerase chain reaction (PCR) or perform enzyme-linked immunosorbent assays (ELISA) [70, 71]. Furthermore, EMSDs overcome challenges with optical-based sensing modalities where solution turbidity, optical path length, and power requirements can significantly hinder sensing results. However, there still exists a need to increase the sensitivity of EMSDs, and microfluidic sensors in general, as high sensitivity is required to detect target analytes in low concentrations or low volumes [72].

Herein, we increase the efficiency of electrochemical sensors that utilize convective flow environments by developing a high-aspect ratio, free-standing membrane (~250 μm height) of vertically aligned carbon nanotubes (CNTs) that form an array of aligned, parallel microchannels (of 4 μm diameter with 32,479 channels per mm^2 or of 16 μm diameter with 2,030 channels per mm^2). The overall sensor dimensions can be scaled up to accommodate macroscale flow cells or any specific EMSD dimension where the fluid flow can be forced through a series of sensing microchannels. Subsequently, this CNT architecture capitalizes on all three mass transport enhancement methods to improve electrochemical sensing: high flow rate, large electroactive surface area, and concentration boundary layer confinement. The sensor architecture is realized

through CNT-templated microfabrication, where CNTs are used as a scaffold to create a microporous membrane and achieve high-surface area to fluid volume structures that are electrically conductive. The structure is coated with urchin-like platinum nanowires (PN), developed through an electroless Pt deposition technique we have previously developed for use on CNTs, cellulose, and silicon oxide [19, 73, 74], to increase the CNT structures electrocatalytic capability during subsequent non-enzymatic, amperometric sensing of H_2O_2. Experiments reveal that stir speed and sensor orientation can greatly affect the current response of the PN-coated CNT (PN-CNT) sensors. Through-flow sensing (i.e., flow through the sensor architecture as would be experienced if the PN-CNT membranes spanned across the flow path of an EMSD) is shown to produce drastically higher signals at lower local fluid velocities than achieved with the traditional method of stirring. Further, we demonstrate near complete detection (>90%) of H_2O_2 at concentrations down to 50 nM through exploitation of the sensor geometry and convective enhancement. Therefore, the CNT sensing platform utilized here offers an efficient method for chemical sensing/biosensing and shows promise for incorporation into the flow field of EMSD and larger macroscale flow cells as portrayed in this work.

2.4 Materials and Methods

2.4.1 CNT Sensing Platform

Fabrication of the CNT sensing platform followed the methods outlined by Marr et al. [19] and is found in greater detail in Appendix A. An aluminum oxide (Al_2O_3) film approximately 50 nm thick was deposited on a silicon (Si) wafer using a Denton e-beam evaporator. A 7 nm layer of iron (Fe) was thermally evaporated onto patterned photoresist to achieve two different CNT sensor pore geometries (4 μm and 16 μm diameter microchannels). The wafer was agitated in N-

18

Methyl-2-pyrrolidone (NMP) for at least 10 minutes to remove the patterned photoresist in a lift-off process, resulting in a hexagonally packed arrangement of Fe free regions. The layers of construction for the CNT architecture are illustrated in Figure 2-1A.
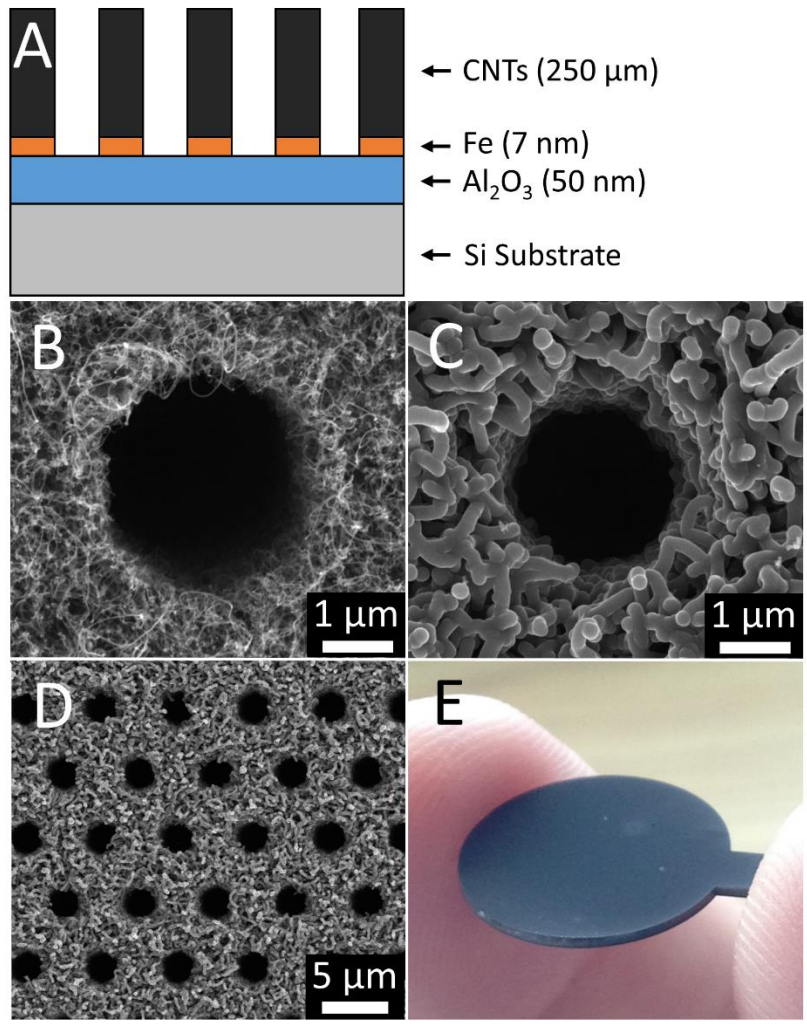
Figure 2-1: (A) Schematic of layers used to manufacture the CNT sensor architecture: Si, Al_2O_3, Fe, and CNTs. Scanning electron microscope (SEM) images of CNTs that form microchannels with a nominal 4 μm diameter (B) immediately after growth, (C) coated with amorphous carbon after infiltration, and (D) an array of porous-walled-microchannels aligned with the direction of the bulk CNT growth. (E) Sample CNT sensor after self-release from the Si substrate.

Diced Fe-patterned wafers were placed in a Lindberg/Blue M Tube Furnace for CNT growth in flowing hydrogen (230 sccm) and ethylene (250 sccm) at 750 °C for 6 minutes. After 6 minutes of growth, the multi-walled CNTs achieved a height of about 250 μm with diameters on the order of 20 nm (see Figure 2-1B), but require somewhat delicate handling. To create a stronger, agglomerated structure, the CNTs were coated (infiltrated) with amorphous carbon in the furnace by flowing hydrogen (158 sccm) and ethylene (250 sccm) at 900 °C for 10 minutes (see Figure 2-1C). This infiltration/coating process with amorphous carbon results in the attachment of neighboring CNTs and enables a mechanically robust yet porous array of microchannels (see Figure 2-1D). The hydrogen gas during carbon infiltration allows the CNT microstructure to self-release from the Si substrate, creating a stand-alone microstructure comprised of carbon-coated, CNT walls (see Figure 2-1E).

Although the CNT membranes self-released from the wafers, the side closest to the Si substrate was covered by a thin carbon layer during infiltration. To remove this layer, an oxygen (O_2) plasma etch was performed for 5 minutes in an Anelva Reactive Ion Etcher DEM-451 (300 W, 3.1 sccm O_2). An additional 2 minute etch was performed on the top face of the released structure to render the carbon surfaces hydrophilic.

2.4.2 Platinum Deposition

Platinum nanowires (PNs) were deposited onto the CNT sensors in a static, electroless environment using a chemical reduction of chloroplatinic acid hexahydrate (37.5% Pt, Sigma-Aldrich 206083) similar to our previous protocols [19, 73, 74]. The concentration used in each deposition was dependent on the mass of the CNT sensor, with a target of 30% Pt to carbon weight in solution (2.9 ± 0.4 mM chloroplatinic acid). Each CNT sensor was held vertically in a Teflon stand for 24 hours in a solution containing chloroplatinic acid, 18 mL of ultrapure water and 2 mL

of formic acid (88% HCOOH, Macron 2592-05). After the deposition, the samples were soaked in deionized water for 5 minutes and then placed in a dehydration oven for 10 minutes. The resulting Pt coverage on the CNTs is shown in Figure 2-2.
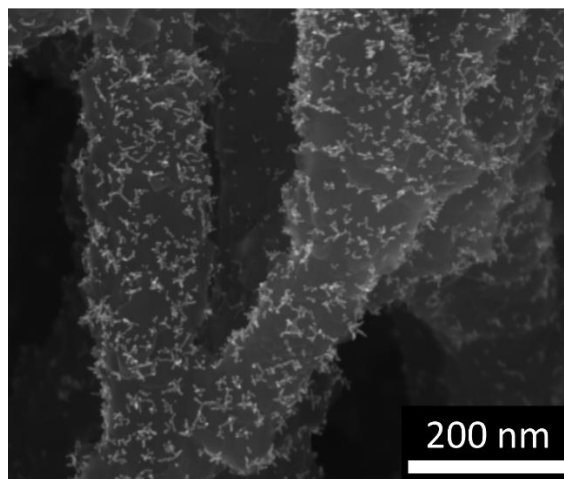
Figure 2-2: SEM image of Pt coverage on CNTs as found near the axial center of the microchannel.

2.4.3 Amperometric Measurements

All experiments were performed in a three-electrode electrochemical cell connected to a CHI 660 Potentiostat/Galvanostat. A Ag/AgCl reference electrode in saturated KCl, a Pt wire counter electrode, and the PN-CNT sensor as the working electrode were used. Amperometric sensing experiments were performed at a potential of 650 mV relative to Ag/AgCl. Before experiments were performed, this potential was applied to the buffer solution until a steady baseline current was achieved from the buffer solution alone.

Non-enzymatic amperometric sensing experiments were performed with H_2O_2 to illustrate the influence of convection and mass transfer on chemical sensing. Electrical current was produced from the oxidation reaction of H_2O_2, as shown in Equation 2-1.

$$H_2O_2 \rightarrow O_2 + 2H^+ + 2e^- \qquad\qquad (2\text{-}1)$$

Two electrons correspond to one molecule of oxidized H_2O_2, allowing the direct correlation between current and oxidation rate using the rate form of Faraday's law shown in Equation 2-2,

$$N = \frac{I}{nF} \qquad\qquad (2\text{-}2)$$

where N is the molar oxidation rate of H_2O_2 (mol s^{-1}), I is the current (A), n is the moles of electrons per mole of H_2O_2, and F is Faraday's constant, 96,485 C (mol e$^-$)$^{-1}$.

2.4.4   Stirred Environment

Stirred experiments were performed in a 50 mL glass beaker containing 30 mL of phosphate buffer saline (1X PBS, 7.4 pH, Fisher Scientific), as shown in Figure 2-3A and B. The PN-CNT sensor was positioned vertically, close to the water level, such that the circular portion of the sensor was completely submerged, but the connecting tab (attached to Nichrome wire with Duralco 120 silver epoxy) was not submerged. Two orientations were examined: the PN-CNT sensor positioned parallel to the flow (Figure 2-3A) and perpendicular to the flow (Figure 2-3B). An 8 mm diameter stir bar (2.5 cm in length) at the bottom of the beaker provided the fluid motion using a Thermo Scientific Super-Nuova stir plate to control the stir speeds. The concentration of H_2O_2 did not change significantly during each test, except as noted in section 2.6.2.

2.4.5   Through-flow Environment

In through-flow experiments, 50 mL of PBS (same as in stirred experiments) was forced through the PN-CNT microchannels. The PN-CNT sensor was clamped together between two O-rings in a machined Teflon electrochemical flow cell, shown in the exploded view in Figure 2-3C. This configuration allowed forced mechanical contact between the sensor and a Nichrome wire

(avoiding the need for silver epoxy used in stirred experiments). The flow cell was oriented vertically, with the reference electrode upstream and the counter electrode downstream of the PN-CNT sensor. This configuration provided the greatest response to hydrogen peroxide, while still providing low background noise. A 60 mL syringe pulled the solution through the cell from a reservoir on the opposite side using a Harvard Apparatus PHD Ultra syringe pump to control the flow rate.
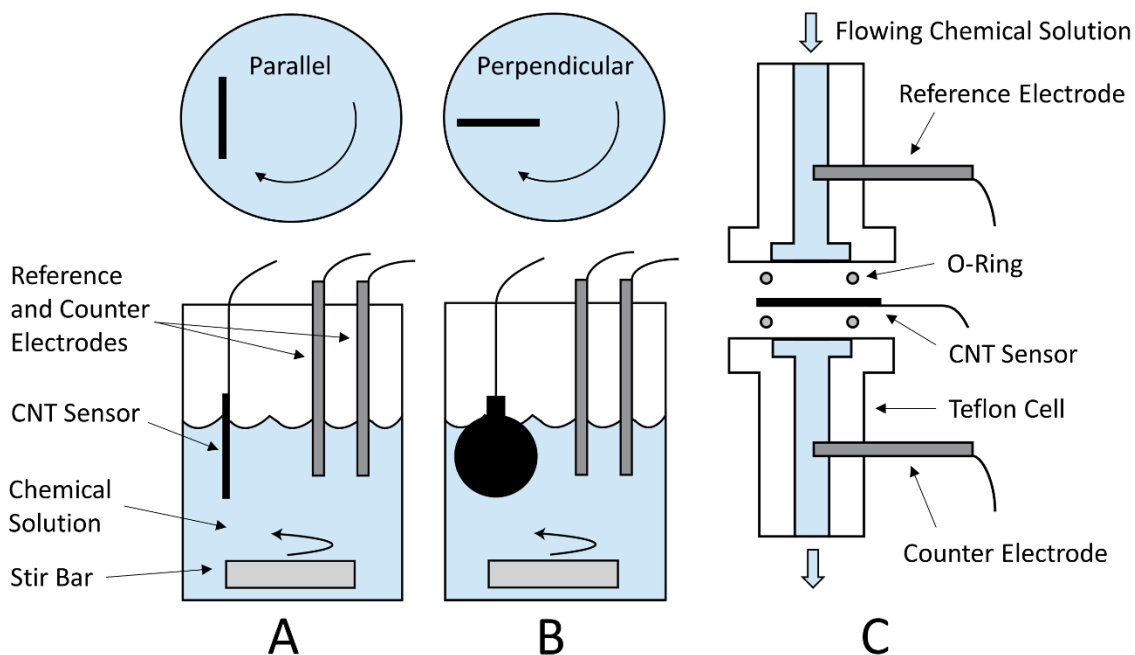
Figure 2-3: Schematics of different convective environments tested using three electrode cells. Stirred conditions with the PN-CNT sensor oriented (A) parallel to flow and (B) perpendicular to flow. (C) Exploded view of through-flow conditions, where the chemical solution is forced through the PN-CNT microchannels.

2.5   Results

2.5.1   Characterization

The PN-CNT sensors were 260 ± 48 μm in thickness, yielding aspect ratios (channel length/diameter) of about 16 and 65 for the 16 and 4 μm diameter channels, respectively. The sensors had a frontal projected area of 1.56 cm^2 (1.41 cm diameter), with both geometries having the same void fraction of 0.413. The surface area for a solid disk of this diameter and thickness would be 3.25 cm^2. With 4 μm channels passing through the disk, the nominal microchannel surface area would increase to 169 cm^2. Since the microstructure is also porous, the actual surface area is significantly higher. A Brunauer–Emmett–Teller (BET) nitrogen absorption test yielded 19.86 m^2 g^{-1} for the CNT sensors. Thus, for a nominal sample mass of 24.5 ± 3.6 mg, the surface area would be 4,621 ± 679 cm^2, or a 1,400 times increase over the nominal solid disk.

The CNT membranes had PNs deposited on the surfaces, resulting in a 13.1 ± 3.9 Pt to carbon weight percent. PNs coverage was highest on the outer surfaces and became more sparse toward the axial center of the channels (see also [19]).

2.5.2   Stirred Results

Figure 2-4A shows the current response in time from a typical set of experiments, where three repeat stirred experiments are shown for the 16 μm channel CNT geometry in the parallel orientation. The baseline currents for different stir speeds (0 (static), 50, 100, 200, 300 rpm) were monitored in one minute intervals. At 300 seconds, 3% H_2O_2 by weight (0.89 M H_2O_2) was added to the cell to obtain a target concentration of 100 μM H_2O_2. This injection of H_2O_2 caused an immediate spike in measured current, which was monitored for three minutes (see central plateau

region of Figure 2-4A and Figure 2-4B). Then, the same stir speeds were stepped through in reverse

order over one minute intervals until the cell returned to a static condition.
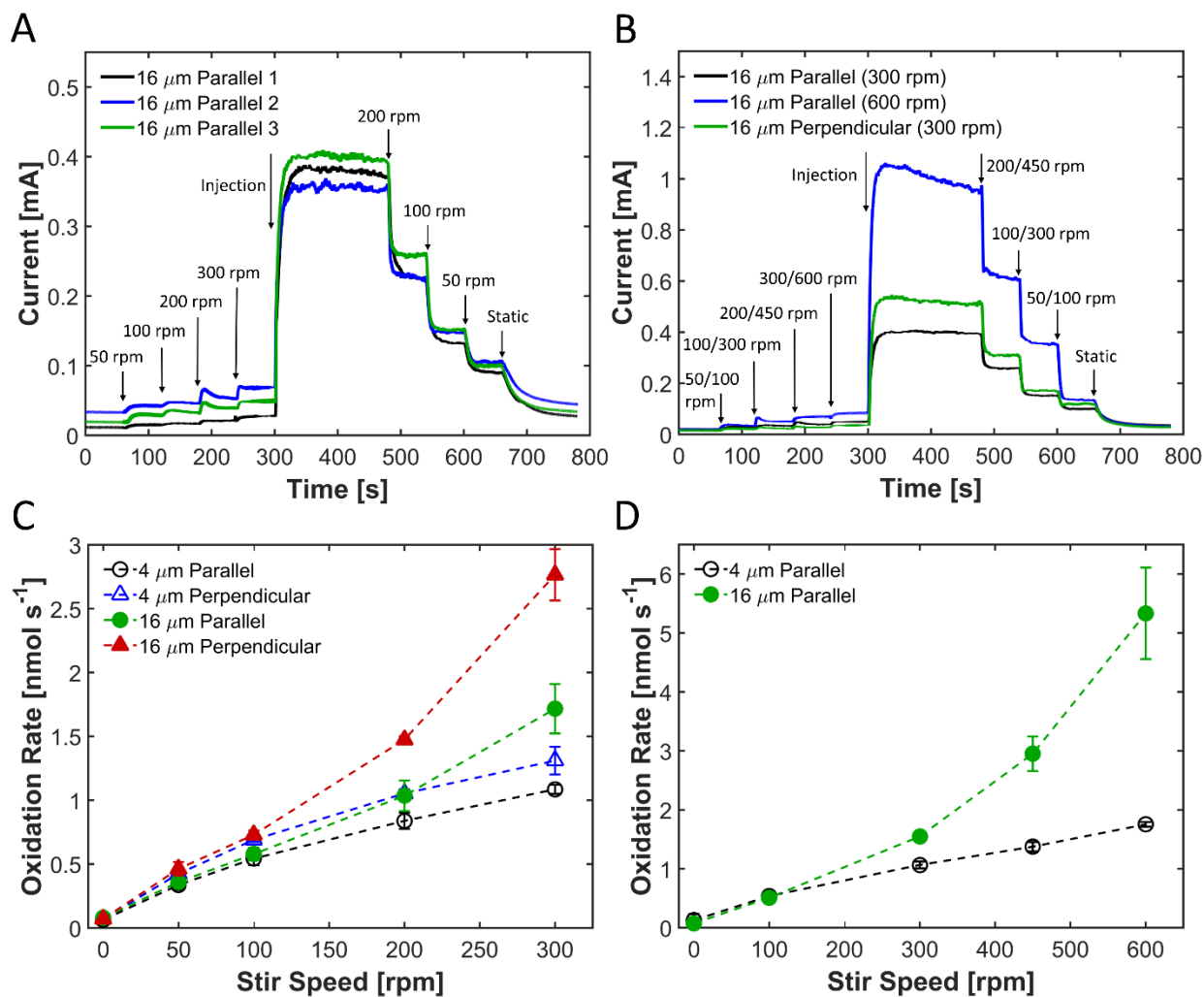
Figure 2-4: (A) Measured current for three separate 16 μm diameter PN-CNT sensors in response to an injection of 100 μM H_2O_2 for different stir speeds. The sensor is oriented parallel to the flow, with the injection of H_2O_2 at 300 seconds is monitored for 3 minutes (central plateau region) while stirring at 300 rpm, after which the stir speed is incrementally lowered, as indicated. (B) Comparison of current response for sample PN-CNT sensors in the parallel orientation (up to 300 rpm and 600 rpm) and in the perpendicular orientation (up to 300 rpm). The first/second indicated stir speeds correspond to testing up to a max stir speed of 300/600 rpm, respectively. (C) Oxidation rates in response to 100 μM H_2O_2 at various stir speeds for parallel and perpendicular sensor orientations with 4 and 16 μm diameter channels relative to the flow. (D) Oxidation rates for the parallel orientation up to 600 rpm for both 4 and 16 μm diameter geometries. In all cases, error bars represent the standard deviation of three measurements.

The results of the parallel orientation from Figure 2-4A were compared to two other stirred environments using the same PN-CNT sensors (16 µm diameter channels) in 100 µM H_2O_2 (see Figure 2-4B). In the first comparison, the PN-CNT sensor was oriented perpendicular to the flow and tested at the same stir speeds (0 (static), 50, 100, 200, 300 rpm). The second comparison considered stir speeds up to 600 rpm (0 (static), 100, 300, 450, and 600 rpm) in the parallel orientation. Both of these comparison conditions gave higher currents than the parallel orientation up to 300 rpm; however, at 600 rpm the measured current appears to decrease by 13% due to a change in the solution concentration, as discussed further in section 2.6.2. Tests were not performed in the perpendicular orientation at 600 rpm due to the strain it placed on the PN-CNT sensor.

It can be seen from Figure 2-4A and B that the measured current was strongly dependent on stir speed, with the highest current achieved at the highest tested stir speed. The current changed suddenly with each reduction in stir speed, showing a strong correlation between the convective environment and the measured current.

For each stir speed, orientation, and channel diameter, the change in current before and after the H_2O_2 injection was used to calculate the oxidation rate of H_2O_2 (see Equation 2-2). A comparison between the oxidation rates for the parallel and perpendicular orientations up to 300 rpm for the 4 and 16 µm diameter geometries is shown in Figure 2-4C. In all cases, three separate CNT sensors were tested for each geometry to obtain the standard deviation of the response. At 100 rpm and lower, the differences in oxidation rates between the different orientations and geometries are minimal. However, as stir speed increases to 300 rpm, the 16 µm sensors have higher oxidation rates, especially in the perpendicular orientation. For both channel diameter sizes, the perpendicular orientation gave higher oxidation rates than the parallel orientation. This

indicates that stir speed, orientation and pore size (channel diameter) all influence the current response of a sensor.

Figure 2-4D shows how oxidation rate increases with stir speed (up to 600 rpm) in the parallel orientation for both channel diameters. The oxidation rates for the 4 μm diameter geometry appear to increase nearly linearly with stir speed after 100 rpm. However, a non-linear increase in oxidation rate with stir speed for the 16 μm diameter geometry is observed. At 600 rpm, the oxidation rate of the 16 μm sensor was about 3 times that of the 4 μm sensor. The oxidation rate of the 16 μm sensor also increased nearly 3 times when stir speed was doubled from 200 to 300 rpm.

2.5.3   Through-Flow Results

To maximize the surface area of the PN-CNT sensor and to utilize boundary layer confinement, all the chemical solution was forced through the microchannels in a through-flow, convective environment (see Figure 2-3C). The current densities for the 16 μm geometry in response to 100 μM H_2O_2 at different flow rates (10, 25, 50, 75, and 100 μL s^{-1}) are shown in Figure 2-5A.

Current densities (which are normalized by area) are used in Figure 2-5A to compare stirred and through-flow results because part of the frontal sensor area is outside of the O-ring used to seal the flow path in the through-flow arrangement. The stirred current is normalized by the frontal projected surface area (1.56 cm^2) and the through-flow current is normalized by the area defined by the inner diameter of the O-rings (0.713 cm^2).

The currents measured in through-flow arrangement were significantly higher than currents obtained in the stirred experiments because the microchannels kept the H_2O_2 close to the surface

(where the reaction takes place), limiting the concentration boundary layer. The volumetric flow rate was a dominant controlling feature of the measured current, as there are sharp drops in current when the flow rate was lowered. The oscillations in the current observed after the injection of H_2O_2 (Figure 2-5A, red curve after 300 seconds) correspond to the frequency of stepping in the syringe pump. This sensitivity to stepping in the syringe pump motor further indicates the dependence of the measured current on the convective environment, as slight changes in the flow rate caused by the syringe pump resulted in signal oscillations.
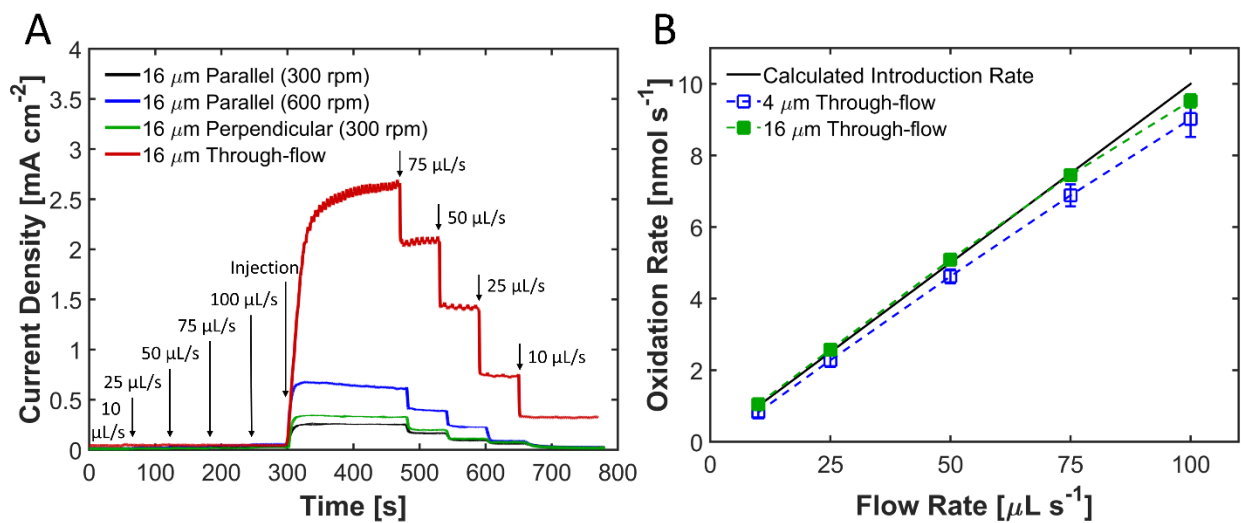
Figure 2-5: (A) Through-flow current densities for the 16 µm diameter channels in response to 100 µM H_2O_2 (injected at 300 seconds and measured for 180 seconds) at different flow rates (10-100 µL s^{-1}) as compared to the current densities of the various stirred conditions for the same concentration of H_2O_2 (previously illustrated in Figure 2-4B). (B) Through-flow oxidation rates in response to 100 µM H_2O_2 at different flow rates for both 4 and 16 µm diameter channels are compared to the calculated introduction rates of H_2O_2. Error bars represent the standard deviation of three measurements.

The measured oxidation rates for the through-flow experiments are shown in Figure 2-5B, where three PN-CNT sensors were again used for each geometry to obtain the standard deviation of the response. These oxidation rates are compared to the calculated introduction rates of H_2O_2

into the flow cell, which were determined from the known concentration of H_2O_2 and the volumetric flow rates. The introduction rate is the theoretical maximum oxidation rate at any given flow rate. The 16 μm channel geometry obtained oxidation rates that were nearly identical to the introduction rates (with a slight drop to 95% at 100 μL s^{-1}). This signifies that nearly all the H_2O_2 was oxidized as it passed through the PN-CNT sensor and correlates well with simulated predictions of the concentration profile throughout the channel, as shown in Appendix B. The 4 μm diameter channels had slightly lower oxidation rates at about 90% of the introduction rate. Oxidation rates for both geometries appeared to increase linearly with flow rate.

2.5.4 Through-Flow Sensitivity, Limit of Detection and Linear Range

The 16 μm diameter PN-CNT sensor at a flow rate of 100 μL s^{-1} provided the highest oxidation rate when tested at 100 μM H_2O_2. Therefore, this geometry and convective environment were chosen to determine the sensitivity, limit of detection (LOD) and linear range for the sensor approach. Figure 2-6A-C shows the complete linear range of the PN-CNT sensor, in the range of 50 nM to 500 μM, with the oxidation rates remaining linear over about 90% of the introduction rates.

The linear range can be seen at lower concentrations in Figure 2-6B and at very low concentrations in Figure 2-6C. The measured oxidation rates are very close to the introduction rates at these low concentrations, which is particularly useful in the detection of very low concentrations where it is desired to maximize the signal from the available analyte. Figure 2-6D shows the current measured in time for the oxidation rates shown in Figure 2-6C, at increments of 50 nM. The limit of detection (LOD) at 100 μL s^{-1} was 0.03 μM (using a signal to noise ratio of S/N = 3). Thus, Figure 2-6C shows that the PN-CNT sensor is approaching the LOD while still remaining very linear. The linear range is then 0.03 – 500 μM.
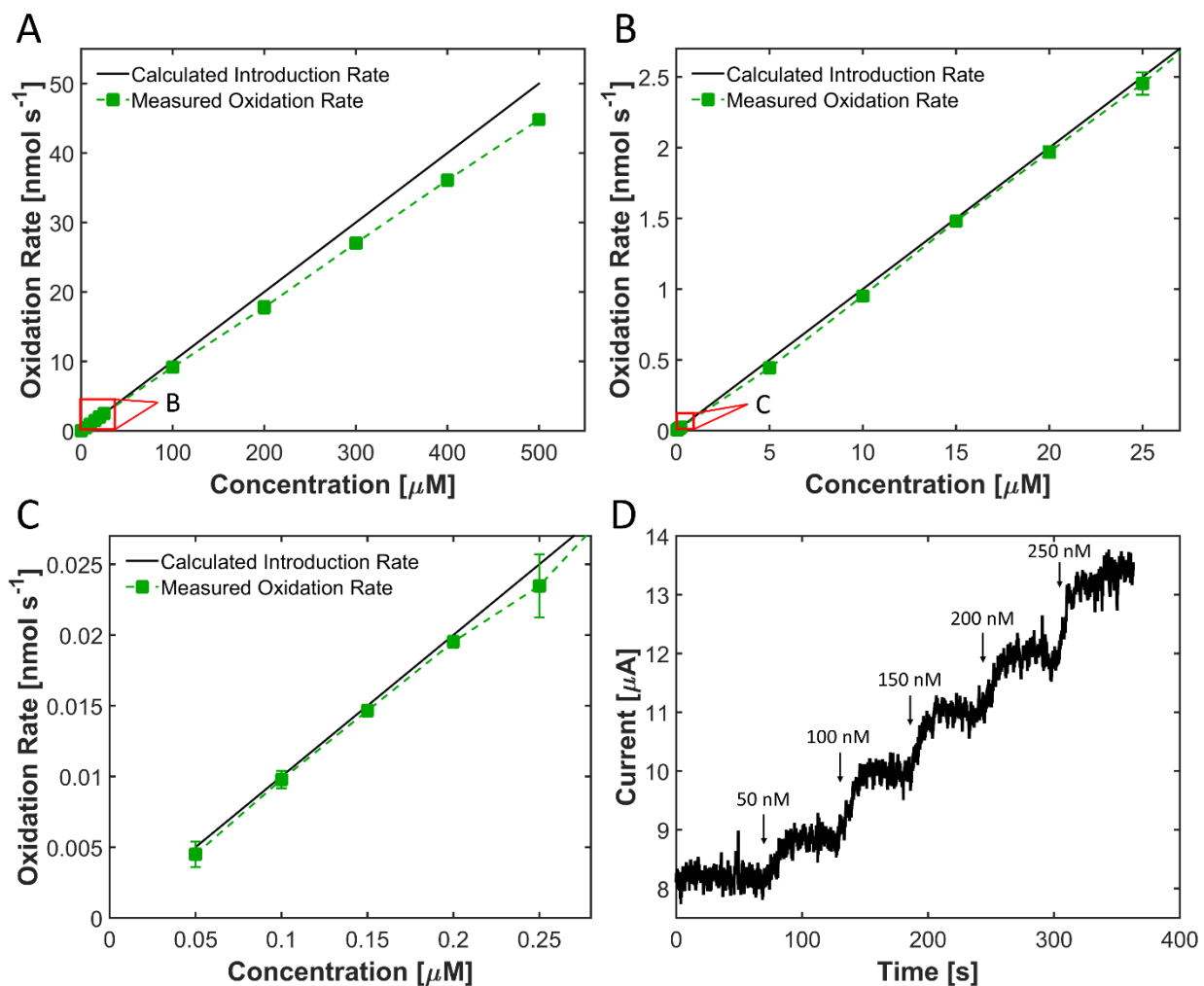
Figure 2-6: (A) Linear range of 16 µm diameter PN-CNT sensor at a flow rate of 100 µL s^{-1}. (B) Close up linear range of (A) up to 25 µM. (C) Close up linear range of (B) up to 0.25 µM. This linear range is approaching the limit of detection of 0.03 µM. (D) The current measured in time for additions of 50 nM H_2O_2, which were used to determine the oxidation rates obtained in (C). In all cases, error bars represent the standard deviation of three measurements.

The sensitivity (current/molarity) of the PN-CNT sensor was determined to be 17,300 µA mM^{-1}. Normalizing by the 2D surface area similar to other researchers (frontal projected area = 0.713 cm^2) gives a sensitivity of 24,300 µA mM^{-1} cm^{-2}. This is an extremely high sensitivity as noted in Table 2-1. If one were to include the nominal microchannel surface area in the normalization (19.86 cm^2), a sensitivity of 871 µA mM^{-1} cm^{-2} would be obtained. Table 2-1 shows

a comparison of sensitivity with some recent Pt-based, non-enzymatic H_2O_2 sensors with our sensitivity ranking among some of the highest reported, regardless of the method for normalizing with area. Four electrodes (including the one in this work) are marked with an asterisk in the table to indicate that they were tested in channel flow. Generally speaking, the sensitivity of these electrodes in a flowing environment was significantly higher than other electrodes in the table, likely due to enhanced mass transfer through convective channel flow. The PN-CNT sensor also had a lower LOD than all but four of the sensors, but only two of those sensors remained linear near the limit of detection.

Table 2-1: Sensitivity, limit of detection (LOD), and linear sensing range comparison with recent Pt-based, non-enzymatic H_2O_2 sensors.

Electrode	Potential (V (Ag/AgCl))	Sensitivity ($\mu A\ mM^{-1}\ cm^{-2}$)	LOD (μM)	Linear Range (μM)	Reference
CV-activated Pt-black*	0.3	4,080	0.01	0.01-300	[75]
Pt strips*	-	-	0.41	-	[76]
Pt/Te-microtubes*	-0.15**	2,000	0.001	0.5-30,000	[77]
SPGFE/MWCNTC/PtNP	-0.4	-	1.23	5–2,000	[78]
PtPd-MWCNTs	0.65**	393	8	12–14,000	[79]
PVA–MWCNTs–PtNPs	0	122.63	0.7	2–3,800	[80]
CoNP–Pt/CNTs	-0.15**	744	0.1	0.2–1,250	[81]
MWCNTs/Pt nanohybrids	0	205.8	0.3	10–2,000	[82]
PtNPs/MWCNTs–SDS	-0.05**	-	0.0019	0.0058–1,100	[83]
Pt hierarchical nanoflower	0.21	1,390	0.32	10–400	[84]
Pt/graphene–CNT paper	-0.05	1,410	0.01	0.1–25	[85]
Fe@Pt/C	-0.35**	218.97	0.75	2.5–41,600	[86]
aHPM	0.8	-	1.69	0.87–167	[87]
PN-CNT microchannels*	0.65	24,300[†] / 871[§]	0.03	0.03–500	This work

*Convection enhanced via channel flow

** potential converted from saturated calomel electrode (SCE) to Ag/AgCl reference electrode (about 0.05 V increase)

† based on frontal projected surface area

§ based on nominal microchannel surface area

2.6   Discussion

2.6.1   Influence of Convection

The results for stirred and through-flow configurations have shown the significant impact of convection on sensing platforms. The signal strength obtained in traditional three-electrode cell configurations can be highly dependent on stir speed and orientation. Although others have shown that covering a sensor with a membrane may reduce the influence of stir speed [87], the influence of convection should generally not be ignored. As such, stir speed and orientation should be reported when amperometric results are presented.

It is likely that both the 4 and 16 μm diameter sensors demonstrated higher oxidation rates in the perpendicular orientation because the flow acted as an impinging jet, increasing the mass transfer coefficient when compared to flow parallel to the sensor. The sensor with 16 μm diameter channels offered oxidation rates that were significantly higher than the 4 μm sensor in the perpendicular orientation, likely because the H_2O_2 solution more easily penetrated into the microchannels, taking advantage of additional surface area and increasing the oxidation rate. The 4 μm channels may be too small to allow the solution to easily enter the channels when stirring, limiting the reaction only to the outer surfaces of the sensor. Further, it is likely that the smaller diameter sensors have a lower amount of Pt deposition inside the microchannel area, as the deposition method is diffusion dominated.

Similarly, the observed non-linear increase in oxidation rate with stir speed for the 16 μm sensors in both the parallel and perpendicular orientations may be caused by an increase in the amount of solution that enters the channels. Thus, the oxidation rates of porous sensors with the larger microchannel diameters appear to be more sensitive to changes in stir speed and orientation.

It was also shown that flowing the chemical solution through the PN-CNT sensor greatly increased the oxidation rates when compared to stirred conditions. Not only were the oxidation rates much higher for through-flow conditions, these higher oxidation rates were achieved at significantly lower local velocities than the stirred environments. For the maximum flow rate of 100 μL s^{-1}, the average velocity through the microchannels was only 0.34 cm s^{-1}. For the maximum stir speed of 600 rpm (assuming the velocity of the fluid past the sensor to be approximated by the local velocity of the stir bar; see Appendix C for a more detailed look into the stirred velocity profile) the velocity was 62.8 cm s^{-1}. Thus, the relative fluid velocity at 100 μL s^{-1} was only about 0.55% the velocity at 600 rpm, while still achieving nearly double the oxidation rate with less than half of the surface area. The drastic improvement in measurement signal for the through-flow configuration, relative to a stirred condition, is due to the intimate contact between analyte and sensing surface achieved through limiting the concentration boundary layer by forcing the liquid through the sensor architecture.

A lower fluid velocity in through-flow sensing may also provide less noise in the signal relative to stirred conditions. In stirred experiments, it was observed that the baseline current increased with increasing stir speeds, despite reducing the buffer solution for more than 30 minutes. In through-flow testing, there was a slight increase in baseline current from static to flowing buffer solution before H_2O_2 injection, possibly caused by a streaming current from flowing solution through the PN-CNT sensor. However, the baseline current remained nearly constant when increasing from 10 to 100 μL s^{-1} in through-flow (Fig. 5A), suggesting the effects of a streaming current were negligible. Regardless, the current response was determined by subtracting the baseline current for the buffer solution from the measured current after H_2O_2 injection at the same flowrate, thereby removing any effect of streaming current from the buffer solution. The increase

in current from static to 600 rpm before injecting H_2O_2 was about 6% of the measured step change at 600 rpm for 100 µM H_2O_2, while the slight increase in current from 10 to 100 µL s^{-1} before injecting H_2O_2 was only 0.2% of the measured step change at 100 µL s^{-1} for 100 µM H_2O_2.

2.6.2   Concentration Change in Time

It should be noted that the concentration of H_2O_2 reduced in time over the duration of the stirred experiments. This was most noticeable with the 16 µm diameter sensor at 600 rpm, as seen by the downward slope in the current after the injection of H_2O_2 (see Figure 2-4B). Three minutes after the injection of H_2O_2, the measured current dropped approximately 13%. In contrast, the measured current of the 4 µm diameter sensors at 600 rpm only dropped by about 4% after three minutes because the oxidation rate was only one third the oxidation rate of the 16 µm diameter sensors.

In a through-flow environment, the H_2O_2 concentration upstream of the PN-CNT sensor does not change in time because the oxidized solution moves through the sensor, such that the current does not decrease in time at a constant flow rate. This allows for very high oxidation rates without having to correct for concentrations changing in time.

2.6.3   Limitations

A major factor that limited the upper end of the sensing range was the formation of oxygen bubbles due to the high oxidation rates of H_2O_2 (see Equation 2-1). Because the experiments were performed by withdrawing the syringe pump, the resulting bubbles in the liquid line had the potential to cause discontinuity in the measured signal. An alternative approach would be to perform the experiments with infusion pumping, such that the generated gases are swept toward a free surface and do not obstruct the signal at high H_2O_2 concentrations.

The detection limit of the PN-CNT sensor could potentially be improved by increasing the flow rate above 100 µL s^{-1} to obtain higher current responses for the same H_2O_2 concentration. It appeared that slight variations in the Pt coverage had little effect on the sensor signal; however, samples without Pt had a very low response with <2% of the measured oxidation rate for PN-CNT sensors at 100 µL s^{-1} (see Figure D-1 in Appendix D).

2.7   Conclusions

This work highlights the utility of convection in detecting low analyte concentrations. The approaches to exploit the use of convection help to increase the sensitivity of electrochemical sensors incorporated into microfluidic devices. In particular, we have shown how high-aspect-ratio PN-CNT sensors provide a unique sensing platform that enhances mass transfer by enabling high flow rates and surface area, and confining concentration boundary layers. PN-CNT sensor performance was measured by the non-enzymatic amperometric sensing of H_2O_2, where it was shown that convection had a significant influence on the measured current. Stir speed and sensor orientation were two factors that affected sensors in stirred environments, especially for those with microchannel diameters of 16 µm. Through-flow sensing oxidized over 90% of the H_2O_2 as it passed through the PN-CNT sensor, producing drastically higher currents at lower velocities than stirring. The high current response obtained by flow through the PN-CNT microchannels resulted in a very high sensitivity, allowing for the detection of analyte concentrations in the nM range. Overall dimensions of the PN-CNT sensor used in this work could be scaled to accommodate the flow field dimensions of a microfluidic sensing device, allowing for the analysis of very small fluid volumes and providing an efficient method for chemical sensing. Moreover, the height, pore diameter and shape (porosity) of the microchannels within the CNT structures could be tailored for distinct sensing applications (e.g. high vs. low fluid flow environments, conjugation with

biorecognition agents of distinct size/molecular weight within the CNT microchannels). Such

further tuning of these microchannel CNT structures is reserved for future work.

3 ELECTROCHEMICAL GLUCOSE SENSORS ENHANCED BY METHYL VIOLOGEN AND VERTICALLY ALIGNED CARBON NANOTUBE CHANNELS

This chapter demonstrates the utility of high aspect ratio electrodes made of VACNTs for glucose detection using a similar flow-through VACNT structure as in Chapter 2. Convection and surface area played key roles in enhancing the sensitivity of the amperometric glucose sensors by increasing the measured current density. This chapter investigates a unique non-enzymatic method for the detection or utilization of glucose with the chemical methyl viologen, which was shown to offer higher sensitivity than traditional enzymatic VACNT electrodes. This chapter is published in ACS Applied Materials and Interfaces [88] and the format has been modified here to meet the stylistic requirements of this dissertation.

3.1 Contributing Authors and Affiliations

Benjamin J. Brownlee, Meisam Bahari, John N. Harb, Jonathan C. Claussen*, and Brian D. Iverson

Department of Mechanical Engineering and Department of Chemical Engineering, Brigham Young University, Provo, UT, 84602

*Department of Mechanical Engineering, Iowa State University, Ames, IA, 50011

3.2 Abstract

Free-standing, vertically aligned carbon nanotubes (VACNTs) were patterned into 16 μm diameter microchannel arrays for flow-through electrochemical glucose sensing. Non-enzymatic sensing of glucose was achieved by the chemical reaction of glucose with methyl viologen (MV) at an elevated temperature and pH (0.1 M NaOH), followed by the electrochemical reaction of reduced-MV with the VACNT surface. The MV sensor required no functionalization (including no metal) and was able to produce on average 3.4 electrons per glucose molecule. The current density of the MV sensor was linear with both flow rate and glucose concentration. Challenges with interference chemicals were mitigated by operating at a low potential of -0.2 V vs. Ag/AgCl. As a comparison, enzymatic VACNT sensors with platinum nano-urchins were functionalized with glucose oxidase by covalent binding (EDC/NHS) or by polymer entrapment (PEDOT) and operated in phosphate buffered saline (PBS). With normalization by the overall cross-sectional area of the flow (0.713 cm^2), the sensitivity of the MV, enzyme-in-solution, and covalent sensors were 45.93, 18.77, and 1.815 mA cm^{-2} mM^{-1}, respectively. Corresponding limits of detection were 100, 194, and 311 nM glucose. The linear sensing ranges for the sensors were: 250 nM – 200 μM glucose for the MV sensor, 500 nM – 200 μM glucose for the enzyme-in-solution sensor, and 1 μM – 6 mM glucose for the covalent sensor. The flow cell and sensor cross-sectional area were scaled down (0.020 cm^2) to enable detection from 200 μL of glucose with MV by flow injection analysis (FIA). The sensitivity of the small MV sensor was 5.002 mA cm^{-2} mM^{-1}, with a limit of detection of 360 nM glucose and a linear range up to at least 150 μM glucose. The small MV sensor has the potential to measure glucose levels found in 200 μL of saliva.

3.3   Introduction

With recent advances in nanomaterials, many glucose sensors have been able to greatly lower their detection limits. Metal and metal oxide nanoparticles [21], along with carbon nanomaterials such as carbon nanotubes (CNTs) [8, 32, 33], graphene [23, 34, 35], and graphene oxide [36] have been shown to be effective at increasing sensor sensitivity [37]. CNTs are favorable for electrochemical sensing because of their high surface area, mechanical strength and electrical conductivity [38]. Many sensors incorporate randomly dispersed nanomaterials (including CNTs) that are cast on an electrode surface [39]. This often requires the use of binders resulting in densely packed nanostructures with poor mechanical stability [89]. Nanostructures grown from an electrode surface, such as nanorods, have been shown to have greater stability, while allowing for greater exposed surface area [40]. In a similar fashion, vertically aligned carbon nanotubes (VACNTs) provide an ordered, preferential orientation of CNTs with high surface area to volume ratio enabling high sensitivity. Glucose sensors are often electrochemically based, which offers good repeatability, affordability, and ease of use as concentration levels can be quantified even in turbid solutions with a digital output [9].

An additional means of improving sensitivity involves taking advantage of convection. Flow-through sensors improve the reaction-diffusion kinetics and consequently are more efficient at reacting the target analyte at the electrode surface than traditional bulk sensors. Highly efficient detection of hydrogen peroxide (H_2O_2) with a flow-through VACNT electrode has been demonstrated in convective environments [54], but an investigation into the effectiveness of flow-through sensing for more complex analyte such as glucose is still needed. Flow-through sensors also have the potential for flow injection analysis (FIA), which enables use of much smaller sample volumes [20].

When glucose is not broken down by the body efficiently, the levels of glucose in the blood stream rise, with the potential for diabetes mellitus as a common resulting metabolic disorder [90]. Over 400 million people have diabetes worldwide [1], with many health risks involved if diabetes is not properly diagnosed and treated [91]. Thus, early and accessible diagnostics are important in reducing the negative side-effects of untreated diabetes. There has been much investigation in continuous glucose monitoring sensors [2] and non-intrusive methods as alternatives to traditional blood-pricking methods [3]. Saliva is a more accessible bodily fluid and studies have shown that glucose levels in saliva can be directly correlated to the glucose levels in blood [4]. However, the glucose concentration in saliva is significantly lower than that of blood, requiring a more sensitive glucose sensor to measure glucose levels accurately.

Glucose has also been investigated as a clean alternative energy source through biofuel cells, with recent advances focusing on improving performance with nanomaterials [92]. Glucose-based biofuel cells are typically small-scale energy production devices and have been considered for applications such as self-powered medical devices [93, 94]. While fuel cells typically have electrolyte flowing between two electrodes, it has also been shown that glucose biofuel cells can operate in flow-through conditions, with solution flowing through an entire biofuel cell [95].

Both glucose sensors and biofuel cells commonly use the enzyme glucose oxidase (GOx) to react with glucose. Biofuel cells typically use an electron-mediator, while glucose sensors often convert glucose into H_2O_2, which in turn reacts electrochemically at the electrode surface. Enzymatic glucose sensors are often functionalized with GOx on the surface, and it has been shown that the functionalization technique greatly impacts the sensitivity, selectivity and longevity of such sensors [48]. Primary methods of electrode functionalization include: physical absorption, cross-linking, covalent bonding, bioaffinity bonding, and polymer entrapment. All enzymatic

sensors are prone to enzyme detachment from the surface and to loss of enzyme activity over time; however, enzyme entrapment in conductive polymers has shown to be an effective method of functionalizing the glucose oxidase to maintain stability and functional form with minimal adverse steric effects [96]. Shi, et al. have provided a comparison of functionalization methods for sol-gel encapsulation and glutaraldehyde cross-linking [49], but there lacks a comparison between different functionalization methods for high-aspect-ratio microstructures, where the functionalization needs to penetrate far beyond the easily accessible outer surface.

In recent literature there has been a trend in the development of non-enzymatic glucose sensors [97]. Non-enzymatic sensors have risen in popularity due to their ease of manufacturing and because they do not have the same stability concerns common to enzymatic sensors [50]. Moreover, non-enzymatic biosensors inherently exhibit long operational life, shelf-life, or stability as they do not contain biological components that typically denature within weeks of exposure to aqueous solutions. This stability offers the possibility of a reusable glucose sensor that would not degrade with time. However, non-enzymatic biosensors typically suffer from poor selectivity, especially to electroactive species such as ascorbic acid, uric acid, and acetaminophen—chemical species found endogenously in biological fluids such as blood.

Methyl viologen (MV) may enable a path to improving sensitivity and selectivity of non-enzymatic glucose biosensors. MV has previously been used in conjunction with GOx as an electron-mediator both in solution [98] and immobilized on a sensor surface [99]. However, recent studies have shown that MV can chemically react with glucose (non-enzymatically) at a sufficiently high temperature and pH for potential use in fuel cell applications [51]. This same chemical reaction could also be used for glucose detection, such that the oxidation of reduced-MV

could be correlated with the concentration of glucose, something that has never been done previously in the literature.

Herein, we have manufactured a free-standing, VACNT electrode with 16 μm diameter microchannels (~350 μm long) as a flow-through glucose sensor. A unique method of glucose detection involving a chemical reaction with MV was explored. MV was chemically reduced in the presence of glucose and was subsequently oxidized at the VACNT surface, requiring no additional surface functionalization (including no metal). Challenges with interference chemicals were mitigated by operating at a low potential of -0.2 V vs. Ag/AgCl. This MV-based VACNT sensor was compared to enzymatic VACNT electrodes functionalized by strategies typical for enzymatic glucose sensors. Unlike the MV sensor, the VACNTs of the enzymatic sensors were functionalized with Pt nano-urchins. GOx was incorporated into three different enzymatic VACNT sensors: GOx mixed into the solution, GOx covalently bound to the VACNTs, and GOx entrapped in a polymer on the CNTs. The electrochemical reaction of MV on the VACNT surface was able to produce more electrons per glucose molecule than is possible with GOx (an average of 3.4, compared to a maximum of 2). Current density was linear with flow rate for MV and GOx-in-solution sensing approaches. However, current density was not linear with flow rate when the chemical and electrochemical reactions both happened at the electrode surface, as was the case with the covalent and polymer VACNT sensors. The current density of each of the sensors was linear with glucose concentration, with the MV sensor producing the highest sensitivity and lowest limit of detection. FIA allows for a more practical application, where smaller analyte volumes can be tested by reducing the cross-sectional area of the VACNT electrode. Using MV with a small flow cell has the potential to measure glucose levels with 200 μL samples in the concentration range typical of saliva.

3.4   Methods

3.4.1   VACNT Fabrication

VACNT fabrication methods were similar to previously published protocols [19, 54] and are found in greater detail in Appendix A. Summarizing, 50 nm of aluminum oxide (Al_2O_3) was deposited onto a 100 mm silicon (Si) wafer by e-beam evaporation. Photolithography was used to pattern positive photoresist (AZ3330) into an array of 16 µm diameter circles that would eventually allow for the formation of defined channels. A thin (7 nm) film of iron (Fe) was thermally evaporated onto the patterned photoresist, followed by sonication in N-Methyl-2-pyrrolidone (NMP) for at least 10 minutes for lift-off patterning of Fe (see schematic in Figure 3-1A). The patterned wafer was diced into 17 mm squares using a diamond-coated blade.

VACNTs were grown by chemical vapor deposition (CVD) in a 1 inch diameter Lindberg/Blue M tube furnace with flowing hydrogen (H_2, 311 sccm) and ethylene (C_2H_4, 338 sccm) at 750 °C for 6 minutes. The temperature was then raised to 900 °C and the H_2 flow rate reduced to 190 sccm to infiltrate (coat) the VACNTs with amorphous carbon for 10 minutes (C_2H_4 flow rate was unchanged). This infiltration process strengthened the VACNT structure to create a mechanically sturdy, porous array of microchannels that self-released from the substrate (see geometry in Figure 3-1B). The resulting free-standing VACNT array (about 350 µm thick) was placed in an oxygen plasma etch for 7 minutes (5 minutes on bottom; 2 minutes on top) in a Technics Planar Etch II machine (250 W, 300 mTorr).
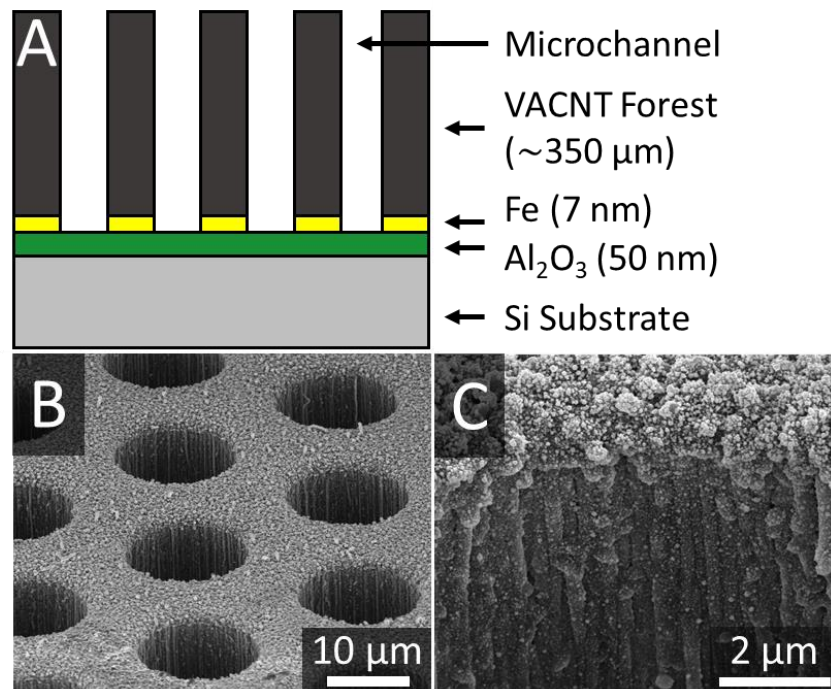
Figure 3-1: (A) Schematic of layers used to manufacture the VACNT sensor architecture (before self-release): Si, Al₂O₃, Fe, and VACNTs. (B) SEM image of array of VACNT microchannels with Pt. (C) SEM image near channel opening, showing Pt coverage on VACNTs.

3.4.2 Functionalization for Enzyme-Based Sensing

3.4.3 Platinum

The VACNTs used for enzymatic sensing were functionalized with platinum nano-urchins (PNUs) as shown in Figure 3-1B and C. The PNUs were deposited in a static, electroless environment by the chemical reduction of a 3 mM chloroplatinic acid hexahydrate solution (37.5% Pt, Sigma-Aldrich 206083) similar to previous protocols [19, 73, 74], The VACNT array was held vertically in a Teflon stand for about 18 hours in a solution containing chloroplatinic acid, 18 mL of ultrapure water and 2 mL of formic acid (88% HCOOH, Macron 2592-05). After the deposition, the PNU-VACNT array was thoroughly rinsed in water and placed on a hot plate to evaporate

excess liquid before measuring the Pt mass. Note that no PNUs were deposited on sensors used with MV (see Figure 3-2A), whereas PNUs were the only functionalization used for sensors with GOx-in-stream (see Figure 3-2B).
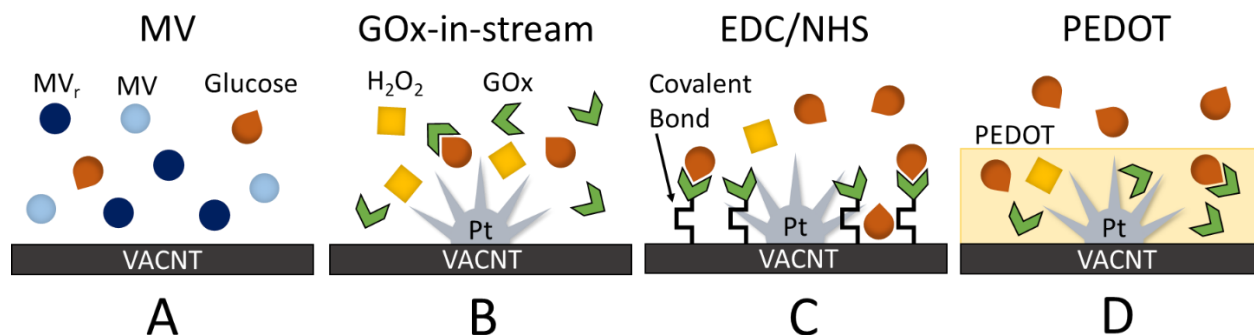
Figure 3-2: Various VACNT glucose sensor configurations. (A) Non-enzymatic MV sensor with no surface functionalization. (B) GOx-in-stream sensor, with Pt on the surface. (C) EDC/NHS sensor with GOx covalently bonded to the VACNTs. (D) PEDOT sensor with GOx entrapped in the polymer.

3.4.4 Covalent (EDC/NHS) Binding

Glucose oxidase from *Aspergillus niger* (GOx, type X-S, 100,000-250,000 units/g, Sigma-Aldrich G7141) was covalently bonded to the PNU-VACNT array using 1-ethyl-3-(-3-dimethylaminopropyl) carbodiimide (EDC, Sigma-Aldrich E7750) and N-hydroxysuccinimide (NHS, Sigma-Aldrich 130672) chemistry following approximately the conditions that were optimized by Wang, et al. (see Figure 3-2C) [100]. The PNU-VACNT array was incubated in 5 mL of 50 mM EDC and 400 mM NHS in 0.1 M 2-(N-morpholino) ethanesulfonic acid (MES, pH 4.7, Thermo Scientific 28390) for 90 minutes to allow the carboxyl groups on the VACNTs to react with EDC and to form NHS esters in preparation for GOx coupling. The sample was then rinsed with ultrapure water and then placed in a 5 mL phosphate buffered saline (PBS, pH 7.4)

solution with 50 mg of GOx (10 mg/mL). The EDC/NHS-PNU-VACNT array was incubated in the GOx mixture at 4 °C at least 16 hours. The GOx-EDC/NHS-PNU-VACNT (hereafter referred to as the EDC/NHS sensor) was then thoroughly rinsed and stored in PBS at 4 °C.

3.4.5 Polymer (PEDOT) Entrapment

GOx was entrapped in the polymer poly(3,4-ethylene-dioxythiophene) (PEDOT) at the PNU-VACNT surfaces following a procedure similar to that of Claussen, et al. (see Figure 3-2D) [23]. First, 35 mg of poly(sodium 4-styrenesulfonate) (PSS, Sigma-Aldrich 243051) was stirred into 5 mL of ultra-pure water. Then, 16 µL of 3,4-ethylene-dioxythiophene (EDOT, Sigma-Aldrich 483028) was mixed into the PSS solution. Finally, 50 mg of GOx (10 mg/mL) was added to the EDOT-PSS solution. The electropolymerization of EDOT to PEDOT was performed in a flow cell (see section 2.6 below) at a flow rate of 0.1 mL/min with a multi-step current (0.5 seconds at 1 mA and 0.5 seconds at 0 A) for 500 cycles. The resulting GOx-PEDOT-PSS-PNU-VACNT (hereafter referred to as the PEDOT sensor) was thoroughly rinsed and stored in PBS at 4 °C.

3.4.6 Amperometric Measurements and Environments

All experiments were performed in a flow-through electrochemical cell (see section 3.4.9) with a saturated (KCl) Ag/AgCl reference electrode, a Pt wire counter electrode, and a VACNT microchannel array as the working electrode. A CH Instruments (CHI) 660E Potentiostat/Galvanostat was employed for all electrochemical testing. Before experiments were performed, a potential (see below for values) was applied to the VACNT electrode until a steady current density was obtained.

3.4.7 Glucose Oxidase

Glucose (Dextrose, Sigma-Aldrich D9434) oxidation with GOx took place under a constant potential of 0.55 V relative to Ag/AgCl in phosphate buffered saline (1X PBS, pH 7.4, Fisher Scientific) at room temperature and typical air exposure. The two-part reaction converted glucose into hydrogen peroxide (H_2O_2) as shown in Equation 3-1 and then the H_2O_2 was oxidized at the PNU-VACNT surface to produce two electrons as shown by Equation 3-2 (equilibrium potential of 0.204 V vs. Ag/AgCl at pH 7.4) [101].

$$\text{D-glucose} + O_2 + H_2O \rightarrow \text{D-gluconic acid} + H_2O_2 \tag{3-1}$$

$$H_2O_2 \rightarrow O_2 + 2H^+ + 2e^- \tag{3-2}$$
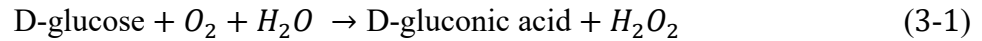
3.4.8 Methyl Viologen

For the non-enzymatic detection of glucose, methyl viologen dichloride hydrate (MV, 98%, Fisher Scientific) was used to chemically react with glucose to produce reduced-MV (MV_r). For this reaction to occur at relevant rates, it was required to increase both temperature and pH [51], with optimal conditions at 55 °C (at a 60 °C set point) and pH 13 (using 0.1 M NaOH). In a basic electrolyte, glucose experiences an enolization process where glucose molecules are converted into endiolate anions, as shown in Equation 3-3 (where D-glucose* represents the endiolate species) [102, 103]. The endiolate species react with MV (the oxidized form of the catalyst) where MV reduces to MV_r (Equation 4). Under this oxidation reaction, the endiolate species then convert into various products that depends on the oxidation extent of the glucose.

$$\text{D-glucose} + OH^- \rightarrow \text{D-glucose}^* \tag{3-3}$$

$$\text{D-glucose}^* + MV \rightarrow MV_r + \text{products} \tag{3-4}$$

The produced MV_r is a free species in the electrolyte which is subsequently oxidized directly on the VACNT surface at a potential of -0.2 V vs. Ag/AgCl without the presence of platinum or any other functionalization on the VACNT structure following Equation 3-5 (standard potential of -0.644 V vs. Ag/AgCl, converted from SCE [104]). Note that MV in Equation 3-5 represents oxidized-MV, returning to its original state before being reduced by glucose.

$$MV_r \rightarrow MV + e^- \tag{3-5}$$

MV experiments were performed in an anaerobic glovebox to prevent oxidation of MV_r, which oxidizes readily in atmospheric conditions with oxygen. Glucose-NaOH solution in 15 mL test tubes (varying concentrations, including a control without glucose) was held in a water bath for about 10 minutes, after which MV was added (1 mM MV) and allowed to react for 20 minutes before introducing the solution into the flow-through set up.

3.4.9   Flow Cell Configurations

The larger electrochemical flow cell is shown in Figure 3-3A, where the VACNT sensor was held between two, size-12 O-rings (3/8" ID) in a clamped Teflon flow cell. Forced mechanical contact between the VACNT electrode and a Nichrome wire allowed for a simple connection mechanism. The flow cell was oriented vertically, with the reference electrode upstream and the counter electrode downstream of the VACNT, each held in place by bored out rubber stoppers. A 60 mL syringe pulled solution through the cell from a reservoir using a Harvard Apparatus PHD Ultra syringe pump to control the flow rate. New pre-mixed concentrations of glucose solution were added to the open reservoir as the previous solution emptied from the reservoir. At high glucose concentrations (>500 μM), the syringe pump was operated in infuse mode instead of withdraw mode to allow bubbles formed at the electrode to escape (only relevant with GOx sensors as no bubbles formed from MV).

Figure 3-3B shows an application of the VACNT sensor at a much smaller scale, where glucose can be injected into the stream (FIA) instead of being pre-mixed in the solution. A much smaller cross-section of VACNT electrode was positioned between two pieces of 1/16" ID (1/8" OD) PVC tubing and held together by 1/8" ID (3/16" OD) tubing. A T-connector was used to allow the reference electrode access to the solution, which was also held in place by 1/8" ID tubing. The solution was pushed (infused) through at a rate of 0.2 mL/min. A 200 µL sample of glucose was manually injected upstream into the tubing over approximately 4 seconds (~3 mL/min).
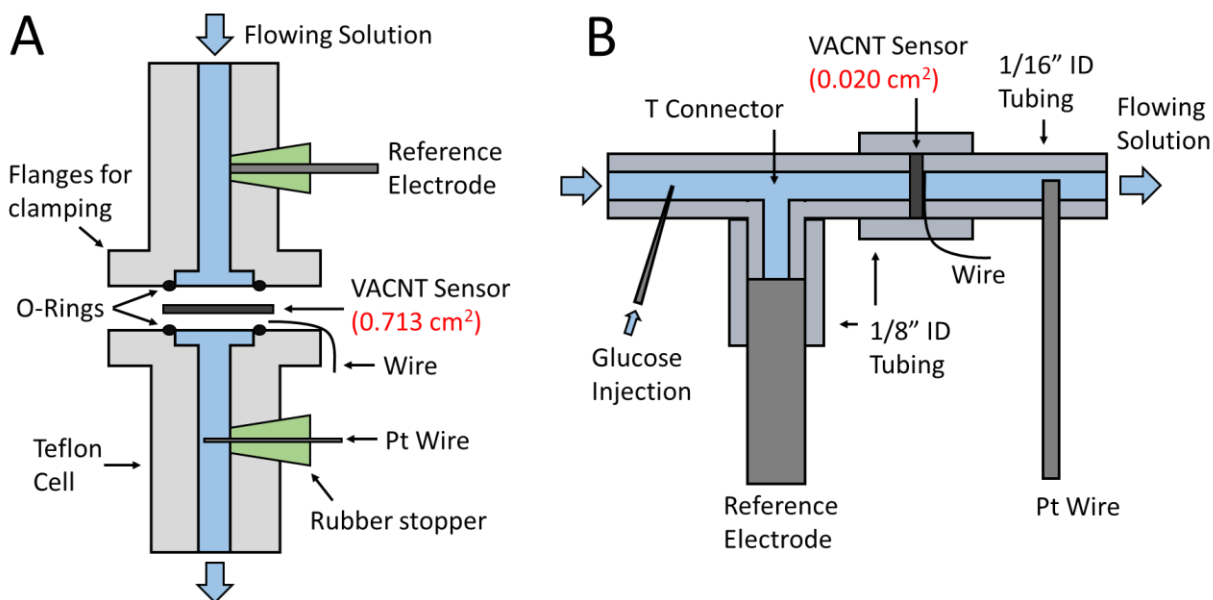
Figure 3-3: Schematic of (A) large and (B) small flow-through cells, where the chemical solution is forced through the VACNT microchannels. The small flow cell enables FIA of 200 µL of glucose.

3.5   Results and Discussion

3.5.1   Characterization

VACNT heights (electrode thicknesses) were measured to be 351 ± 27 μm. With a nominal channel diameter of 16 μm, the channel length to diameter ratio was about 22. The nominal void ratio of each electrode was 0.41. VACNTs coated with amorphous carbon have been shown to have a high number of surface defects that are favorable for increasing charge transfer, as previously shown by Raman spectroscopy [105].

For the enzymatic sensors, the mass of the deposited Pt was measured to be 4.46 ± 0.70 mg (14.7 ± 2.3 % of sensor by weight). More detailed characterization of Pt deposited in a similar manner can be found by others, including analysis by TEM [19] and XRD [106].

3.5.2   MV Wait Time

For the chemical reaction of glucose with MV, a maximum pH of 12 is recommended by Watt because MV becomes unstable at high pH [51]. However, it was found that at relatively low MV concentrations (1 mM), MV could be used in a pH 13 solution (0.1 M NaOH) because the rate of MV decomposition was negligible compared to the glucose-MV reaction. Thus, a pH 13 solution was chosen to provide faster reaction rates of glucose and reduce the waiting time. To determine the optimal waiting time for the reaction, the current was measured in the large flow cell in 10 min intervals (data not shown). A maximum current was obtained at 30 minutes, with 82% of the maximum at 10 minutes and 97% of the maximum at 20 minutes. Longer times (40 and 50 minutes) resulted in a slight decrease in the measured current. Thus, a 20 minute wait time was chosen for all subsequent experiments.

3.5.3 Flow Rate

Flow rate greatly influences the sensitivity of flow sensors and can provide linearly varying current with flow rate [54]. Figure 3-4 shows the measured current density for 100 μM glucose at different volumetric flow rates (0.5 to 8 mL/min; average velocities: 0.283 to 4.53 mm/s) for each of the glucose sensors (MV, GOx-in-stream, EDC/NHS, and PEDOT; see Figure 3-2) in the large flow cell. A concentration of 100 μM glucose was chosen to mimic a typical glucose concentration found in saliva and is representative of an accessible bodily fluid with a lower concentration. The current was normalized by the frontal surface area, as defined by the O-rings (0.713 cm^2).

Figure 3-4A shows that the current density was largest and most linear with flow rate when the glucose reaction occurred upstream of the VACNT electrode, as was the case with both GOx and MV in solution. The green dashed line represents the current density that would be obtained for 100 μM glucose (at the given flow rate) if each glucose molecule produced two electrons. This becomes the theoretical maximum for GOx reactions if each glucose molecule was converted into H_2O_2 and then each H_2O_2 molecule reacted at the surface (see Equations 3-1 and 3-2). However, when the GOx was in the stream, a reaction efficiency of glucose to H_2O_2 was observed, as the current density was only about 64% the theoretical values. On the other hand, the MV reaction produced a significantly higher current density, at approximately 2.65 times the current density produced with GOx in stream, resulting in an average of 3.4 electrons per glucose molecule. This is possible because it is not H_2O_2, but MV_r, that is oxidized at the electrode surface (see Equation 3-5). Tests were repeated for three separate VACNT sensors with an average standard deviation relative to the mean of 11.9%. It should be noted that the lowest flow rate gave a much higher relative standard deviation of 31.5% and was likely due to experimental error.
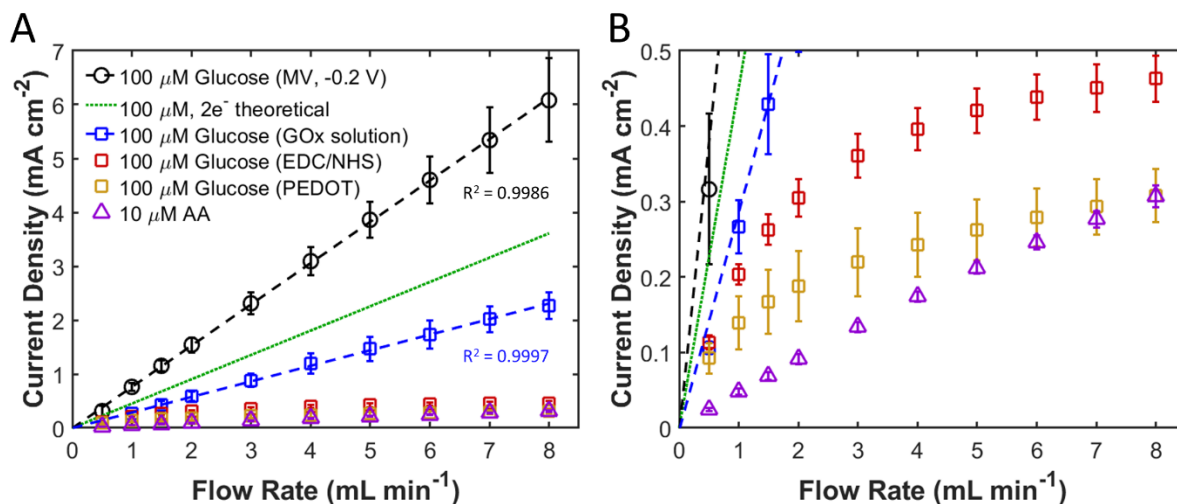
Figure 3-4: (A) Comparison of current density from 100 μM glucose for different VACNT electrodes at various flow rates (0.5 – 8 mL/min). The current density from MV and GOx-in-stream sensors were both linear with flow rate, with the MV sensor collecting more than 2 electrons per glucose molecule. The MV sensor operated at -0.2 V vs. Ag/AgCl in 0.1 M NaOH, while the remainder of the sensors were tested at 0.55 V vs. Ag/AgCl in pH 7.4 PBS. The current density from ascorbic acid (AA) at 0.55 V vs. Ag/AgCl is also shown. (B) Close up of low current density measurements, showing that the EDC/NHS and PEDOT sensors were nonlinear with flow rate. Note that error bars represent standard deviation from three repeat measurements.

When the chemical reaction was moved to the electrode by functionalizing the VACNTs with GOx, a nonlinear trend with flow rate was observed (see Figure 3-4B). At the lowest flow rate tested (0.5 mL/min), the current density of each of the GOx sensors was very similar, but the current densities of the functionalized sensors begin to asymptote as flow rate increases. This suggests that the time component to the two-part reaction of glucose with GOx and H_2O_2 with the PNU-VACNT surface becomes significant at high flow rates. For example, at 0.5 mL/min there would be on average 1.24 seconds to complete the chemical and electrochemical reactions within the VACNT array, but only 0.08 seconds at 8 mL/min. When the chemical reaction takes place before reaching the electrode, only the electrochemical portion needs to take place during this time. Although both the EDC/NHS and PEDOT sensors follow the same trend, it can also be seen in Figure 3-4B that the EDC/NHS sensor exhibited higher current densities at higher flow rates (about

1.5 times larger at 8 mL/min). The lower current from the PEDOT sensor could be caused from less coverage of GOx as a result of the polymer functionalization, or because the polymer layer acts as a diffusion barrier between the VACNT surface and the solution. It is also possible that variations in PEDOT coverage and VACNT channel length caused the PEDOT sensor to have the largest average standard deviation relative to the mean at 18.8%.

Flow rates for subsequent concentration tests were chosen to yield large current densities while still maintaining reasonable solution volumes. For GOx functionalized on the VACNTs, it is most efficient to be below 3 mL/min at a concentration of 100 μM because current doesn't increase significantly with flow above this point. A flow rate of 1 mL/min was chosen because the EDC/NHS current density was still close to the GOX-in-stream current density at this point and for reasons discussed in the following section on selectivity (see section 3.5.4). For the in-solution sensors, the selection of flow rate is somewhat arbitrary as sensitivity will continue to increase with increasing flow rate. To maintain reasonable solution volumes, a flow rate of 6 mL/min was chosen.

3.5.4 Selectivity of Enzyme Sensors

Selectivity of glucose against interfering species is important for the accurate measurement of glucose concentrations. Also shown in Figure 3-4 is current density with flow rate for 10 μM of ascorbic acid (AA, Fisher Scientific) at a potential of 0.55 V vs. Ag/AgCl (same as GOx tests), as tested with each of the GOx sensors (Pt only, EDC/NHS, and PEDOT). The current density from this interfering species was rather large because AA oxidizes readily at this potential [107]. This was especially significant for the low current densities of EDC/NHS and PEDOT sensors at high flow rates, which is the main reason to operate the functionalized sensors at a low flow rate (1 mL/min). GOx-in-stream had the least impact, with the 10 μM AA giving a current density

about 15% of the 100 µM glucose current density (minimal dependence on flow rate). At lower potentials, it is possible to minimize the effects of interfering species and measure the change in the O_2 reduction current [107]. However, at low potentials the PNU-VACNTs produced a very large negative current from the reduction of oxygen, making it unreasonable to operate at low potentials in the presence of oxygen (oxygen is required for the GOx reaction).

It has previously been shown that a polymer layer such as PEDOT can help reduce the impact from interfering species [23]. However, the current density was nearly identical with and without the PEDOT layer on the PNU-VACNT electrodes, as the small standard deviation in Figure 3-4B includes both PEDOT and non-PEDOT samples. It is possible that the large surface area and high-aspect-ratio VACNT channels were not completely coated with the polymer and the resulting electrode was thus able to oxidize the interfering species at the same rate as the sensors with PEDOT.

3.5.5 Selectivity of MV Sensor

With MV there was more flexibility in the operating potential of the sensor because tests were performed in an oxygen-free environment (avoiding the current from oxygen reduction while preventing the oxidation of MV_r) and because the standard equilibrium potential of MV is very low (-0.644 vs. Ag/AgCl, converted from SCE [104]). It was observed that a significant current was produced by interfering species on the VACNT electrode at potentials above about -0.2 V vs. Ag/AgCl, below which the current from the interfering species was significantly lower (data not shown). Thus, a potential of -0.2 V vs. Ag/AgCl was chosen for all experiments with MV.

Figure 3-5 shows the impact of interfering species on the current density of 100 µM glucose with 1 mM MV. The initial baseline is from heated 0.1 M NaOH and 1 mM MV flowing at 6 mL/min, followed by the upstream addition of heated NaOH with 100 µM glucose and 1 mM MV

54

at ~100 s. As this upstream solution was depleted, a comparable mixture was added to the upstream reservoir at ~210 s, now with several interfering chemicals present (NaOH heated with 100 μM glucose, 10 μM AA, 10 μM uric acid (UA, Sigma-Aldrich U2625), 10 μM acetaminophen (AP, Sigma-Aldrich A5000) and 1 mM MV). In this manner, the ability to detect glucose in the presence of the interfering chemicals was demonstrated. There was an observed increase in current density of about 6% from the three interfering species combined, likely caused by a slight reaction with MV. It should be noted that a small oscillation in the measured current was observed after the addition of glucose, as can be seen in Figure 3-5. The oscillations corresponded to the stepping of the syringe pump, a phenomenon previously observed in the signal for H_2O_2 detection [54].
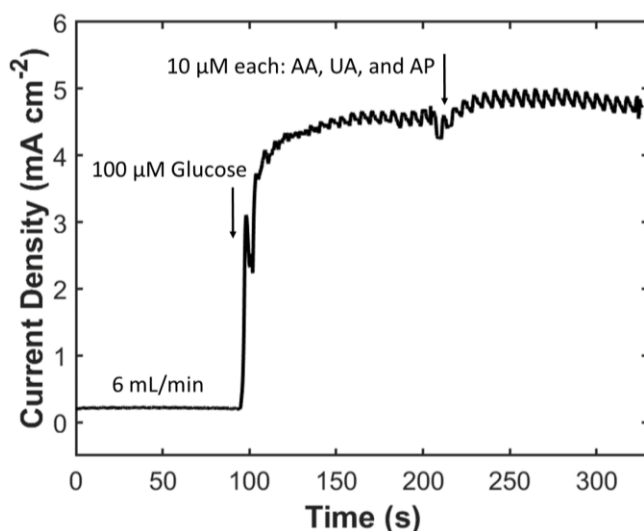
Figure 3-5: Current density with time for 100 μM glucose and 1 mM MV in 0.1 M NaOH flowing at 6 mL/min and potential of -0.2 V vs. Ag/AgCl, followed by an upstream addition of 10 μM of each of the following common interfering species: ascorbic acid (AA), uric acid (UA) and acetaminophen (AP). A 6% increase in current was observed by the addition of interfering species with the glucose.

3.5.6 Sensitivity, Limit of Detection, and Linear Sensing Range

The current density with time at lower concentrations of glucose (2.5 to 10 µM) with MV is shown in Figure 3-6. The baseline is heated NaOH and 1 mM MV flowing at 6 mL/min, followed by the upstream additions of heated NaOH with glucose and 1 mM MV. At these low concentrations, there is still a distinct increase in current with the addition of glucose and a linear relationship between current density and glucose concentration is apparent.
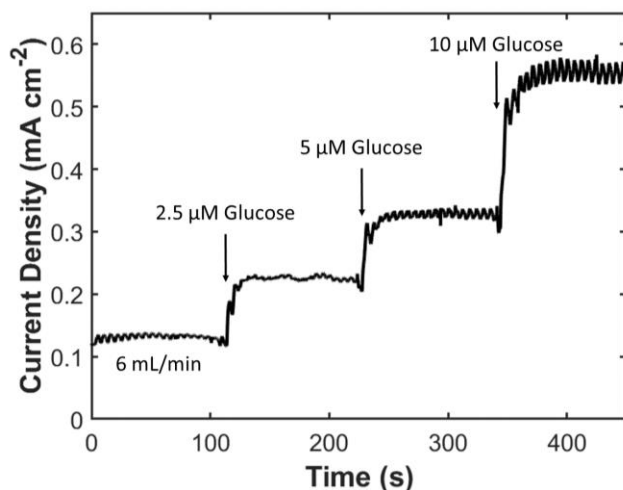
Figure 3-6: Current density with time for low glucose concentrations (2.5, 5, 10 µM) with 1 mM MV in 0.1 M NaOH at a flow rate of 6 ml/min and potential of -0.2 V vs. Ag/AgCl.

Figure 3-7 shows the current density at various glucose concentrations for MV, GOx-in-solution, and EDC/NHS sensors. The PEDOT sensor was not included in the concentration experiments because it showed no advantage over the EDC/NHS sensor from the flow rate experiments in section 3.5.3. In Figure 3-7A the full linear range of the EDC/NHS sensor is shown to be much larger than the other two sensors, up to about 6 mM glucose. The MV and GOx-in-solution sensors both reach their linear limit at about 200 µM glucose. It is likely that the EDC/NHS electrode had a much larger linear range because it was operating at a much lower flow

rate. Thus, it seems that the flow rate of the sensor could potentially be modified to target different concentration ranges with a linear response.

Figure 3-7B shows the linear range for the MV and GOx-in-solution sensors. It can be seen that each sensor is linear below 200 µM glucose, with MV having the largest slope and thus the highest sensitivity at 45.93 mA mM^{-1} cm^{-2} (based on the projected frontal area of 0.713 cm^2). The limit of detection (LOD) of each sensor was calculated from the sensitivity (based on three times the standard deviation of the baseline), with the observed lowest linear sensing region being slightly higher than the LOD. The MV sensor had the lowest LOD at 100 nM glucose and was linear down to a concentration of 250 nM. Table 3-1 summarizes the measured performance of each VACNT sensor, including the sensitivity, LOD, and linear range. The low limits of detection and high sensitivities for the VACNT sensors shown in Table 3-1 are comparable with the best glucose sensors in the literature, with glucose sensors typically ranging from 5 to 100,000 nM glucose LOD and sensitivities of 0.001 to 12 mA mM^{-1} cm^{-2} [9, 37, 96, 108]. The large sensitivity of the VACNT sensors comes from high current per geometric cross-sectional area and does not include the surface area associated with microchannel length. It is interesting to note that although the sensitivity of the EDC/NHS sensor was much lower, the background noise was nearly proportionally smaller, such that the calculated limit of detection was still very similar to that of the other sensors. With GOx in solution, the background noise was significantly higher than that for PBS alone. Although the EDC/NHS sensor operated at a slower flow rate of 1 mL/min, it would have only marginally increased sensitivity if operated at 6 mL/min, as noted in section 3.5.3.
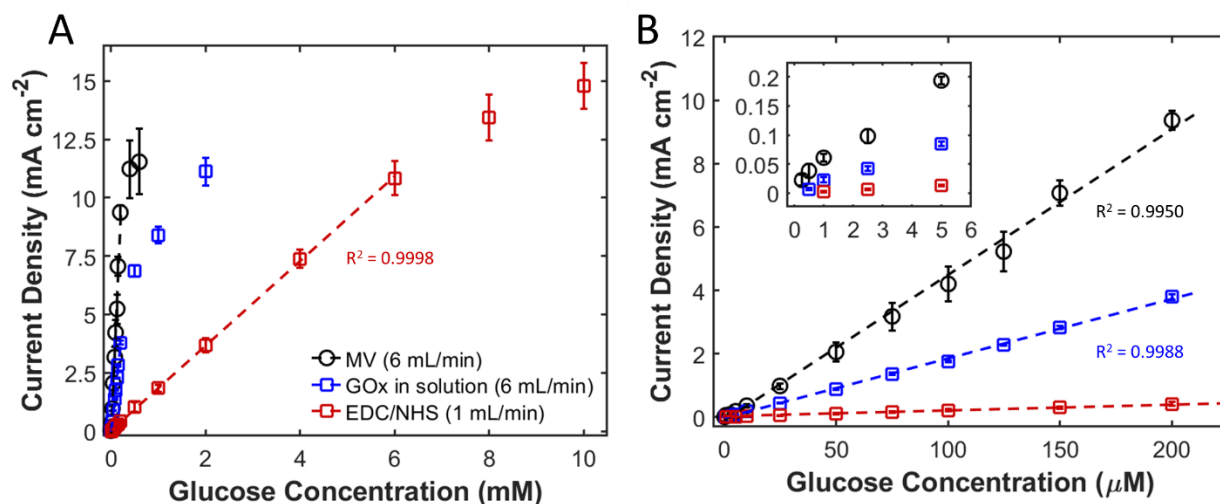
Figure 3-7. Measured current density at different glucose concentrations flowing at 1 mL/min for EDC/NHS sensors and 6 mL/min for MV and GOx-in-solution. The MV sensor operated at -0.2 V in 0.1 M NaOH, while GOx-in-solution and EDC/NHS sensors were tested at 0.55 V in pH 7.4 PBS. (A) Full linear range of EDC/NHS sensor is shown to be much larger than the linear range of GOx-in-solution and MV. (B) Current density for lower glucose concentrations, where all of the sensors are linear and MV has the highest current density for any given concentration. Inset: Linear sensing range as low as 0.25 µM. Note that error bars represent standard deviation from three repeat measurements.

Table 3-1: Summary of various VACNT sensor conditions and measured results in this work.

Sensor	Potential[*] (V (Ag/AgCl))	Flow Rate[†] (mL/min)	Sensitivity[‡] (mA mM^{-1} cm^{-2})	LOD (nM)	Linear Range (µM)
MV	-0.2	6	45.93	100	0.25 to 200
GOx-in-solution	0.55	6	18.77	194	0.5 to 200
EDC/NHS	0.55	1	1.815	311	1 to 6,000
Small MV	-0.2	0.2	5.002	360	<50 to >150[§]

[*]Chosen to produce high glucose signal while reducing signal from interfering species (see sections 3.5.4 and 3.5.5)

[†]Selected based on linearity and solution volume limitations as noted in section 3.5.3

[‡]Based on projected frontal area of 0.713 cm^2 (or 0.020 cm^2 for small MV sensor)

[§]Linearity beyond this range was not explored

3.5.7   Small Volume MV Sensor

A smaller flow cell (see Figure 3-3B) was used to demonstrate glucose detection with much smaller volumes (200 µL) via flow injection analysis (FIA). The cross-sectional area was reduced by 36 times, giving an area of only 0.020 cm^2 (compared to 0.713 cm^2). A flow rate of 0.2 mL/min was chosen, giving an average velocity of 4.08 mm/s. This velocity through the smaller sensor was comparable to that for the larger flow cell (equivalent to a large cell flow rate of 7.2 mL/min). However, during glucose injection the velocity increased as the 200 µL sample was injected over about 4 seconds (about 3 mL/min). The overall flow rate through the small sensor would then be ~3.2 mL/min, suggesting that the solution concentration would be approximately 95% of the injected glucose concentration.

Figure 3-8A shows the current density with time during the injection of different glucose concentrations (0, 50, 100, 150 µM) and 1 mM MV. The conditions were the same used with MV in the large flow cell: a 20-minute wait time in pH 13 (0.1 M) NaOH, with the VACNT electrode at a potential of -0.2 V. Two injections are shown for each concentration, with a close up of a single injection shown in the figure inset. There was a high current density measured during the glucose injection period (about 4 seconds). After the injection, there was a steady region with a high glucose concentration at the original flow rate (0.2 mL/min) before the current density reduced to the baseline current.

With this FIA, there are three different values that can be used to correlate to glucose concentration: (1) integration of the current to obtain total charge (normalized by the injection volume), (2) measured peak current density during injection, and (3) measured steady current density after the injection. Figure 3-8B shows that each of these measurement techniques was linear with glucose concentration. However, a larger standard deviation of peak current density

was observed (44.6% average standard deviation relative to the mean), compared to the steady

region current density (15.5%). The large standard deviation of the peak current density was likely

due to manual control of the injection rate, where the rate of injection greatly influenced the peak

current densities.
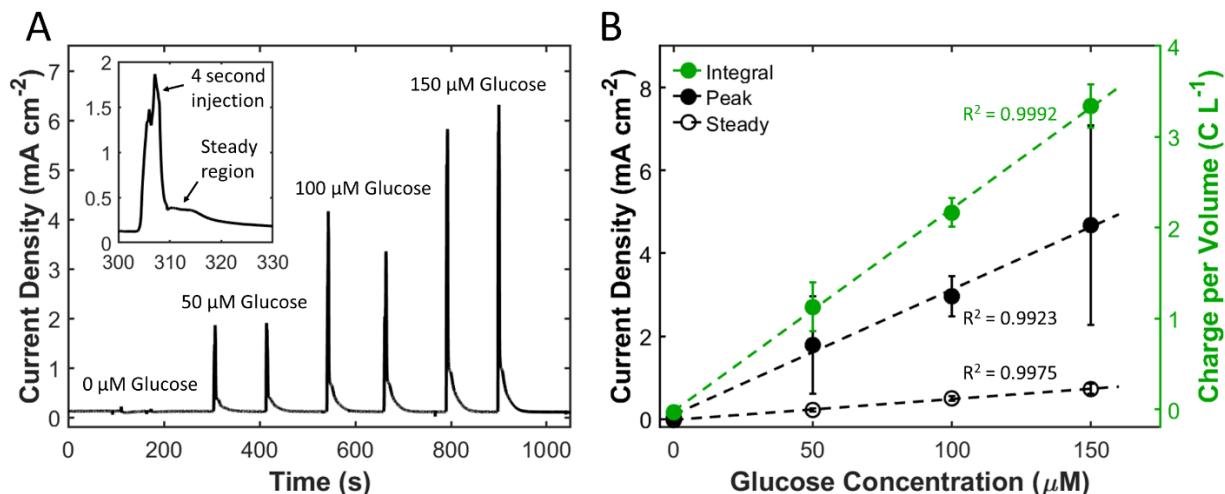
Figure 3-8: Small volume flow cell with 200 µL injections of glucose (0, 50, 100, 150 µM) and 1 mM MV flowing at 0.2 mL/min and operating at -0.2 V in 0.1 M NaOH. (A) Current density from two injections of each concentration as a function of time. Inset: Zoomed view of 50 µM injection, showing the peak caused by injection and a steady region before reducing to baseline current. (B) Methods used to detect glucose concentration including integration of current from injected glucose (normalized by injection volume), peak current density during injection, and steady current density just after injection. Each method is linear with concentration with the peak current density measurements exhibiting the largest standard deviation. Note that error bars represent standard deviation from the average of two tests for three repeat devices.

Although the current-integration method is a valid calculation method, by using the current

density measured in the steady region it was possible to determine a sensitivity and limit of

detection that could be compared with the large flow cell. The sensitivity from the curve fit slope

was determined to be 5.002 mA cm^{-2} mM^{-1}, which is about 9 times smaller than the sensitivity of

the large flow cell. Although a larger sensitivity could be obtained using the peak current density,

the measured signal was much more variable than the steady current density, as noted by the large error bars in Figure 3-8B.

With a smaller sensor also came much smaller background noise, which resulted in a calculated limit of detection (LOD) of 360 nM glucose. Thus, although the sensitivity was less than the large MV sensor, the smaller background noise helped give a comparable LOD. The full linear range was not investigated for the smaller sensor, but experiments demonstrate that the measurement was linear with concentration up to at least 150 µM glucose. Within this concentration range and with as little as 200 µL (or potentially less) the MV sensor has the potential to measure the glucose levels found in saliva [4]. Table 3-1 reports the measured performance of the small sensor as compared to the other sensors in this work.

3.5.8   Advantages and Disadvantages of MV for Glucose Sensing

MV has been shown to be a promising agent for enhancing glucose detection. Because the chemical reaction does not involve a pathway with H_2O_2, it is possible to detect more than 2 electrons per glucose molecule. This led to a very high sensitivity with a low limit of detection for both the large bulk experiments and for the small volume FIA experiments. Also, no additional functionalization of the sensor was necessary, as the electrode consisted of only carbon (VACNTs with added carbon from the infiltration process). This means that no metal was needed and also no enzyme was necessary, avoiding typical problems of enzymatic sensors, such as signal decay in time. The low working potential also allowed for minimizing the effect of interfering species.

The advantages of using MV come at a potential cost, as the MV sensor exhibits a few key restrictions when compared to GOx-based sensors. The temperature of the solution was elevated to 55 °C in order to facilitate the reaction of MV with glucose and was allowed to proceed for 20 minutes in an oxygen-free environment before measuring the current. The solution was also at pH

13, likely requiring an increase in solution pH, similar to many other non-enzymatic sensors. While these conditions may be challenging to implement and are limited to in vitro applications, the idea of utilizing an amplification chemical to react with glucose is an intriguing prospect.

3.6   Conclusions

This work has shown the effectiveness of using MV as the reacting agent for glucose detection. When combined with the VACNT electrode, the measured current density from the non-enzymatic MV reaction was very high (with a sensitivity of 45.93 mA mM^{-1} cm^{-2} and a limit of detection of 100 nM). These high current densities were linear with both flow rate and glucose concentration in the 0.25–200 µM range and the effect from common interfering species was minimal at the low working voltage of -0.2 V vs. Ag/AgCl. Future work will involve investigating the interference from carbohydrates other than glucose. MV-based glucose sensing is potentially limited in self-glucose monitoring applications due to the chemical reaction of glucose with MV at an elevated temperature in an oxygen-free environment for several minutes before passing though the sensing electrode.

With surface-based, enzymatic GOx reactions, the measured current density leveled off at lower flow rates than for sensors that allowed the chemical reaction to take place in solution. For convective-enhanced sensor technologies, the additional requirement of having all of the chemical reactions taking place at the sensor surface introduces an additional limitation in utilizing flow rate to increase sensor sensitivity. Further, measured current densities with MV were higher than theoretically possible with enzymatic GOx reactions, with a release of 3.4 electrons per glucose molecule on average. The additional electrons made available with MV in this flowing configuration may also be useful in increasing power output of glucose-based biofuel cells.

The MV sensor was scaled down in size to enable the detection of glucose in small volumes of only 200 µL. The small sensor had a high enough sensitivity to potentially measure glucose levels found in saliva, with testing in real saliva samples as an area for future investigation. The small VACNT configuration could also be applied to enzymatic sensors, with potential future work including the exploration of injection-based, small volume sensing with VACNT electrodes to enhance enzymatic sensing.

4 3D INTERDIGITATED VERTICALLY ALIGNED CARBON NANOTUBE ELECTRODES FOR ELECTROCHEMICAL IMPEDIMETRIC BIOSENSING

This chapter demonstrates the utility of high aspect ratio interdigitated electrodes made of VACNTs. Aspect ratio and surface area were shown to be important factors in determining the sensitivity of 3D VACNT interdigitated electrodes for impedimetric sensing of biomolecules bound to electrode surfaces. The highest sensitivity was observed with the highest aspect ratio interdigitated electrode, as shown using a demonstrative protein (streptavidin) bound to VACNTs for the impedimetric detection of the small biomolecule biotin, which results could be applied for future applications such as oral cancer screening.

4.1 Contributing Authors and Affiliations

Benjamin J. Brownlee, Jonathan C. Claussen,* and Brian D. Iverson

Department of Mechanical Engineering, Brigham Young University, Provo, UT, 84602

*Department of Mechanical Engineering, Iowa State University, Ames, IA, 50011

4.2 Abstract

Advances in nanomaterials, combined with electrochemical impedance spectroscopy (EIS), have allowed electrochemical biosensors to have high sensitivity while remaining label-free, enabling the potential for portable diagnosis at the point-of-care. We report porous, 3D vertically aligned carbon nanotube (VACNT) electrodes for impedance-based biosensing characterized by

electrode height (5, 25, and 80 µm), gap width (15 and 25 µm), and geometry (interdigitated and serpentine). Electrodes are characterized using scanning electron microscopy, cyclic voltammetry, and electrochemical impedance spectroscopy (EIS). The protein streptavidin is functionalized onto VACNT electrodes for detection of biotin, as confirmed by fluorescence microscopy. EIS is used to measure the change in impedance across electrodes for different biotin concentrations. Tall, closely-spaced VACNT interdigitated electrodes (IDEs) are shown to have the highest electroactive surface area (15x the 2D geometric area) and the highest sensitivity, while serpentine electrodes (SEs) are observed to be less sensitive. Two linear sensing regions and a limit of detection of 1 ng/mL biotin are observed. The relative change in imaginary impedance from biotin is shown to be as high as 107%. Although this biosensing platform is shown with streptavidin and biotin, it could be extended to other proteins, antibodies, viruses, and bacteria.

4.3   Introduction

Carbon nanomaterials such as carbon nanotubes (CNTs), graphene, and graphene oxide have been shown to effectively increase the sensitivity of electrochemical sensors [37, 109]. Specifically, micro and nanostructured surfaces greatly increase electrode surface area and may outperform smooth, planar geometries [30]. The high electrical conductivity and high surface area of CNTs make them attractive as an electrode nanomaterial [38]. Many CNT sensors incorporate randomly dispersed CNTs that are cast on an electrode surface [39], but nanostructures grown from an electrode surface have been shown to have greater stability and allow for greater exposed surface area [40]. Particularly, vertically aligned carbon nanotubes (VACNTs) provide an ordered, preferential orientation of CNTs that are grown from the substrate. Very high aspect ratio geometries are possible through patterning of the VACNT forest, offering the potential for three dimensional (3D), porous electrodes that may be exploited for concentration measurement of

proteins, antibodies, or other molecules. The high surface-area-to-volume ratio that comes from the 3D, porous VACNT electrodes enables higher protein capture capacity relative to planar electrodes, leading to the potential for improved sensitivity [41]. High sensor sensitivity is important for enabling detection of low concentrations of target analyte, opening the door for new sensing applications, such as early diagnostics.

Advances in electrochemical biosensors have pushed toward the ability to obtain effective, rapid results. While biosensors can use a variety of detection methods such as optical, electrical or piezoelectric, electrochemical sensors offer the advantage of being repeatable, affordable, and easy to use [9]. In particular, electrochemical sensors comprised of interdigitated electrodes (IDE) exhibit low ohmic drops, high signal-to-noise ratios, and fast response times [11]. IDE biosensors are often impedimetric, using electrochemical impedance spectroscopy (EIS) to measure small changes in impedance at an electrode surface and offer the potential for label-free and real-time detection of various analytes [52, 53]. These advantages of electrochemical IDE biosensors enable portable diagnosis at the point-of-care by eliminating the need for laboratory expertise and the time associated with conventional immunoassay-based testing [110, 111].

While IDE geometries are typically used, a serpentine electrode (SE) design has been shown to increase sensitivity of a capacitive humidity sensor when compared to an IDE of the same material and dimensions [112]. A serpentine design has been used in other applications, such as in the design of a flow field for redox flow batteries to enhance performance through geometry [113]. Hence both the IDE and serpentine geometry would be of interest to explore in terms of electrochemical sensing performance.

In addition to electrode geometry, electrode surface areas also plays an important role in electrochemical sensing. Typical planar electrodes have a thickness that is on the order of 10s to

100s of nanometers. While an electrode height (thickness) of a few micrometers may be considered 3D, patterned VACNTs offer the potential to increase the electrode thicknesses to greater than 100s of micrometers. VACNTs have previously been used as IDEs for capacitors with VACNT heights ranging from 34 – 70 µm with a 20 – 35 µm gap between electrodes [44-46]. Although such tall heights are not typically reported for electrochemical biosensors, our previous work with an oral cancer biomarker had a VACNT electrode height of about 75 µm and gap of 25 µm [105].

Previous IDE sensors were made entirely of VACNTs, including the interdigitated fingers and the electrical leads [105]. A redox sensor for dopamine was constructed with a VACNT electrode height of 0.66 µm and 3 µm gap, where the fingers of VACNT IDEs were grown directly on metallic electrical leads [114]. Others have shown that an electrical connection can be made from VACNTs through an insulating aluminum oxide layer to an underlying metallic electrical lead [47]. This approach using a thin metallic electrical lead offers a way to separate the leads from the sensing region and enables access to the sensor when used within a microfluidic cavity. The ability to use a sensor in a microfluidic channel is an additional feature that promotes point-of-care diagnosis, as microfluidics-based detection offers simple, fast and convenient platform relative to traditional macroscopic platforms [13].

This work characterizes porous, 3D VACNT electrodes for impedance-based biosensing by comparing the change in electrochemical impedance for different electrode heights, gap widths, and geometries (IDE vs SE). Patterned VACNT forests were grown to heights of 5, 25, and 80 µm on underlying chromium electrical leads. Amorphous carbon was added to provide additional rigidity to the VACNTs while still maintaining porosity. Electrodes were characterized using scanning electron microscopy and cyclic voltammetry. To compare the performance of the distinctly constructed VACNTs within an electrochemical biosensing paradigm, the common

protein-ligand system (streptavidin-biotin) was employed. The protein streptavidin was functionalized onto VACNT electrodes for detection of biotin, where biotin binds to streptavidin in one of the strongest known non-covalent bonds between a protein and a ligand [115]. Fluorescence microscopy aided in confirming streptavidin and biotin binding on VACNTs. Electrical impedance spectroscopy (EIS) was used to measure the change in impedance across electrodes for different biotin concentrations. The change in impedance with the addition of streptavidin and biotin was modeled by an equivalent electrical circuit and the change in imaginary impedance at a single frequency was monitored for different biotin concentrations. VACNT height and electrode geometry are shown to influence biosensor sensitivity, with tall, closely-spaced IDEs having the highest sensitivity. Comparison between 3D IDE and SE configurations are also provided. Although this biosensing platform is shown with streptavidin and biotin, it could be extended to other proteins, antibodies, viruses, and bacteria by functionalizing with another biorecognition agent with a selective binding mechanism.

4.4   Results and Discussion

4.4.1   Electrode Design

The IDE design is illustrated in Figure 4-1A and the SE design is shown in Figure 4-1B, with some additional details given in Appendix E. Dark red and blue areas (central region) represent patterned forests of VACNTs acting as the electrodes; light red and blue areas (left and right edges) represent thin chromium (Cr) electrical leads underneath an aluminum oxide (Al_2O_3) layer. This approach with buried Cr electrical leads differs from our previously reported sensors [105] with electrical leads comprised of VACNTs and allows for integration into a microfluidic

channel (see section 4.4.5 and Appendix D). Figure 4-1C illustrates the three-dimensional nature of VACNT IDE electrodes.

The electrode length (L) was 2.95 mm for all sensors tested in this work. Two different electrode widths (w_e, 20 and 25 µm), and two different gap widths (w_g, 15 and 25 µm), were used for IDE and SE sensor designs. VACNT height (h) was varied for the IDE electrode arrangement (5, 25, and 80 µm), resulting in six different geometries summarized in Table 4-1.
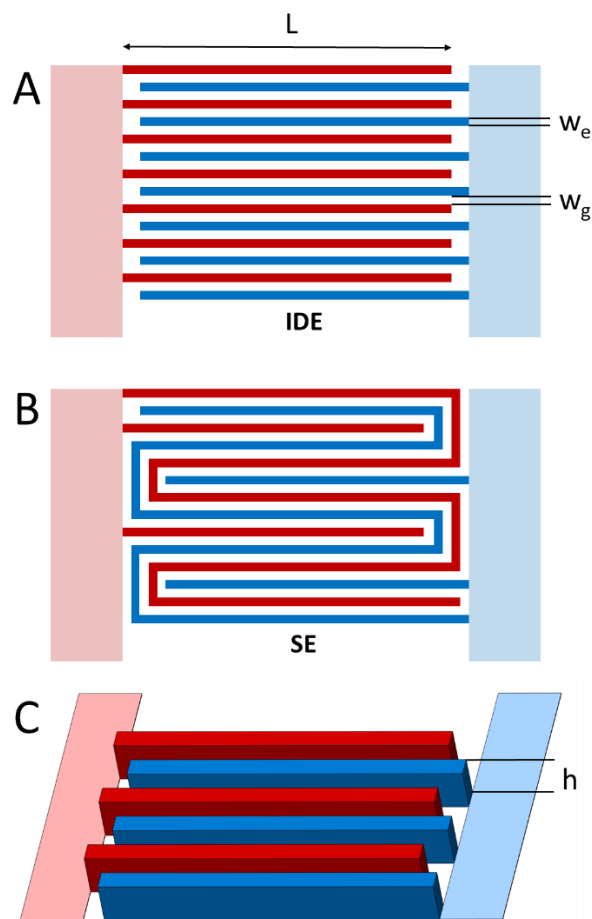
Figure 4-1: Schematic of the (A) IDE and (B) SE electrode arrangements with electrode length (L), electrode width (w_e), and gap width (w_g) represented. Red and blue distinguish the different electrodes in the sensor, with the dark colors representing regions of VACNTs and light colors representing Cr leads under Al_2O_3. (C) Schematic emphasizing 3D nature of VACNT IDE electrodes with electrode height (h) represented. Images are not to scale and do not show all fingers.

Table 4-1: Summary of dimensions for sensor geometries.

Geometry	w_e (μm)	w_g (μm)	h (μm)
IDE	25	25	5
	25	25	20
	25	25	80
	20	15	80
SE	25	25	80
	20	15	80

Each IDE sensor had 61 total fingers (30 and 31 per side) and each SE sensor occupied an equivalent area with two winding fingers (1 per side) and 20 shortened fingers (10 per side). For $w_g = 25$ μm, the sensing region was nearly square at 3.025 mm x 3 mm, with a total electrode area of 4.5 mm^2. For $w_g = 15$ μm, the sensing region was smaller at 2.115 mm x 3 mm, with a total electrode area of 3.6 mm^2. The two Cr electrical leads for each sensor are 13 mm x 0.5 mm.

4.4.2 VACNT Characterization

Figure 4-2A shows the processing layers for biosensor fabrication, where an oxidized silicon (Si) wafer had patterned Cr and patterned iron (Fe) separated by the insulating Al_2O_3 layer. Planar Cr electrical leads underneath Al_2O_3 can be seen in Figure 4-2B as the lighter region on the substrate. VACNTs were grown by chemical vapor deposition (CVD) similar to previously published protocols [19, 54]. After VACNT growth, amorphous carbon was added to strengthened the VACNTs and create mechanically sturdy, porous microstructures (see Figure 4-2B and C).

Carbon-coated VACNTs are slightly hydrophobic after they are grown. An oxygen plasma etch was used to remove the amorphous carbon in between electrodes and also served to change the VACNTs from hydrophobic to hydrophilic [19]. This hydrophilicity is important to ensure that

the solution is wetting the entire electrode and to promote close contact between the molecules in solution and the electrode surface.
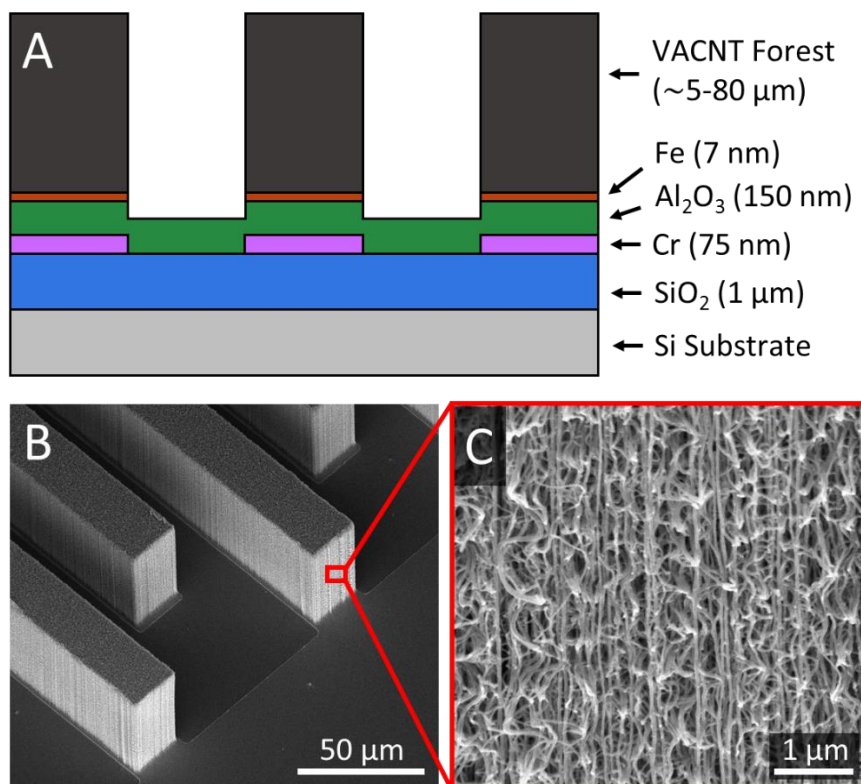
Figure 4-2: (A) Schematic of layers used to fabricate the VACNT sensor architecture: Si, SiO_2, Cr, Al_2O_3, Fe, and VACNTs. Scanning electron microscope (SEM) images of (B) 3D VACNT electrodes and (C) magnified VACNTs, showing porous nature of electrode.

VACNT electrode heights were measured using optical profilometry. CVD growth times of 5, 30, and 120 s corresponded with approximately 5, 20, and 80 μm electrode heights, respectively. The resulting aspect ratios (h/w_g) of the VACNT electrodes ranged from 0.2 to 5.3. The aspect ratio was limited by the height to which VACNT forests could grow without tipping over, causing an electrical short between the electrodes (see more details on VACNT growth stability in Appendix F). This limiting height was a function of the electrode width (w_e) and likely

also influenced by the gap width (w_g); an 80 μm height approached the upper limit for the smaller electrode design (w_e = 20 μm, w_g = 15 μm). Taller electrodes could be made by increasing w_e, but sensitivity may also be affected because of the increase of underutilized surface area within the electrode.

4.4.3 Cyclic Voltammetry (CV)

By sweeping the applied potential, CV can give important information about the geometry and electroactivity of an electrode. Figure 4-3A shows cyclic voltammograms of VACNT electrodes of varying heights (5, 20, and 80 μm) at a constant scan rate of 1000 mV/s in a static 50 μL droplet of ferricyanide solution. The overall shape of the curves is typical for the single electron electrochemical reaction involving ferricyanide, having anodic and cathodic peaks in current. The peaks are caused by a balance between reaction kinetics and diffusion from the solution and are symmetric about 0 V because the reference is to a VACNT electrode and not a dedicated reference electrode such as Ag/AgCl.

Figure 4-3A shows that VACNT height causes a significant difference in the peak current, with the 80 μm peak current being about 7.2x greater than the 5 μm. The double layer capacitance also increases with increasing VACNT height, which is manifest by the increase in separation of the curves in the range of ± 0.2 to 0.6 V in Figure 4-3A. The electroactive surface area of an electrode is linearly proportional to the peak current (i_p) as given by the Randles-Sevcik equation at 25 °C:

$$i_p = (2.69 \text{x} 10^5) n^{3/2} A D^{1/2} C v^{1/2} \tag{4-1}$$

where n is the number of electrons transferred (n=1), A is the electroactive area of the electrode (units of cm^2), D is the diffusion coefficient of ferricyanide ($7.2 \text{x} 10^{-6}$ cm^2/s), C is the ferricyanide concentration (5 mM or $5 \text{x} 10^{-6}$ mol/cm^3), and v is the scan rate (0.125 to 1.25 V/s). The only

variable that is not well defined is the electrode surface area. The 2D geometric area of the electrode pattern is known to be 0.022 cm² ($30Lw_e$), but the exact surface area of the electrode is not known because of the porous nature of the VACNTs. The calculated electroactive surface areas for the 80, 20, and 5 µm tall VACNTs were 0.33, 0.13, and 0.046 cm², respectively. Thus, the electroactive surface area of the 80 µm tall electrode was 15x larger than the 2D geometric area, with the actual surface area likely being even higher because of the electrode porosity.
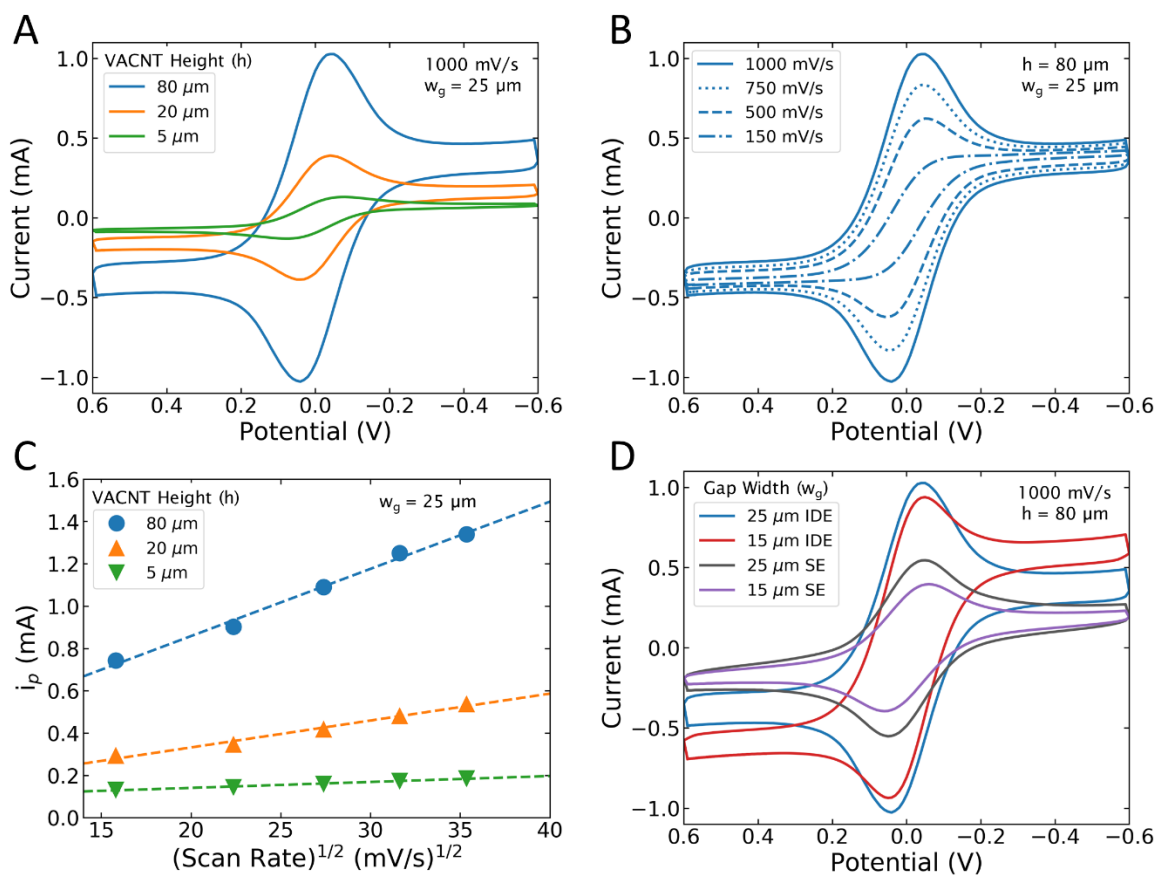
Figure 4-3: Cyclic voltammograms of VACNT electrodes in ferricyanide solution. (A) 80, 20, and 5 µm tall VACNT IDEs (w_g = 25 µm) at a scan rate of 1000 mV/s. (B) 80 µm tall VACNT IDE (w_g = 25 µm) at scan rates of 1000, 750, 500, and 150 mV/s. (C) Peak current i_p with the square root of scan rate for 80, 20, and 5 µm tall VACNTs. (D) 80 µm tall VACNT IDEs and SEs with w_g of 25 and 15 µm at a scan rate of 1000 mV/s.

The peak current increased with scan rate, as can be seen in Figure 4-3B for 80 μm tall VACNTs. It is interesting to note that the shape of the CV curve transitions from prominent peaks at high scan rates to a more sigmoidal shape with no peak at the lowest scan rate. This occurs because the electrodes are close enough together to cause a diffusion limited scenario at slower scan rates, typical of microelectrode arrays. The peak-to-peak potential separation was about 85 mV, which is close to the ideal Nernstian peak separation of 59 mV. The peak-to-peak separation for other CNT-based electrochemical sensors is typically reported at about 80-100 mV [116, 117]. According to Equation 1, the peak current should be linearly proportional to the square root of scan rate, which is plotted in Figure 4-3C for the three different VACNT heights. This linearity, combined with the fact that the peak-to-peak potential separation did not increase with increasing scan rate (see Figure 4-3B), confirms that the VACNT electrode and the electrochemical reaction experience fast, reversible kinetic behavior [118].

Figure 4-3D shows cyclic voltammograms of various 80 μm tall VACNT electrode designs. The blue curve is the same IDE geometry shown in Figure 4-3A and B, with $w_g = 25$ μm. An IDE with $w_g = 15$ μm (red curve) exhibited a larger peak current than the $w_g = 25$ μm IDE (relative to the baseline scan current). Thus, the 15 μm IDE had the highest electroactive surface area at 0.36 cm^2 while having a smaller 2D area of 0.018 cm^2, resulting in a 20x increase in electroactive surface area relative to a planar IDE. The peak currents for the SE curves (gray and purple) in Figure 4-3D are significantly lower than the IDEs. Even though the geometric dimensions and actual surface areas are the same for the IDE and SE configurations, the long winding electrodes in the SE configuration appears to reduce the effectiveness of the available area, perhaps because of the ohmic resistance along the lengthy meandering electrode. This reduced effectiveness of the SE surface area is opposite to the finding that SEs improve performance of capacitive sensors

[112], suggesting that SEs may not be as suitable for impedimetric sensors as they were for capacitive sensors. Additional CV data that shows the effect of scan rate on each geometry is found in Figure D-2 (Appendix D).

4.4.4   EIS Characterization

Nyquist plots are a convenient way to show the results from EIS, where imaginary impedance (-Z") is plotted with respect to real impedance (Z') over a range of frequencies. Nyquist plots for 80, 20, and 5 μm tall IDEs are shown in Figure 4-4A, where the impact of VACNT height on the baseline EIS measurement is evident by the change in magnitude of the semi-circular curves. The impedance was much larger for the 5 μm tall VACNTs than for the 80 μm tall VACNTs, an observation that correlates well with the larger current observed from the CV data (Figure 4-3A) as a result of the higher surface area. Figure 4-4B is a zoomed in view of the bottom left of the large semi-circles from Figure 4-4A to highlight a second, smaller semi-circular curve. These smaller semi-circles follow the same trend as the larger semi-circles, where the impedance of the 5 μm tall VACNTs was larger than the impedance of the 80 μm tall VACNTs. The data markers in the Nyquist plots in Figure 4-4 are the measured experimental EIS results for VACNT IDEs taken after EDC/NHS chemical activation but before the addition of streptavidin or biotin.

The inset of Figure 4-4B shows an equivalent electrical circuit that represents the observed behavior. Each semi-circular shape in the Nyquist plot is representative of a resistance-capacitor time constant; as observed in Figure 4-4, two time constants are necessary to describe the sensor behavior. The equivalent circuit uses constant phase elements (CPEs) in place of capacitors because the semi-circles are depressed, which is more apparent when the axes of the Nyquist plot have an equivalent scale (see Figure D-3 in Appendix D). The location of resistance R_0 is shown in Figure 4-4A and represents of the resistance in the Cr electrical leads. As R_0 varied between

samples and between electrical probe positioning for each test, Nyquist plots were biased by subtracting out this resistance to so that the results could be presented clearly (see x-axis Figure 4-4B).
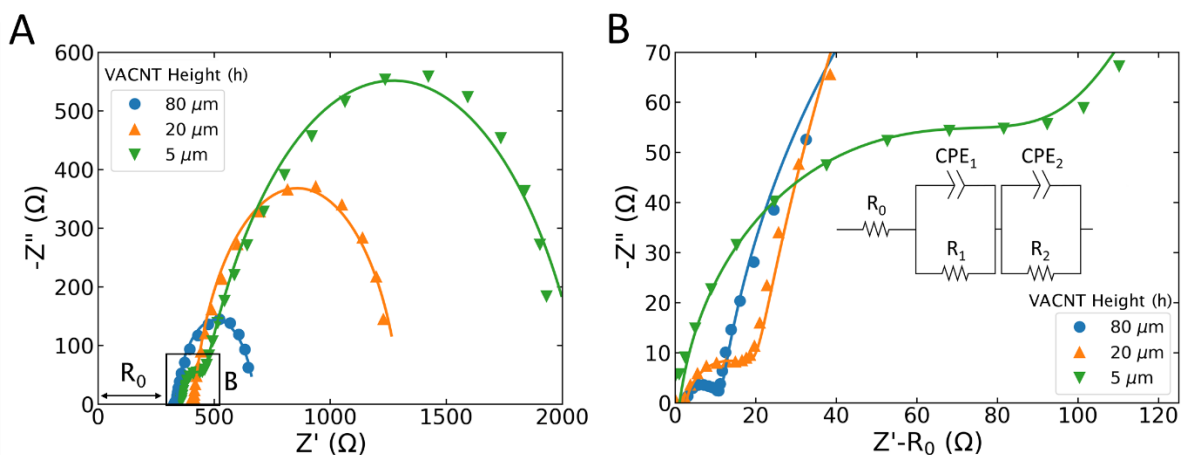
Figure 4-4: Experimental (markers) and simulated (lines) Nyquist plots of VACNT IDEs (w_g = 25 μm). (A) 80, 20, and 5 μm tall VACNTs with no streptavidin/biotin. (B) Zoomed in view of Figure 4-4A normalized by R_o, highlighting the trends for the first semi-circle. Inset: equivalent circuit used to curve fit experimental data.

The first time constant (CPE_1/R_1, small semi-circle) is observed at higher frequencies (approximately 70 – 10,000 Hz) and is associated with ferricyanide kinetics at the VACNT electrode surface, including charge transfer resistance and double layer capacitance. The second time constant (CPE_2/R_2, large semi-circle) is observed at lower frequencies (approximately 0.1 – 70 Hz) and is related to the diffusion of ferricyanide to and from the VACNT electrode surface. The IDE geometry has finite diffusion between the electrodes, causing the shape of the impedance in a Nyquist plot to bend in an arc instead extend linearly as is the case in semi-infinite diffusion [119]. Although a traditional Warburg element does not apply (semi-infinite only), the diffusion component could also be modeled by an open finite-length Warburg element or a finite-length

CPE element, with CPEs being able to better fit experimental data as shown by Figure D-4 in Appendix D [119]. A similar equivalent circuit with two CPE/R pairs is also used to model lithium-ion batteries, where the first time constant is attributed to an interfacial layer and the second time constant is attributed to charge transfer resistance and double layer capacitance [120]. Our previous VACNT sensor had a large semi-circle at high frequencies because of capacitance along the VACNT electrical leads [105], but that feature was not observed when using underlying Cr electrical leads. The equivalent circuit in Figure 4-4B was used to curve fit the experimental EIS data with EIS Spectrum Analyzer software and the simulated results are plotted as the solid lines in Figure 4-4. The values of curve fit equivalent circuit elements for VACNT IDE heights of 5, 20, and 80 μm are given in Table D-1 of Appendix D. The simulated results matched the experimental results with reasonable accuracy.

4.4.5   Functionalization of F-SA and Binding of F-biotin

It has previously been shown by Raman spectroscopy that VACNTs coated with amorphous carbon have a high number of surface defects, an attribute favorable for increasing the number of sites where proteins can bind and increasing charge transfer during electrochemical measurements [105]. Due to the addition of amorphous carbon to the VACNTs, a large number of defect sites are present that host carboxyl groups (COOH) on the electrode surface, as illustrated in Figure 4-5A. These carboxyl groups were activated by EDC/NHS chemistry to allow fluorescently tagged streptavidin (F-SA) to covalently bond to the VACNTs (Figure 4-5B). Fluorescently tagged biotin (F-biotin) was then bound to the F-SA, as biotin binds to streptavidin in one of the strongest known non-covalent bonds between a protein and a ligand [115]. The VACNT electrode with F-SA and F-biotin is represented in Figure 4-5C, noting that up to 4 F-biotin molecules can bind with a single F-SA protein.
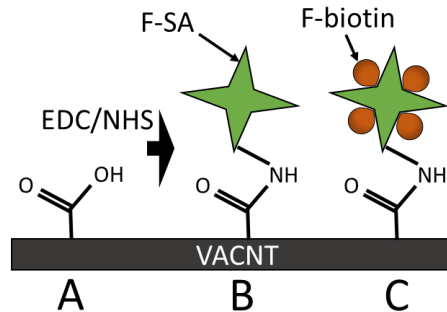
Figure 4-5: Schematic of binding used to characterize the VACNT sensors. (A) Carboxyl groups (COOH) from carbon-infiltrated VACNTs. (B) F-SA (streptavidin) covalently bound to VACNTs using EDC/NHS chemistry. (C) F-biotin bound to streptavidin.

Because the fluorescent dye only has 2% of the mass of the streptavidin, the impedance and binding results are expected to be similar to unlabeled streptavidin. On the other hand, the molecular weight of the F-biotin is 921.5 g/mol, about 3.8 times larger than unlabeled biotin at 244.3 g/mol, but still significantly smaller than streptavidin at 53,000 g/mol. F-biotin and F-SA have diameters of approximately 1.2 nm and 5 nm, respectfully [121]. Thus, F-biotin has a volume that is about 58x smaller than F-SA.

Fluorescently tagged molecules were used to enable a qualitative confirmation of the coverage of streptavidin and biotin on the VACNTs by fluorescent microscopy. Figure 4-6A shows the blue fluorescence of F-SA on VACNT IDE electrode fingers and Figure 4-6B shows the red fluorescence of F-biotin bound to the F-SA on the same device. The protein-ligand binding appears efficient across the entire surface of the VACNTs as displayed in the top down view shown in Figure 4-6 for binding performed by a static droplet on the VACNTs with a concentration of 500 µg/mL F-SA and 100 µg/mL F-biotin. It should be noted that there was also some coverage on the substrate, but this appears black in the Figure 4-6 images because it is out of the microscope focal plane. This non-specific binding on the substrate does not seem to affect the sensor performance.
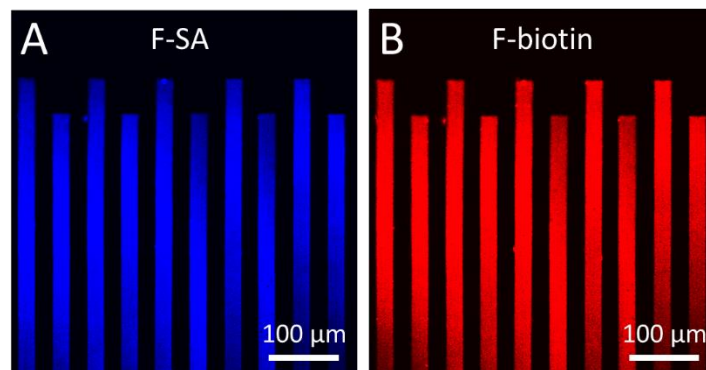
Figure 4-6: Fluorescent microscopy images confirming good coverage of (A) 500 μg/mL fluorescently tagged streptavidin (F-SA, blue) bound to 80 μm tall VACNT IDEs and (B) 100 μg/mL fluorescently tagged biotin (F-biotin, red) bound to F-SA. Note that F-SA and F-biotin are present in both images (same sensor), but fluoresce at different wavelengths.

While the functionalization and binding steps for the sensor were carried out with a static droplet on the VACNTs, the sensors were originally designed with an underlying Cr layer to allow for integration in a microfluidic channel to increase mass transfer of the molecules to the electrode surface. Our previous flow-through VACNTs electrodes for hydrogen peroxide [54] and glucose [88] detection showed that flowing conditions greatly improved amperometric signals. Microfluidic IDE sensors have also been shown to be more sensitive than static IDE sensors [122]. A 3D printed microfluidic flow channel was designed to be clamped over the sensor, with the Cr leads remaining exposed for electrical contact, as can be seen in Figure D-5 (Appendix D)). Although fluorescence showed better coverage using the microchannel (Figure D-6, Appendix D), initial electrochemical tests with the microfluidic channel demonstrated little improvement over static F-SA and F-biotin binding. Thus, static tests were chosen for experimental simplicity. However, the proof of concept was successful, such that the sensor could be incorporated into a microchannel. There likely exist applications where the microfluidic channel would be beneficial. We note that this integration can be achieved without loss in signal strength although further investigation is likely needed for optimal microfluidic conditions in a given application.

4.4.6   Biotin Sensing with IDEs

The impedance change associated with F-SA and F-biotin binding to a sample sensor surface is shown in Figure 4-7A and B for an 80 μm tall VACNT IDE. As shown in Figure 4-7A, there was a slight change observed in the resistance of the diffusion-driven large semi-circles when adding F-SA and F-biotin to the VACNTs (1.8% F-SA, 3.5% F-SA+F-biotin), but there was a much larger change observed in the resistance of the kinetics-driven small semi-circles shown in Figure 4-7B (32% F-SA, 138% F-SA+F-biotin). Thus, it is advantageous to focus on the changes that occur at the higher frequencies associated with the kinetics at the electrode surface.

Two options were considered for monitoring changes in the small semi-circle in response to molecules bound to the surface. The first and more direct option is to use impedance data measured at a single frequency. Specifically, the imaginary component of impedance Z" exhibited the largest relative change when F-biotin was bound to the VACNTs. Figure 4-7C shows the relative change in imaginary impedance at 147 Hz for 80, 20, and 5 μm tall VACNTs for different concentrations of F-biotin, where the percent change is measured relative to the imaginary impedance at 147 Hz after functionalizing with F-SA. The percent change in imaginary impedance was calculated across all measured frequencies and it was determined that 147 Hz gave the highest signal for all heights. The location of the 147 Hz impedance is on the right side of the small semi-circle, as shown by the data markers outlined in black in Figure 4-7B. The second option for monitoring changes is shown in Figure 4-7D, where the relative change in resistance R_1 from the equivalent circuit model is plotted for different F-biotin concentration for 80, 20, and 5 μm tall VACNTs. Because this method uses an equivalent circuit resistance, the fitted parameter accounts for all the measured frequencies instead of just a single frequency. The single frequency method and the equivalent circuit method with curve fit parameters give relative changes that follow a

similar trend and are comparable in magnitude. The relative change in imaginary impedance at 147 Hz generally gave a higher signal than the change in R_1 resistance, therefore the results for all subsequent geometries are reported only in terms of relative imaginary impedance change. The data in Figure 4-7C and D represent the average of three sensors, with the error bars indicating the standard deviation.
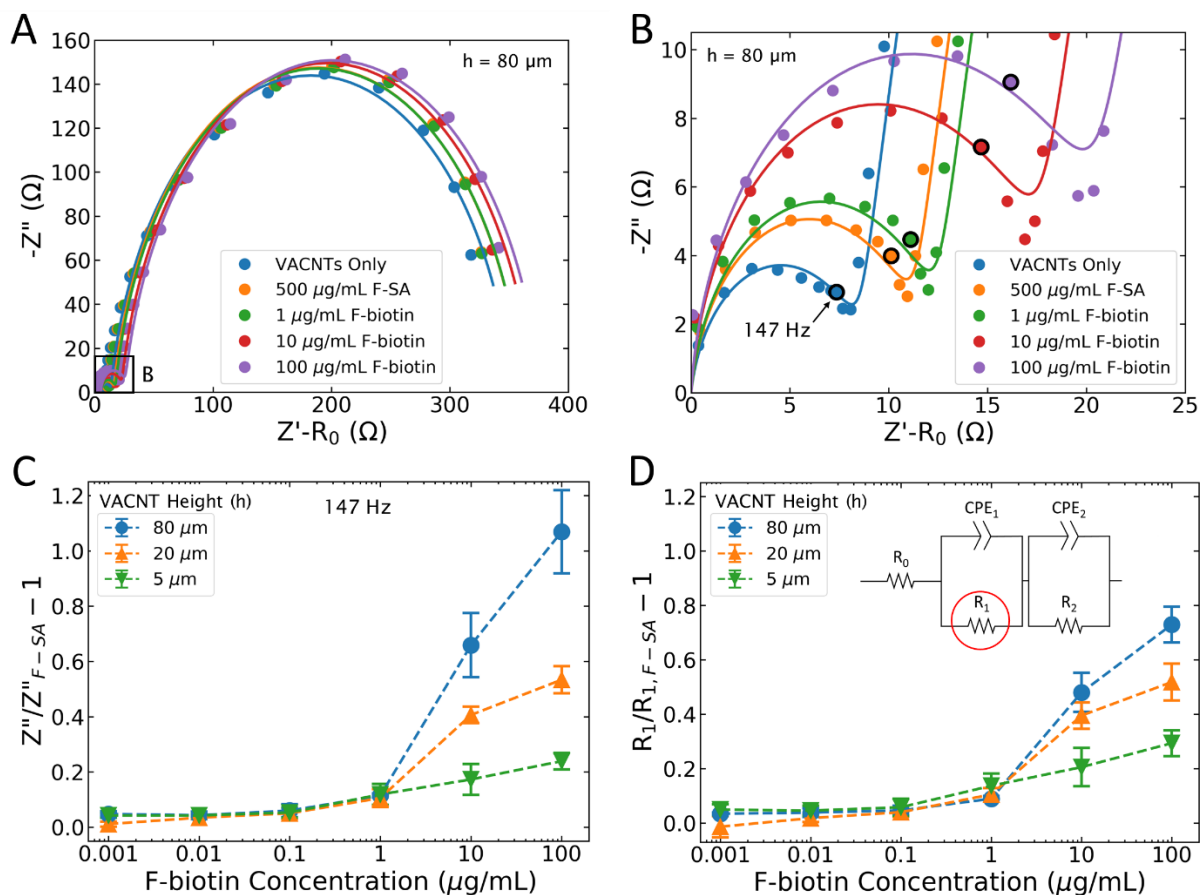
Figure 4-7: (A) 80 µm tall VACNT IDEs (w_g = 25 µm) with subsequent addition of 500 µg/mL F-SA and 1, 10, and 100 µg/mL F-biotin. (B) Zoomed in view of the first semi-circle of Figure 7A, with 147 Hz marked with a black outline. Relative change in (C) imaginary impedance at 147 Hz and (D) R_1 resistance from equivalent circuit as function of F-biotin concentration for 80, 20, and 5 µm tall VACNT IDEs. The error bars represent the standard deviation for three different sensors.

In Figure 4-7C and D it can be seen that the changes in impedance were small at lower concentrations of F-biotin (1 ng/mL to 1 µg/mL), and then there was a sudden spike in impedance at 10 µg/mL F-biotin, potentially leading to two linear sensing regions. While the exact cause of this phenomenon is unknown, it is possible that higher concentrations of F-biotin allow the molecules to better penetrate the porous VACNT electrode because of a higher concentration gradient, thus utilizing more of the surface area in between VACNTs. The 80 µm VACNTs provided an average change in imaginary impedance of 7% from $0.001 - 1$ µg/mL F-biotin and an average change of 95% from $1 - 100$ µg/mL F-biotin, with an overall maximum change of imaginary impedance of 107% relative to F-SA at 100 µg/mL F-biotin. The tall VACNTs (80 µm) generally demonstrated a larger relative change in impedance with F-SA and F-biotin, likely due to the additional surface area compared to the shorter electrodes and because the baseline impedance of the bare VACNTs was the smallest (see Figure 4-4B).

4.4.7 Electrode Geometry

EIS data shown up to this point has been for IDEs with $w_g = 25$ µm. The SE design shown in Figure 4-1B was explored as a potential alternative design to the more traditional IDE as it has previously been shown to exhibit a large signal change associated with capacitance [112]. Electrodes with $w_g = 15$ µm were also tested, as closely spaced electrodes generally provide better sensitivity.

Figure 4-8A shows Nyquist plots for 80 µm tall IDEs and SEs with w_g of 25 and 15 µm having F-SA and F-biotin bound to the VACNTs. The impedance was significantly larger for the SEs, with the large semi-circle impedance related to diffusion being about 5x larger than that for the IDEs. The resistance for both the IDE and SE with $w_g = 15$ µm was reduced relative to $w_g = 25$ µm, confirming a shorter diffusion length with a smaller gap between electrodes. The inset of

Figure 4-8A shows that the small semi-circle resistances related to kinetics for the SEs were larger in magnitude than the resistance of IDEs.
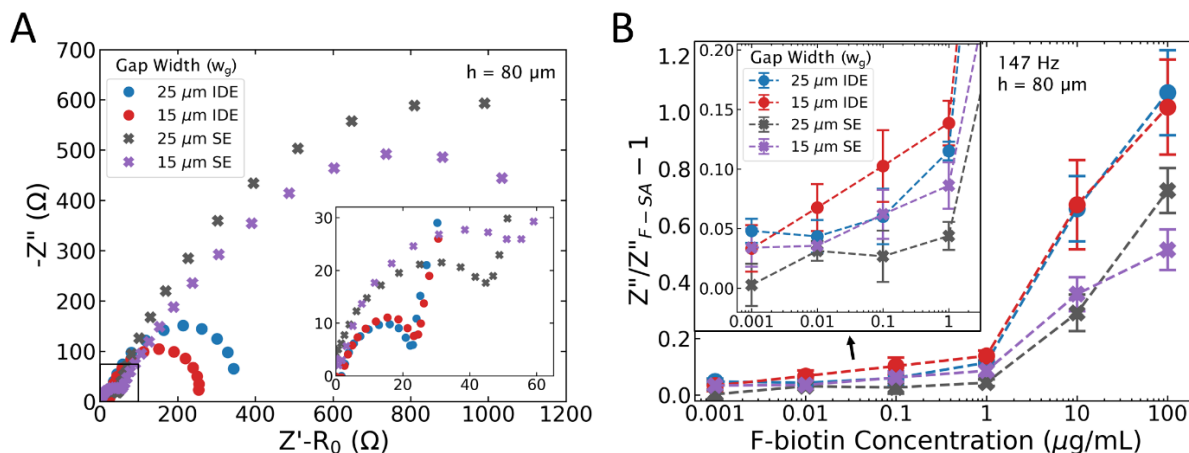
Figure 4-8: (A) Nyquist plots for 80 μm tall VACNT IDEs and SEs with w_g of 15 and 25 μm. Inset shows zoomed in view of smaller semi-circles near the origin. (B) Relative change in imaginary impedance Z" at 147 Hz as a function of F-biotin concentration for 80 μm tall VACNT IDEs and SEs with w_g of 15 and 25 μm. Inset shows close up of F-biotin concentrations from 1 ng/mL to 1 μg/mL. The error bars represent the standard deviation for three different sensors.

The relative change in imaginary impedance with F-biotin concentration is shown in Figure 4-8B for the same geometric configurations shown in Figure 4-8A. The tracking frequency that provided that largest change in imaginary impedance remained at 147 Hz for both IDEs and SEs. A very similar trend was observed for each geometry, with a large change in impedance observed with increasing concentration above 1 μg/mL F-biotin. The IDEs were shown to have a higher change in impedance than SEs, especially at higher F-biotin concentrations where the two IDEs had very similar changes in impedance. The inset in Figure 4-8B shows that the impedance still increased with increasing F-biotin concentrations below 1 μg/mL, with the IDE of w_g = 15 μm having the highest sensitivity and also being the most linear among the geometries tested. Thus,

there were two linear regions, one from 1 ng/mL to 1 µg/mL and another from 1 µg/mL to 100 µg/mL. Two different linear ranges for detection have been reported by others for amperometric and impedimetric sensing, but the slope typically is more gradual at higher concentrations as the electrode becomes saturated with analyte. A detection limit of 1 ng/mL is close to the detection limit of other biotin sensors reported in literature [123, 124].

Modest changes in the sensing signal were observed at F-biotin concentrations below 1 µg/mL. One potential reason is that F-biotin is a small molecule, much smaller than proteins, so that the change with concentration is likely smaller than for larger protein molecules. The VACNT IDEs were previously shown to have a limit of detection in the picomolar range when detecting oral cancer biomarkers [105], instead of in the nanomolar range that is here observed with F-biotin. Exploration of the effect of molecule size, as well as the investigation of non-specific binding, are potential extensions of this work. The main goal of the current work is to examine the influence of height for very tall VACNT electrodes and compare the geometric influence of these devices for a representative protein model.

4.5   Conclusions

This work has characterized porous, 3D VACNTs electrodes for impedance-based biosensing. Electrode height was shown to have a large impact on CV and EIS curves, with tall 80 µm VACNTs having the highest calculated electroactive surface area (approximately 15x the 2D geometric area) and thus resulting in the smallest baseline kinetic resistance as seen through Nyquist plots. The representative protein streptavidin was functionalized onto VACNT electrodes for detection of biotin and good coverage was confirmed by fluorescence microscopy. EIS was used to measure the change in impedance across electrodes for different biotin concentrations. Two linear sensing regions are observed for all electrode geometries and IDEs had higher

sensitivity than SEs. The relative change in imaginary impedance from F-biotin was shown to be as high as 107% for IDEs. The geometry with the highest sensitivity and the most linear sensing region was an 80 μm tall VACNT IDE with a gap width of 15 μm, enabling a limit of detection of 1 ng/mL F-biotin.

Although this biosensing platform is shown with streptavidin and biotin, it could be extended to other proteins, antibodies, viruses, and bacteria depending on surface functionalization. By having multiple sensors in series, it would be possible to simultaneously detect many different target analytes. It is expected that this structure and sensing approach will be viable for a range of electrochemical sensing, particularly in medical diagnostics.

4.6 Experimental Section

4.6.1 Electrode Fabrication

Detailed fabrication processes are found in Appendix A (summarized here) and a cost estimate of sensor fabrication is found in Appendix G. Photolithography was used to pattern positive photoresist (AZ3330) on a 100 mm diameter, oxidized silicon (Si) wafer (1 μm thick oxide, see Figure 4-2A for processing). Patterned photoresist was used to create the electrode designs from Figure 4-1 and the Cr electrical leads for each electrode (13 mm x 0.5 mm). A 75 nm layer of Cr was deposited onto the patterned photoresist by e-beam evaporation. A lift-off process was performed by sonication in N-methyl-2-pyrrolidone (NMP) for 30 min, leaving only patterned Cr on the oxidized wafer. In this manner, Cr was deposited below all 3D electrode regions and as electrical leads to the sensor electrodes. After covering the contact pads to the electrical leads with permanent marker, 150 nm of aluminum oxide (Al_2O_3) was deposited by e-beam evaporation. NMP sonication was performed for 5 min to expose the contact pads by removing the marker ink

and Al_2O_3 for electrical connects. Planar, Cr electrical leads underneath Al_2O_3 can be seen in Figure 4-2B as the lighter region on the substrate. A second photolithography process was used to cover the wafer in photoresist except in regions where sensor fingers are to be constructed. A 7 nm film of iron (Fe) was thermally evaporated onto the patterned photoresist, followed by sonication in NMP for 15 minutes leaving patterned Fe on a portion of the Al_2O_3/Cr layer. In this manner, the catalyst for CNT growth was patterned so that growth would only occur in the 3D electrode regions. The patterned wafer was diced into 16.1 mm x 8 mm rectangles using a dicing saw with a diamond-coated blade.

VACNT growth methods were similar to previously published protocols [19, 54]. VACNTs were grown by chemical vapor deposition (CVD) in a 1-inch diameter Lindberg/Blue M tube furnace with flowing hydrogen (H_2, 311 sccm) and ethylene (C_2H_4, 338 sccm) at 750 °C for 5, 30, or 120 s. The temperature was then raised to 900 °C and the C_2H_4 flow rate reduced to 193 sccm to infiltrate (coat) the VACNTs with amorphous carbon for 60 s. This infiltration process strengthened the VACNTs to create mechanically sturdy, porous microstructures (see Figure 4-2B and C). The electrodes were oxygen plasma etched (250 W, 300 mTorr, 30 – 60 s) until the two electrodes were electrically isolated using a Technics Planar Etch II machine.

4.6.2 Electrochemical Measurements

All electrochemical experiments were performed with a CH Instruments (CHI) 660E Potentiostat/Galvanostat in a two-electrode configuration where one VACNT electrode was the working electrode and the other VACNT electrode was the counter/reference electrode. The Cr contact pads were contacted by micro-manipulation probes. The electrolyte was a static 50 μL droplet of 5 mM potassium ferricyanide ($K_3[Fe(CN)_6]$), 5 mM potassium ferrocyanide ($K_4[Fe(CN)_6]$), and 100 mM KCl in phosphate buffered saline (PBS, 1X, pH 7.4, Fisher Scientific).

Cyclic voltammetry (CV) was performed between -600 mV and 600 mV relative to the VACNT electrode at scan rates of 150 mV/s to 1250 mV/s. Ohmic drop correction was used to account for the resistance within the Cr electrical leads (about 300 Ω). The frequencies for electrochemical impedance spectroscopy (EIS) ranged from 10,000 Hz to 0.1 Hz, with an input amplitude of 10 mV. Appendix A.14 provides additional procedural information and Appendix H gives details for checking the EIS capabilities of a potentiostat.

4.6.3 Streptavidin Functionalization

The VACNT electrodes were incubated in a 50 µL droplet of 100 mM EDC and 100 mM NHS in 0.1 M 2-(N-morpholino) ethanesulfonic acid (MES, pH 4.7, Thermo Scientific 28390) for 60 min. The VACNT electrodes were then rinsed and soaked in PBS for 20 min. A 20 µL droplet of 500 µg/mL, fluorescently tagged Atto 425 streptavidin (F-SA, Sigma Aldrich 09260) in PBS was placed on the EDC/NHS-activated VACNTs for 60 min to bind the SA protein to the VACNTs (Figure 4-5B). Electrodes were then rinsed and allowed to soak in PBS for 40 min. While the stock F-SA solution was stored at 4 °C, all functionalization steps and soakings were performed at room temperature.

4.6.4 Biotin Sensing

A 20 µL droplet of 1 ng/mL fluorescently tagged Atto 565 biotin (F-biotin, Sigma-Aldrich 92637) in PBS was placed on F-SA/VACNT sensors for 20 min. The sensor was then rinsed and allowed to soak in 50 µL of PBS for 1 minute, after which electrochemical measurements were taken. The concentration of F-biotin was incrementally increased for each measurement following the same procedure above for each concentration (0.01, 0.1, 1, 10, and 100 µg/mL).

4.6.5 Fluorescence

Fluorescence measurements were performed with an Olympus FluoView FV1000 confocal laser scanning microscope (see Section A.13 in Appendix A). Wavelengths of 405 and 543 nm were used to excite the F-SA and F-biotin, respectively. The two fluorescent markers have very little overlap in absorption and emission so that the intensity of each is nearly independent of the other. Specific microscope settings included: 20x magnification, 12% laser power, and 200 µm aperture size.

4.6.6 Supporting Information

Supporting Information is available in Appendix D.

5   CONCLUSIONS

This dissertation has characterized electrochemical sensors that are enhanced by convection and by 3D electrodes made from high surface area VACNTs. Conclusions from the amperometric flow-through sensors from Chapters 2 and 3 and the impedimetric interdigitated electrodes from Chapter 4 are discussed below, including potential future work in each area.

5.1   Flow-Through VACNT Sensors

Chapters 2 and 3 investigated flow-through amperometric sensors made of VACNTs that form arrays of aligned, parallel microchannels. Convection was shown to increase the sensitivity of high aspect ratio VACNT electrochemical sensors by using high flow rates in microchannels where concentration boundary layers were confined. The porous nature of the free-standing VACNT electrode provided high surface area for analyte to electrochemically react, which also aided in improving the sensitivity of the amperometric sensors.

Chapter 2 demonstrated the performance of flow-through VACNT microchannel arrays by measuring the current generated by oxidizing hydrogen peroxide. Through-flow sensing oxidized over 90% of the hydrogen peroxide as it passed through the VACNT microchannels, producing drastically higher currents at lower velocities than stirring conditions. The high measured current resulted in a very high sensitivity, allowing for the detection of analyte concentrations in the nM range.

In Chapter 3, the flow-through VACNT architecture was developed further for the detection of glucose using a unique non-enzymatic approach with the chemical methyl viologen. The effectiveness of using methyl viologen as the reacting agent for glucose detection was shown by comparing the results to the results obtained by using VACNTs with traditional enzymatic functionalization strategies. The measured current densities with methyl viologen were higher than theoretically possible with enzymatic reactions, generating an average of 3.4 electrons per glucose molecule on average. The high current densities obtained were linear with both flow rate and glucose concentration in the 0.25–200 µM range, while also having minimal effect from common interfering species by operating at a low potential. The additional electrons made available with MV may also be useful in increasing power output of glucose-based biofuel cells. However, methyl viologen glucose sensing is potentially limited due to the chemical reaction that must take place at an elevated temperature in an oxygen-free environment for several minutes before passing though the sensing electrode. The VACNT sensor was also scaled down in size to enable the detection of glucose in small volumes of only 200 µL in the concentration range typical of saliva.

5.2   VACNT IDEs

Chapter 4 characterized porous, 3D VACNT electrodes with planar metallic electrical leads for impedimetric biosensing. The change in impedance was measured using electrochemical impedance spectroscopy with the representative protein streptavidin functionalized to the VACNT electrode for detection of biotin. Electrode height was shown to have a large impact on sensor performance, with tall 80 µm VACNTs having an electroactive surface area that was 15x the area of the 2D electrode pattern. Two linear sensing regions are observed for all electrode geometries, but interdigitated electrodes were more sensitive than serpentine electrodes. The relative change in imaginary impedance from biotin was shown to be as high as 107%. The geometry with the

highest sensitivity and the most linear sensing region was an 80 μm tall VACNT IDE with a gap width of 15 μm, enabling a limit of detection of 1 ng/mL biotin.

Beyond what is presented in Chapter 4, there was also significant collaboration with Iowa State University in the development of VACNT electrodes for impedimetric sensing. Collaborative work that investigated the detection of human cancerous inhibitor PP2A (CIP2A) with VACNT IDEs is published in Biosensors and Bioelectronics [105]. In this collaborative work, a similar 3D VACNT electrode was fabricated that was made completely out of VACNTs, instead of incorporating underlying metallic electrical leads as in Chapter 4. The VACNT IDE was functionalized with an antibody specific to CIP2A, a salivary protein that is associated with a variety of malignancies such as oral, breast, and multiple myeloma cancers. The sensor was capable of label-free detection of CIP2A with a linear sensing range of 1 to 100 pg/mL within saliva supernatant (see Figure I-1 in Appendix I). This sensing range is more sensitive than the corresponding sensing range of CIP2A enzyme linked immunosorbent assay (ELISA). The sensor also provided quick results in less than 35 minutes, demonstrating great promise for point-of-care testing. These results help show promise for rapid cancer screening such as early-stage diagnosis of oral cancer at a dentist's office.

Additional work in collaboration with Iowa State University was performed for the detection of the cytokines interferon gamma (IFN-γ) and Interleukin 10 (IL-10). These molecules are useful for the early detection of Mycobacterium Avium subspecies Paratuberculosis (MAP), which is an infection that can lead to Johne's disease in cattle. Using similar VACNT IDE structures that were used for CIP2A, the sensors were capable of selective detection of both IL-10 and IFN-γ within diluted bovine implant supernatant. The IL-10 sensor had a linear sensing range of 0.1 to 30 pg/ml and the IFN-γ sensor had a linear sensing range 50-1000 pg/ml. These highly

sensitive detection ranges combined with a fast response time of less than 35 minutes demonstrate initial steps toward rapid, pen-side identification of cattle with MAP infection before physical symptoms of Johne's disease in cattle are present.

5.3   Future Work

5.3.1 Flow-Through VACNT Sensors

The work done with flow-through VACNT glucose sensors in Chapters 3 built upon the same VACNT structure used for characterization with hydrogen peroxide in Chapter 2. Future work with this flow-through VACNT design could include:

- Further work with enzymatic sensing, such as exploration of injection-based, small volume sensing with VACNT electrodes. A reduction in interfering species and an increase in sensitivity may be possible by having multiple VACNT microchannel arrays in series. For example, the first VACNT array could apply a constant potential to oxidize all the interfering species (or at least the majority of interfering species). Next, there could be a VACNT microchannel array functionalized with glucose oxidase (with no potential applied). Having a separate functionalized array would separate the chemical and electrochemical reactions allow for better sensitivity at higher flow rates. Then, finally, a third VACNT electrode would sense the generated hydrogen peroxide. Thus, having three VACNT arrays in series could allow the enzymatic sensor to have high sensitivity and operate at high potentials without having interference from other species in solution.

- Further work on miniaturization and integration with a microfluidic system. Much of the flow-through work presented in this dissertation involved large analyte solutions in the mL

range, but the glucose sensor was also shown to be effective with flow injection analysis using µL volumes of analyte in a reduced scale flow cell.

- Investigation into the pressure drop and optimization of sensor sensitivity to required pumping power. This could involve looking into a wider range of microchannel diameters and porosities, as determined by the amount of carbon infiltration.

- The strength of the VACNT microchannels and the maximum flow rate or pressure drop before failure.

- For methyl viologen applications, investigating the interference from carbohydrates other than glucose would be important.

- Testing real saliva samples that have been spiked with different concentrations of glucose, or testing saliva of volunteers before and after eating a meal to see how applicable the glucose sensor would be with real samples.

- Investigation into using the VACNT architecture as an electrode for fuel cell applications.

5.3.2   VACNT IDEs

The effectiveness of VACNT IDEs and the influence of geometry was explored in Chapter 4. The sensors can only be effective if they are functionalized with proteins or antibodies that can specifically target the desired analyte. Thus, an opportunity for future work lies in the ability to functionalize the VACNT for detection of different analyte. Further investigation is also needed into the coverage of the functionalized proteins throughout the IDE structure. By cleaving the silicon substrate, it may be possible to use the fluorescent microscope to image the side profile and the cross-section of the VACNT IDE to see if the proteins are penetrating the porous structure. As mentioned in section 5.2, work was done with Iowa State University for the detection of CIP2A,

IL-10, and IFN-γ with VACNT IDEs. The results from the work with IL-10 and IFN-γ are in preparation for publication. Future work could also involve detection of different target analyte such as other proteins, antibodies, viruses, and bacteria that have a selective binding mechanism that can be functionalized to the VACNT electrode.

To have a better understanding of the different elements in the equivalent circuit model, it would be beneficial to perform EIS experiments with different concentrations of ferricyanide solution. Changes in the Nyquist plot with variations in ferricyanide concentration would indicate which portion of the EIS data are impacted by concentration and are thus related to diffusional behavior.

The results from this dissertation and the collaborative work with Iowa State University have been for static functionalization, incubation, and sensing. However, microfluidic sensors benefit from high sensitivity and portability and initial work showed that integration with a 3D printed microchannel was possible with the VACNT IDEs that incorporated underlying metallic electrical leads. Further work is needed to integrate the VACNT IDEs into a portable microfluidic test cell. Investigation is also needed to identify the applications where using the microchannel for functionalization and for binding target analyte would provide a higher sensitivity. Optimization of flow rates, deposition times, microfluidic flow cell geometry, are VACNT geometry are some of the important things that would need to be tested when further developing the microfluidic system. A microchannel would also provide a way simple way for multiple sensors to be used with the same sample volume to detect various different analyte. The ratio of different species in the same sample, such as IFN-γ and IL-10, can be informative in medical diagnostics. The impact of non-specific binding would also need to be investigated further, especially if detecting multiple analytes in a complex biological matrix.

VACNT IDEs are well-suited for miniaturization, large scale fabrication and potential incorporation into microfluidic channels for multiplex electrochemical sensing of a wide variety of target analytes from a single sample. By using minimal equipment such as a portable potentiostat (similar to a glucometer), point of care results can be obtained by non-technical staff. Thus, future work could involve integrating the sensors with a microfluidic channel and a portable potentiostat to show the application of VACNT IDEs for a range of electrochemical sensing that will be beneficial in medical diagnostics.

REFERENCES

1. *IDF Diabetes Atlas, 8th edn.* 2017, Brussels, Belgium: International Diabetes Federation.

2. Klonoff, D.C., D. Ahn, and A. Drincic, Continuous Glucose Monitoring: A Review of the Technology and Clinical Use, *Diabetes Research and Clinical Practice*, 2017, 133: 178-192.

3. Viswanath, B., C.S. Choi, K. Lee, and S. Kim, Recent Trends in the Development of Diagnostic Tools for Diabetes Mellitus Using Patient Saliva, *TrAC Trends in Analytical Chemistry*, 2017, 89: 60-67.

4. Gupta, S., S.V. Sandhu, H. Bansal, and D. Sharma, Comparison of Salivary and Serum Glucose Levels in Diabetic Patients, *Journal of Diabetes Science and Technology*, 2015, 9(1): 91-96.

5. *Blood Glucose Testing and Monitoring*. 2015 [cited 1 May 2020]; Available from: http://www.diabetescommunity.com/management/blood-glucose-testing.html.

6. Pejcic, B., R.D. Marco, and G. Parkinson, The role of biosensors in the detection of emerging infectious diseases, *Analyst*, 2006, 131(10): 1079-1090.

7. Sawant, S.N., *13 - Development of Biosensors From Biopolymer Composites*, in *Biopolymer Composites in Electronics*, K.K. Sadasivuni, et al., Editors. 2017, Elsevier. p. 353-383.

8. Bandodkar, A.J., I. Jeerapan, J.-M. You, R. Nuñez-Flores, and J. Wang, Highly Stretchable Fully-Printed CNT-Based Electrochemical Sensors and Biofuel Cells: Combining Intrinsic and Design-Induced Stretchability, *Nano Letters*, 2016, 16(1): 721-727.

9. Zaidi, S.A. and J.H. Shin, Recent Developments in Nanostructure Based Electrochemical Glucose Sensors, *Talanta*, 2016, 149: 30-42.

10. Thévenot, D.R., K. Toth, R.A. Durst, and G.S. Wilson, Electrochemical biosensors: recommended definitions and classification1International Union of Pure and Applied Chemistry: Physical Chemistry Division, Commission I.7 (Biophysical Chemistry); Analytical Chemistry Division, Commission V.5 (Electroanalytical Chemistry).1, *Biosensors and Bioelectronics*, 2001, 16(1): 121-131.

11. Varshney, M., Y. Li, B. Srinivasan, and S. Tung, A label-free, microfluidics and interdigitated array microelectrode-based impedance biosensor in combination with nanoparticles

immunoseparation for detection of Escherichia coli O157:H7 in food samples, *Sensors and Actuators B: Chemical*, 2007, 128(1): 99-107.

12. Hall, S.B., E.A. Khudaish, and A.L. Hart, Electrochemical oxidation of hydrogen peroxide at platinum electrodes. Part 1. An adsorption-controlled mechanism, *Electrochimica Acta*, 1998, 43(5–6): 579-588.

13. Deng, J. and X. Jiang, Advances in Reagents Storage and Release in Self-Contained Point-of-Care Devices, *Advanced Materials Technologies*, 2019, 4(6): 1800625.

14. Alkire, R. and B. Gracon, Flow-Through Porous Electrodes, *Journal of The Electrochemical Society*, 1975, 122(12): 1594-1601.

15. Paulin, M., D. Hutin, and F. Coeuret, Theoretical and Experimental Study of Flow-Through Porous Electrodes, *Journal of The Electrochemical Society*, 1977, 124(2): 180-188.

16. Strohl, A.N. and D.J. Curran, Reticulated vitreous carbon flow-through electrodes, *Analytical Chemistry*, 1979, 51(3): 353-357.

17. Csoeregi, E., L. Gorton, G. Marko-Varga, A.J. Tuedoes, and W.T. Kok, Peroxidase-Modified Carbon Fiber Microelectrodes in Flow-Through Detection of Hydrogen Peroxide and Organic Peroxides, *Analytical Chemistry*, 1994, 66(21): 3604-3610.

18. Khayyami, M., G. Johansson, D. Kriz, B. Xie, P.-O. Larsson, and B. Danielsson, Flow-injection determination of trace hydrogen peroxide or glucose utilizing an amperometric biosensor based on glucose oxidase bound to a reticulated vitreous carbon electrode, *Talanta*, 1996, 43(6): 957-962.

19. Marr, K.M., B. Chen, E.J. Mootz, J. Geder, M. Pruessner, B.J. Melde, R.R. Vanfleet, I.L. Medintz, B.D. Iverson, and J.C. Claussen, High Aspect Ratio Carbon Nanotube Membranes Decorated with Pt Nanoparticle Urchins for Micro Underwater Vehicle Propulsion via H2O2 Decomposition, *ACS Nano*, 2015, 9(8): 7791-7803.

20. Amatatongchai, M., W. Sroysee, S. Chairam, and D. Nacapricha, Amperometric Flow Injection Analysis of Glucose Using Immobilized Glucose Oxidase on Nano-Composite Carbon Nanotubes-Platinum Nanoparticles Carbon Paste Electrode, *Talanta*, 2017, 166: 420-427.

21. Sattayasamitsathit, S., Y. Gu, K. Kaufmann, W. Jia, X. Xiao, M. Rodriguez, S. Minteer, J. Cha, D.B. Burckel, C. Wang, R. Polsky, and J. Wang, Highly Ordered Multilayered 3D Graphene Decorated with Metal Nanoparticles, *Journal of Materials Chemistry A*, 2013, 1(5): 1639-1645.

22. Chen, Z., W. Ren, L. Gao, B. Liu, S. Pei, and H.-M. Cheng, Three-dimensional flexible and conductive interconnected graphene networks grown by chemical vapour deposition, *Nature Materials*, 2011, 10(6): 424-428.

23. Claussen, J.C., A. Kumar, D.B. Jaroch, M.H. Khawaja, A.B. Hibbard, D.M. Porterfield, and T.S. Fisher, Nanostructuring Platinum Nanoparticles on Multilayered Graphene Petal Nanosheets for Electrochemical Biosensing, *Advanced Functional Materials*, 2012, 22(16): 3399-3405.

24. Meshkani, F. and M. Rezaei, Nickel catalyst supported on magnesium oxide with high surface area and plate-like shape: A highly stable and active catalyst in methane reforming with carbon dioxide, *Catalysis Communications*, 2011, 12(11): 1046-1050.

25. Bartley, J.K., C. Xu, R. Lloyd, D.I. Enache, D.W. Knight, and G.J. Hutchings, Simple method to synthesize high surface area magnesium oxide and its use as a heterogeneous base catalyst, *Applied Catalysis B: Environmental*, 2012, 128(0): 31-38.

26. Rezaei, M., M. Khajenoori, and B. Nematollahi, Synthesis of high surface area nanocrystalline MgO by pluronic P123 triblock copolymer surfactant, *Powder Technology*, 2011, 205(1–3): 112-116.

27. Hu, S., Y. Gong, Q. Xu, X. Liu, Q. Zhang, L. Zhang, and T. Dou, Highly selective formation of propylene from methanol over high-silica EU-1 zeolite catalyst, *Catalysis Communications*, 2012, 28(0): 95-99.

28. Liu, P., J. Wang, R. Wei, X. Ren, and X. Zhang, A Highly Efficient Hβ Zeolite Supported Pt Catalyst Promoted by Chromium for the Hydroisomerization of n-Heptane, *Catalysis Letters*, 2008, 126(3-4): 346-352.

29. Parsafard, N., M.H. Peyrovi, and M. Rashidzadeh, n-Heptane isomerization on a new kind of micro/mesoporous catalyst: Pt supported on HZSM-5/HMS, *Microporous and Mesoporous Materials*, 2014, 200(0): 190-198.

30. Schröper, F., D. Brüggemann, Y. Mourzina, B. Wolfrum, A. Offenhäusser, and D. Mayer, Analyzing the electroactive surface of gold nanopillars by electrochemical methods for electrode miniaturization, *Electrochimica Acta*, 2008, 53(21): 6265-6272.

31. Forrer, P., F. Schlottig, H. Siegenthaler, and M. Textor, Electrochemical preparation and surface properties of gold nanowire arrays formed by the template technique, *Journal of Applied Electrochemistry*, 2000, 30(5): 533-541.

32. Gupta, S., C.N. Murthy, and C.R. Prabha, Recent Advances in Carbon Nanotube Based Electrochemical Biosensors, *International Journal of Biological Macromolecules*, 2018, 108: 687-703.

33. Claussen, J.C., A.D. Franklin, A.U. Haque, D. Marshall Porterfield, and T.S. Fisher, Electrochemical Biosensor of Nanocube-Augmented Carbon Nanotube Networks, *ACS Nano*, 2009, 3(1): 37-44.

34. Ashkan, K., G. Nataliia, G. Maria, and K. Evgeny, Graphene-Functionalized 3D-Carbon Fiber Electrodes – Preparation and Electrochemical Characterization, *Electroanalysis*, 2016, 28(9): 1943-1946.

35. Lawal, A.T., Progress in Utilisation of Graphene for Electrochemical Biosensors, *Biosensors and Bioelectronics*, 2018, 106: 149-178.

36. Bollella, P., G. Fusco, C. Tortolini, G. Sanzò, G. Favero, L. Gorton, and R. Antiochia, Beyond Graphene: Electrochemical Sensors and Biosensors for Biomarkers Detection, *Biosensors and Bioelectronics*, 2017, 89: 152-166.

37. Dhara, K. and D.R. Mahapatra, Electrochemical Nonenzymatic Sensing of Glucose Using Advanced Nanomaterials, *Microchimica Acta*, 2018, 185(1): 49.

38. Tsentalovich, D.E., R.J. Headrick, F. Mirri, J. Hao, N. Behabtu, C.C. Young, and M. Pasquali, Influence of Carbon Nanotube Characteristics on Macroscopic Fiber Properties, *ACS Applied Materials & Interfaces*, 2017, 9(41): 36189-36198.

39. Kumar, S., R. Rani, N. Dilbaghi, K. Tankeshwar, and K.-H. Kim, Carbon Nanotubes: A Novel Material for Multifaceted Applications in Human Healthcare, *Chemical Society Reviews*, 2017, 46(1): 158-196.

40. Ahmad, R., N. Tripathy, M.-S. Ahn, and Y.-B. Hahn, Solution Process Synthesis of High Aspect Ratio ZnO Nanorods on Electrode Surface for Sensitive Electrochemical Detection of Uric Acid, *Scientific Reports*, 2017, 7: 46475.

41. Kim, D. and A.E. Herr, Protein immobilization techniques for microfluidic assays, *Biomicrofluidics*, 2013, 7(4): 041501.

42. Schnoor, M.H. and C.D. Vecitis, Quantitative Examination of Aqueous Ferrocyanide Oxidation in a Carbon Nanotube Electrochemical Filter: Effects of Flow Rate, Ionic Strength, and Cathode Material, *The Journal of Physical Chemistry C*, 2013, 117(6): 2855-2867.

43. Buffa, A., Y. Erel, and D. Mandler, Carbon Nanotube Based Flow-Through Electrochemical Cell for Electroanalysis, *Analytical Chemistry*, 2016, 88(22): 11007-11015.

44. Chiou, Y.-D., D.-S. Tsai, H.H. Lam, C.-h. Chang, K.-Y. Lee, and Y.-S. Huang, Cycle stability of the electrochemical capacitors patterned with vertically aligned carbon nanotubes in an LiPF6-based electrolyte, *Nanoscale*, 2013, 5(17): 8122-8129.

45. Hsia, B., J. Marschewski, S. Wang, J.B. In, C. Carraro, D. Poulikakos, C.P. Grigoropoulos, and R. Maboudian, Highly flexible, all solid-state micro-supercapacitors from vertically aligned carbon nanotubes, *Nanotechnology*, 2014, 25(5): 055401.

46. Liu, C.-C., D.-S. Tsai, W.-H. Chung, K.-W. Li, K.-Y. Lee, and Y.-S. Huang, Electrochemical micro-capacitors of patterned electrodes loaded with manganese oxide and carbon nanotubes, *Journal of Power Sources*, 2011, 196(13): 5761-5768.

47. Chen, G., B. Dodson, D.M. Hedges, S.C. Steffensen, J.N. Harb, C. Puleo, C. Galligan, J. Ashe, R.R. Vanfleet, and R.C. Davis, Fabrication of High Aspect Ratio Millimeter-Tall Free-Standing Carbon Nanotube-Based Microelectrode Arrays, *ACS Biomaterials Science & Engineering*, 2018, 4(5): 1900-1907.

48. Sassolas, A., L.J. Blum, and B.D. Leca-Bouvier, Immobilization Strategies to Develop Enzymatic Biosensors, *Biotechnology Advances*, 2012, 30(3): 489-511.

49. Shi, J., J.C. Claussen, E.S. McLamore, A. Ul Haque, D. Jaroch, A.R. Diggs, P. Calvo-Marzal, J.L. Rickus, and D. Marshall Porterfield, A Comparative Study of Enzyme Immobilization Strategies for Multi-Walled Carbon Nanotube Glucose Biosensors, *Nanotechnology*, 2011, 22(35): 1-10.

50. Luo, Y., F.-Y. Kong, C. Li, J.-J. Shi, W.-X. Lv, and W. Wang, One-pot Preparation of Reduced Graphene Oxide-Carbon Nanotube Decorated with Au Nanoparticles Based on Protein for Non-enzymatic Electrochemical Sensing of Glucose, *Sensors and Actuators B: Chemical*, 2016, 234: 625-632.

51. Watt, G.D., Kinetic Evaluation of the Viologen-Catalyzed Carbohydrate Oxidation Reaction for Fuel Cell Application, *Renewable Energy*, 2014, 63(Supplement C): 370-375.

52. Daniels, J.S. and N. Pourmand, Label-Free Impedance Biosensors: Opportunities and Challenges, *Electroanalysis*, 2007, 19(12): 1239-1257.

53. Ding, S., C. Mosher, X.Y. Lee, S.R. Das, A.A. Cargill, X. Tang, B. Chen, E.S. McLamore, C. Gomes, J.M. Hostetter, and J.C. Claussen, Rapid and Label-Free Detection of Interferon Gamma via an Electrochemical Aptasensor Comprising a Ternary Surface Monolayer on a Gold Interdigitated Electrode Array, *ACS Sensors*, 2017, 2(2): 210-217.

54. Brownlee, B.J., K.M. Marr, J.C. Claussen, and B.D. Iverson, Improving Sensitivity of Electrochemical Sensors with Convective Transport in Free-standing, Carbon Nanotube Structures, *Sensors and Actuators B: Chemical*, 2017, 246: 20-28.

55. Lopes, J.P., M.A. Alves, M.S.N. Oliveira, S.S.S. Cardoso, and A.E. Rodrigues, Internal mass transfer enhancement in flow-through catalytic membranes, *Chemical Engineering Science*, 2013, 104: 1090-1106.

56. Lyubovsky, M., H. Karim, P. Menacherry, S. Boorse, R. LaPierre, W.C. Pfefferle, and S. Roychoudhury, Complete and partial catalytic oxidation of methane over substrates with enhanced transport properties, *Catalysis Today*, 2003, 83(1–4): 183-197.

57. Bell, A.T., H.P. Calis, T.S. Everwijn, A.W. Gerritsen, C.M. Van Den Bleek, F. Goudriaan, and F.G. Van Dongen, Chemical Reaction Engineering: Science & TechnologyMass transfer characteristics of parallel passage reactors, *Chemical Engineering Science*, 1994, 49(24): 4289-4297.

58. Lodge, A.W., M.J. Lacey, M. Fitt, N. Garcia-Araez, and J.R. Owen, Critical appraisal on the role of catalysts for the oxygen reduction reaction in lithium-oxygen batteries, *Electrochimica Acta*, 2014, 140: 168-173.

59. Qiu, K. and Z.X. Guo, Hierarchically porous graphene sheets and graphitic carbon nitride intercalated composites for enhanced oxygen reduction reaction, *Journal of Materials Chemistry A*, 2014, 2(9): 3209-3215.

60. Solovev, A.A., Y. Mei, E. Bermúdez Ureña, G. Huang, and O.G. Schmidt, Catalytic Microtubular Jet Engines Self-Propelled by Accumulated Gas Bubbles, *Small*, 2009, 5(14): 1688-1692.

61. Soler, L., V. Magdanz, V.M. Fomin, S. Sanchez, and O.G. Schmidt, Self-Propelled Micromotors for Cleaning Polluted Water, *ACS Nano*, 2013, 7(11): 9611-9620.

62. Sanchez, S., A.N. Ananth, V.M. Fomin, M. Viehrig, and O.G. Schmidt, Superfast Motion of Catalytic Microjet Engines at Physiological Temperature, *Journal of the American Chemical Society*, 2011, 133(38): 14860-14863.

63. Laocharoensuk, R., J. Burdick, and J. Wang, Carbon-Nanotube-Induced Acceleration of Catalytic Nanomotors, *ACS Nano*, 2008, 2(5): 1069-1075.

64. Ke, H., S. Ye, R.L. Carroll, and K. Showalter, Motion Analysis of Self-Propelled Pt−Silica Particles in Hydrogen Peroxide Solutions, *The Journal of Physical Chemistry A*, 2010, 114(17): 5462-5467.

65. Campuzano, S., J. Orozco, D. Kagan, M. Guix, W. Gao, S. Sattayasamitsathit, J.C. Claussen, A. Merkoçi, and J. Wang, Bacterial Isolation by Lectin-Modified Microengines, *Nano Letters*, 2011, 12(1): 396-401.

66. Ginoza, T., K. Okamura, J. Fukuda, and H. Suzuki. *Improvement of detection sensitivity using electrodes with micropillar structures*. in *Solid-State Sensors, Actuators and Microsystems Conference 2009 TRANSDUCERS*. 2009.

67. Guo, M.-m., Y. Xia, W. Huang, and Z. Li, Electrochemical fabrication of stalactite-like copper micropillar arrays via surface rebuilding for ultrasensitive nonenzymatic sensing of glucose, *Electrochimica Acta*, 2015, 151(0): 340-346.

68. Gao, C., Z. Guo, J.-H. Liu, and X.-J. Huang, The new age of carbon nanotubes: An updated review of functionalized carbon nanotubes in electrochemical sensors, *Nanoscale*, 2012, 4(6): 1948-1963.

69. Chikkaveeraiah, B.V., H. Liu, V. Mani, F. Papadimitrakopoulos, and J.F. Rusling, A microfluidic electrochemical device for high sensitivity biosensing: Detection of nanomolar hydrogen peroxide, *Electrochemistry Communications*, 2009, 11(4): 819-822.

70. Escarpa, A., M.C. González, M.A. López, A. Escarpa, M.C. González, and M.Á. López, *Electrochemical Sensing on Microfluidic Chips*, in *Agricultural and Food Electroanalysis*. 2015, John Wiley & Sons, Ltd. p. 331-356.

71. Claussen, J.C. and I.L. Medintz, Using Nanotechnology to Improve Lab on a Chip Devices, *Journal of Biochips & Tissue Chips*, 2012, 2(4): e117.

72. Nyholm, L., Electrochemical techniques for lab-on-a-chip applications, *Analyst*, 2005, 130(5): 599-605.

73. Chen, B., N.T. Garland, J. Geder, M. Pruessner, E. Mootz, A. Cargill, A. Leners, G. Vokshi, J. Davis, W. Burns, M.A. Daniele, J. Kogot, I.L. Medintz, and J.C. Claussen, Platinum Nanoparticle Decorated SiO2 Microfibers as Catalysts for Micro Unmanned Underwater Vehicle Propulsion, *ACS Applied Materials & Interfaces*, 2016, 8(45): 30941-30947.

74. Claussen, J.C., M.A. Daniele, J. Geder, M. Pruessner, A.J. Makinen, B.J. Melde, M. Twigg, J.M. Verbarg, and I.L. Medintz, Platinum-Paper Micromotors: An Urchin-Like Nanohybrid Catalyst for Green Monopropellant Bubble-Thrusters, *ACS Applied Materials & Interfaces*, 2014, 6(20): 17837-17847.

75. Qiang, L., S. Vaddiraju, J.F. Rusling, and F. Papadimitrakopoulos, Highly sensitive and reusable Pt-black microfluidic electrodes for long-term electrochemical sensing, *Biosensors and Bioelectronics*, 2010, 26(2): 682-688.

76. Sassa, F., H. Laghzali, J. Fukuda, and H. Suzuki, Coulometric Detection of Components in Liquid Plugs by Microfabricated Flow Channel and Electrode Structures, *Analytical Chemistry*, 2010, 82(20): 8725-8732.

77. Guascito, M.R., D. Chirizzi, C. Malitesta, E. Mazzotta, M.Siciliano, T. Siciliano, A. Tepore, and A. Turco, Low-potential sensitive H2O2 detection based on composite micro tubular Te adsorbed on platinum electrode, *Biosensors and Bioelectronics*, 2011, 26(8): 3562-3569.

78. Niu, X., H. Zhao, C. Chen, and M. Lan, Platinum nanoparticle-decorated carbon nanotube clusters on screen-printed gold nanofilm electrode for enhanced electrocatalytic reduction of hydrogen peroxide, *Electrochimica Acta*, 2012, 65: 97-103.

79. Chen, K.-J., C.-F. Lee, J. Rick, S.-H. Wang, C.-C. Liu, and B.-J. Hwang, Fabrication and application of amperometric glucose biosensor based on a novel PtPd bimetallic nanoparticle decorated multi-walled carbon nanotube catalyst, *Biosensors and Bioelectronics*, 2012, 33(1): 75-81.

80. Fang, Y., D. Zhang, X. Qin, Z. Miao, S. Takahashi, J.-i. Anzai, and Q. Chen, A non-enzymatic hydrogen peroxide sensor based on poly(vinyl alcohol)–multiwalled carbon nanotubes–platinum nanoparticles hybrids modified glassy carbon electrode, *Electrochimica Acta*, 2012, 70: 266-271.

81. Han, L., Q. Wang, S. Tricard, J. Liu, J. Fang, J. Zhao, and W. Shen, Amperometric detection of hydrogen peroxide utilizing synergistic action of cobalt hexacyanoferrate and carbon nanotubes chemically modified with platinum nanoparticles, *RSC Advances*, 2013, 3(1): 281-287.

82. Miao, Z., D. Zhang, and Q. Chen, Non-enzymatic Hydrogen Peroxide Sensors Based on Multi-wall Carbon Nanotube/Pt Nanoparticle Nanohybrids, *Materials*, 2014, 7(4): 2945.

83. Li, X., X. Liu, W. Wang, L. Li, and X. Lu, High loading Pt nanoparticles on functionalization of carbon nanotubes for fabricating nonenzyme hydrogen peroxide sensor, *Biosensors and Bioelectronics*, 2014, 59(0): 221-226.

84. Heli, H., N. Sattarahmady, R. Dehdari Vais, and A.R. Mehdizadeh, Enhanced electrocatalytic reduction and highly sensitive nonenzymatic detection of hydrogen peroxide using platinum hierarchical nanoflowers, *Sensors and Actuators B: Chemical*, 2014, 192: 310-316.

85. Sun, Y., K. He, Z. Zhang, A. Zhou, and H. Duan, Real-time electrochemical detection of hydrogen peroxide secretion in live cells by Pt nanoparticles decorated graphene–carbon nanotube hybrid paper electrode, *Biosensors and Bioelectronics*, 2015, 68: 358-364.

86. Mei, H., W. Wu, B. Yu, H. Wu, S. Wang, and Q. Xia, Nonenzymatic electrochemical sensor based on Fe@Pt core–shell nanoparticles for hydrogen peroxide, glucose and formaldehyde, *Sensors and Actuators B: Chemical*, 2016, 223: 68-75.

87. Atci, E., J.T. Babauta, and H. Beyenal, A hydrogen peroxide microelectrode to use in bioelectrochemical systems, *Sensors and Actuators B: Chemical*, 2016, 226: 429-435.

88. Brownlee, B.J., M. Bahari, J.N. Harb, J.C. Claussen, and B.D. Iverson, Electrochemical Glucose Sensors Enhanced by Methyl Viologen and Vertically Aligned Carbon Nanotube Channels, *ACS Applied Materials & Interfaces*, 2018, 10(34): 28351-28360.

89. Ahmad, R., M.-S. Ahn, and Y.-B. Hahn, A Highly Sensitive Nonenzymatic Sensor Based on Fe2O3 Nanoparticle Coated ZnO Nanorods for Electrochemical Detection of Nitrite, *Advanced Materials Interfaces*, 2017, 4(22): 1700691.

90. Dashty, M., A Quick Look at Biochemistry: Carbohydrate Metabolism, *Clinical Biochemistry*, 2013, 46(15): 1339-1352.

91. Domingueti, C.P., L.M.S.A. Dusse, M.d.G. Carvalho, L.P. de Sousa, K.B. Gomes, and A.P. Fernandes, Diabetes Mellitus: The Linkage Between Oxidative Stress, Inflammation, Hypercoagulability and Vascular Complications, *Journal of Diabetes and Its Complications*, 2016, 30(4): 738-745.

92. Zhao, C.-e., P. Gai, R. Song, Y. Chen, J. Zhang, and J.-J. Zhu, Nanostructured Material-Based Biofuel Cells: Recent Advances and Future Prospects, *Chemical Society Reviews*, 2017, 46(5): 1545-1564.

93. Gamella, M., A. Koushanpour, and E. Katz, Biofuel Cells – Activation of Micro- and Macro-Electronic Devices, *Bioelectrochemistry*, 2018, 119: 33-42.

94. Cosnier, S., A. J. Gross, A. Le Goff, and M. Holzinger, Recent Advances on Enzymatic Glucose/Oxygen and Hydrogen/Oxygen Biofuel Cells: Achievements and Limitations, *Journal of Power Sources*, 2016, 325: 252-263.

95. Abreu, C., Y. Nedellec, A.J. Gross, O. Ondel, F. Buret, A.L. Goff, M. Holzinger, and S. Cosnier, Assembly and Stacking of Flow-through Enzymatic Bioelectrodes for High Power Glucose Fuel Cells, *ACS Applied Materials & Interfaces*, 2017, 9(28): 23836-23842.

96. Mross, S., S. Pierrat, T. Zimmermann, and M. Kraft, Microfluidic Enzymatic Biosensing Systems: A Review, *Biosensors and Bioelectronics*, 2015, 70: 376-391.

97. Zhu, H., L. Li, W. Zhou, Z. Shao, and X. Chen, Advances in Non-enzymatic Glucose Sensors Based on Metal Oxides, *Journal of Materials Chemistry B*, 2016, 4(46): 7333-7349.

98. Zen, J.-M. and C.-W. Lo, A Glucose Sensor Made of an Enzymatic Clay-Modified Electrode and Methyl Viologen Mediator, *Analytical Chemistry*, 1996, 68(15): 2635-2640.

99. Ghica, M.E. and C.M.A. Brett, A Glucose Biosensor Using Methyl Viologen Redox Mediator on Carbon Film Electrodes, *Analytica Chimica Acta*, 2005, 532(2): 145-151.

100. Wang, X., S.B. Kim, D. Khang, H.-H. Kim, and C.-J. Kim, Optimization and Characterization of Covalent Immobilization of Glucose Oxidase for Bioelectronic Devices, *Biochemical Engineering Journal*, 2016, 112: 20-31.

101. Bockris, J.O.M. and L.F. Oldfield, The Oxidation-Reduction Reactions of Hydrogen Peroxide at Inert Metal Electrodes and Mercury Cathodes, *Transactions of the Faraday Society*, 1955, 51(0): 249-259.

102. Anderson, L., S.M. Wittkopp, C.J. Painter, J.J. Liegel, R. Schreiner, J.A. Bell, and B.Z. Shakhashiri, What Is Happening When the Blue Bottle Bleaches: An Investigation of the Methylene Blue-Catalyzed Air Oxidation of Glucose, *Journal of Chemical Education*, 2012, 89(11): 1425-1431.

103. De Wit, G., A.P.G. Kieboom, and H. van Bekkum, Enolisation and Isomerisation of Monosaccharides in Aqueous, Alkaline Solution, *Carbohydrate Research*, 1979, 74(1): 157-175.

104. Monk, P.M.S., *The Viologens: Physicochemical Properties, Synthesis and Applications of the Salts of 4,4'-Bipyridine*. 1998, Chichester, New York: Wiley.

105. Ding, S., S.R. Das, B.J. Brownlee, K. Parate, T.M. Davis, L.R. Stromberg, E.K.L. Chan, J. Katz, B.D. Iverson, and J.C. Claussen, CIP2A Immunosensor Comprised of Vertically-aligned Carbon Nanotube Interdigitated Electrodes Towards Point-of-Care Oral Cancer Screening, *Biosensors and Bioelectronics*, 2018, 117: 68-74.

106. Sun, S., D. Yang, G. Zhang, E. Sacher, and J.-P. Dodelet, Synthesis and Characterization of Platinum Nanowire–Carbon Nanotube Heterostructures, *Chemistry of Materials*, 2007, 19(26): 6376-6378.

107. Gonzalez-Gaitan, C., R. Ruiz-Rosas, E. Morallon, and D. Cazorla-Amoros, Effects of the Surface Chemistry and Structure of Carbon Nanotubes on the Coating of Glucose Oxidase and Electrochemical Biosensors Performance, *RSC Advances*, 2017, 7(43): 26867-26878.

108. Chen, C., Q. Xie, D. Yang, H. Xiao, Y. Fu, Y. Tan, and S. Yao, Recent Advances in Electrochemical Glucose Biosensors: A Review, *RSC Advances*, 2013, 3(14): 4473-4491.

109. Andoy, N.M., M.S. Filipiak, D. Vetter, Ó. Gutiérrez-Sanz, and A. Tarasov, Graphene-Based Electronic Immunosensor with Femtomolar Detection Limit in Whole Serum, *Advanced Materials Technologies*, 2018, 3(12): 1800186.

110. Lequin, R.M., Enzyme Immunoassay (EIA)/Enzyme-Linked Immunosorbent Assay (ELISA), *Clinical Chemistry*, 2005, 51(12): 2415-2418.

111. Chikkaveeraiah, B.V., A.A. Bhirde, N.Y. Morgan, H.S. Eden, and X. Chen, Electrochemical Immunosensors for Detection of Cancer Protein Biomarkers, *ACS Nano*, 2012, 6(8): 6546-6561.

112. Rivadeneyra, A., J. Fernández-Salmerón, J. Banqueri, J.A. López-Villanueva, L.F. Capitan-Vallvey, and A.J. Palma, A novel electrode structure compared with interdigitated electrodes as capacitive sensor, *Sensors and Actuators B: Chemical*, 2014, 204(Supplement C): 552-560.

113. Sun, J., M. Zheng, Y. Luo, and Z. Yu, Three-dimensional detached serpentine flow field design for redox flow batteries, *Journal of Power Sources*, 2019, 428: 136-145.

114. Sugime, H., T. Ushiyama, K. Nishimura, Y. Ohno, and S. Noda, An interdigitated electrode with dense carbon nanotube forests on conductive supports for electrochemical biosensors, *Analyst*, 2018, 143(15): 3635-3642.

115. Diamandis, E.P. and T.K. Christopoulos, The biotin-(strept)avidin system: principles and applications in biotechnology, *Clinical Chemistry*, 1991, 37(5): 625-636.

116. Koehne, J., J. Li, A.M. Cassell, H. Chen, Q. Ye, H.T. Ng, J. Han, and M. Meyyappan, The fabrication and electrochemical characterization of carbon nanotube nanoelectrode arrays, *Journal of Materials Chemistry*, 2004, 14(4): 676-684.

117. Kang, X., Z. Mai, X. Zou, P. Cai, and J. Mo, A sensitive nonenzymatic glucose sensor in alkaline media with a copper nanocluster/multiwall carbon nanotube-modified glassy carbon electrode, *Analytical Biochemistry*, 2007, 363(1): 143-150.

118. Elgrishi, N., K.J. Rountree, B.D. McCarthy, E.S. Rountree, T.T. Eisenhar, and J.L. Dempsey, A Practical Beginner's Guide to Cyclic Voltammetry, *Journal of Chemical Education*, 2018, 95(2): 197-206.

119. Lai, C.-Y., J.-H. Weng, W.-L. Shih, L.-C. Chen, C.-F. Chou, and P.-K. Wei, Diffusion impedance modeling for interdigitated array electrodes by conformal mapping and cylindrical finite length approximation, *Electrochimica Acta*, 2019, 320: 134629.

120. Choi, W., H.-C. Shin, J.M. Kim, J.-Y. Choi, and W.-S. Yoon, Modeling and Applications of Electrochemical Impedance Spectroscopy (EIS) for Lithium-ion Batteries, *Journal of Electrochemical Science and Technology*, 2020, 11(1): 1-13.

121. Erickson, H.P., Size and Shape of Protein Molecules at the Nanometer Level Determined by Sedimentation, Gel Filtration, and Electron Microscopy, *Biological Procedures Online*, 2009, 11(1): 32.

122. Manczak, R., M. Fouet, R. Courson, P.-L. Fabre, A. Montrose, J. Sudor, A.-M. Gué, and K. Reybier, Improved on-chip impedimetric immuno-detection of subpopulations of cells toward single-cell resolution, *Sensors and Actuators B: Chemical*, 2016, 230: 825-831.

123. Lee, S.-J., V. Anandan, and G. Zhang, Electrochemical fabrication and evaluation of highly sensitive nanorod-modified electrodes for a biotin/avidin system, *Biosensors and Bioelectronics*, 2008, 23(7): 1117-1124.

124. Buzid, A., P.E. Hayes, J.D. Glennon, and J.H.T. Luong, Captavidin as a regenerable biorecognition element on boron-doped diamond for biotin sensing, *Analytica Chimica Acta*, 2019, 1059: 42-48.

APPENDIX A.   STANDARD PROCESSES AND EQUIPMENT PROCEDURES

A.1   Fabrication of VACNT Sensors

1. Start with 4" oxidized Si wafer
2. If necessary, spin solvent clean and dehydrate bake wafer at 150 $^{\circ}$C for 8 min
3. If using underlying chromium pattern (for IDE mask):
   a. Spin coat with HMDS
   b. Spin coat with AZ 3330
   c. Soft bake wafer on hot plate for 60 sec at 90 $^{\circ}$C
   d. Allow wafer to cool on table (about 15 seconds)
   e. Expose photoresist with mask for 12-20 seconds (IDE with contact pads)
   f. Hard bake wafer on hot plate for 60 sec at 90 $^{\circ}$C
   g. Allow wafer to cool on table (about 15 seconds)
   h. Develop photoresist
   i. Deposit 75 nm chromium with e-beam
   j. Sonicate wafer for 30 min in N-Methyl-2-pyrrolidone (NMP) and rinse with water
   k. Dry with clean air or nitrogen gun
   l. Using a sharpie, manually mark over chromium contact pads
4. Deposit $Al_2O_3 \sim$ 150 nm thick using the e-beam evaporator
   a. If using chromium, after deposition sonicate wafer for 5 min in NMP and rinse with water.
5. Spin coat with HMDS (*don't use if already have chromium layer)
6. Spin coat with AZ 3330 (AZ 2020 if negative mask, currently only small circles mask)
   a. If AZ 3330 is not available, AZ 3312 may be used: see BYU cleanroom website for operating parameters.
7. Soft bake wafer on hot plate for 60 sec at 90 $^{\circ}$C (110 $^{\circ}$C if negative)
8. Allow wafer to cool on table (about 15 seconds)
9. Expose photoresist with mask for 12-20 seconds (8 seconds if negative)
   a. If using chromium layer, be sure to align finger-only mask to original chromium layer
10. Hard bake wafer on hot plate for 60 sec at 90 $^{\circ}$C (110 $^{\circ}$C if negative)
11. Allow wafer to cool on table (about 15 seconds)
12. Develop photoresist
13. Evaporate Fe $\sim$ 7 nm with thermal evaporator (JIM)
14. Sonicate wafer for 30 min in N-Methyl-2-pyrrolidone (NMP) and rinse with water
15. Dry with clean air or nitrogen gun
16. Spin coat with AZ 3330

17. Soft bake wafer on hot plate for 60 sec at 90 ⁰C
18. Dice wafer
19. Grow CNTs
20. O$_2$ etch samples with PEII
21. If applicable, deposit Pt
    a. After, soak in DI water for 5 min and then dry on hotplate at 100 ⁰C for 3 min
22. If applicable, biofunctionalize the CNTs

A.2   Wafer Solvent Clean

1. Ensure that the motor speed on Solitec spinner is set to 0 rpm, and that the vacuum and motor switches are both turned off before beginning cleaning process
2. Turn main power for the Solitec spinner on
3. Slide wafer-positioning fixture around chuck collar
4. Place wafer onto chuck face, using fixture as alignment guide
5. While fixture (and wafer) are being pressed against bottom face of chuck collar, turn vacuum switch on
6. Lower fixture until wafer adheres to chuck face
7. Carefully slide fixture away from chuck
8. Turn motor switch on and slowly increase rotational speed to ~3,000 rpm
9. Spray continuous stream of Acetone onto center of wafer for several seconds
10. Begin to spray Isopropyl Alcohol (IPA) onto center of wafer concurrently with Acetone
11. After 1-2 seconds, discontinue Acetone stream and allow for 2-3 more seconds of IPA dispensing to continue (this ensures that no residual Acetone is left on wafer)
12. Once IPA dispensing is discontinued, allow a few seconds for the IPA to spin off of wafer (this is indicated by an outward spiral color change on wafer surface)
13. Repeat steps 9-12 three times per wafer
14. Slowly decrease spinner speed until chuck (wafer) is no longer rotating
15. Turn motor switch off
16. Turn vacuum switch off
17. Turn main power off
18. Carefully remove wafer from chuck face

A.3   Film Deposition using Denton Vacuum Integrity 20 E-Beam Evaporator

1. If chamber is initially under vacuum, ensure that all functions/valves are off and select Vent button
2. Once chamber is vented, the chamber door should open easily allowing for placement of wafers (this may take several minutes after gage reads atmospheric pressure)
3. Inspect wafer planetary system and ensure that motor fixtures are installed
4. Secure wafers to wafer plates by gently tightening the nuts to the screws around perimeter of wafer
5. If wafer got particulates on it, use clean air or nitrogen gun to gently blow off each wafer assembly before installation onto planetary system in E-Beam Evaporator chamber
6. Use set screw on backside of wafer plate to mount securely to motor fixtures

7. Gently pull on each wafer plate after installation to ensure that plates are securely fastened
8. Secure wires from each battery on motor fixtures to accompanying electric motor to begin rotation of wafer plates
9. Ensure E-Gun Shutter is open (green) so as to allow access to the crucible receiver
10. Acquire crucible of desired material
    a. Tungsten does not have a sleeve/material holder, it is place directly into e-beam in two layers, with previously used pellets on top layer
11. Place crucible into receiver of E-Beam Evaporator
12. Use a flashlight to illuminate crucible within chamber
    a. Flashlight should be placed such that it does not need to be held in place
13. Align E-Beam Evaporator mirrors such that the crucible can only be seen through the sightglass by reflection off mirrors, and not by direct line of sight
    a. Note: If crucible can be seen by direct line of sight, deposition will occur on sightglass
14. Turn off, and remove, flashlight from E-Beam Evaporator chamber
15. On E-Beam Evaporator display, select Rotation to begin rotation of planetary system
    a. Note: Speed button can also be used to adjust rotational speed of planetary system
16. Select E-Gun Shutter button (turn off; red) to ensure that deposition will not begin prematurely during ramp up
17. Shut chamber door and press firmly on door until vacuum is pulled in chamber during following steps
18. Select Mech Pump button (turn on; green)
19. Select Roughing Valve button (turn on; green)
20. Start timer for roughing pump
21. Wait 6 minutes
22. Select Roughing Valve button (turn off; red)
23. Select High Vac Valve "bomb" then press square at end of sentence (turn on; green)
24. Start timer for high vacuum
25. Wait 30 seconds
26. Select Ion Gauge Emission (turbo pump) button (turn on; green)
27. While pumping down, set the program to correct material
    a. Turn on power to Inficon XTC/2 deposition controller box
    b. Set parameters on deposition controller box according to material
        i. Select Reset
        ii. Select Stop
        iii. Change parameters by selecting Program (navigate using arrow keys; be sure to select either the up or down arrows after a value is entered in order to store the value)
            1. Tooling factor 1 and 2 (Current: Al_2O_3 = 180, W = 120, Cr = 140)
            2. Density (Al_2O_3 = 3.97, W = 19.25, Cr = 7.20)
            3. Z-Ratio (Al_2O_3 = 0.336, W = 0.163, Cr = 0.305)
        iv. Select Program to return to main screen
    c. Select Life to display crystal life (XTAL%)
    d. Record crystal life in logbook

28. Wait until Chamber IG display indicates a chamber pressure of 5.5×10^{-5} Torr or lower and record time in logbook
29. Perform deposition
    a. Turn on main power to Power Supply (when at 5.5×10^{-5} Torr)
    b. Turn on power for pattern sweep controller (Kangaroo)
    c. Turn on Voltage (left green button)
    d. Turn on Emission (right green button)
    e. Slowly ramp up Emission Current Adjustment knob, allowing for about 4 seconds between each value of 10 on dial
    f. Once a visual of the crucible can be seen through sightglass, adjust current pattern as desired. Note: very tight sweep mode must be used for tungsten.
        i. Pattern 1 covers a large area of the crucible, good for chromium
        ii. Pattern 2 covers a moderate area of crucible, good for alumina
        iii. To move pattern, press the cross-hair button on the controller and then use the sweep joystick, ensuring that current pattern is located exclusively within the material to be deposited. Note: the beam may need to be moved slightly if the deposition rate drops during run.
    g. With the shutter closed, continue slowly ramping up Emission Current Adjustment knob until desired current is achieved. Note that the deposition rate will not be seen until the shutter is open.
        i. Al_2O_3 deposits around 2-3 Å/s at 55 mA
        ii. Chromium deposits around 3-4 Å/s at 25-30 mA
        iii. Tungsten deposits at about 300 mA, resulting in about 0.3 Å/s.
    h. Select E-Gun Shutter button (turn on; green) to open shutter
    i. Select Start button on deposition controller box to begin deposition measurements
    j. Continue deposition until desired thickness is met (read in KÅ)
        i. If the deposition rate drops during deposition, the location of the electron beam may need to be moved slightly
    k. Select E-Gun Shutter button (turn off; red)
    l. Begin slowly ramping down current using Emission Current Adjustment knob
    m. Record deposition thickness on E-Beam Evaporator logbook along with operating pressure, etc
    n. Once current reads 0.0 mA (off), turn off Emission (right side)
    o. Turn off Voltage (left side)
    p. Turn off power supply, pattern controller, and deposition controller box
30. Wait 5-10 minutes for the system to cool
31. Select Ion Gauge Emission button (turn off; red)
32. Select High Vac Valve "bomb" (turn off; red)
33. Select Mech Pump button (turn off; red)
34. Select Vent to vent chamber
35. Select E-Gun Shutter button (turn on; green)
36. Remove crucible using large tweezers (this may still be hot)
37. Remove wafer plates and wafers
38. Shut chamber door and press firmly on door until vacuum is pulled in chamber during following steps
39. Put E-Beam Evaporator in standby mode

  a. Select Mech Pump button (turn on; green)
  b. Select Roughing Valve button (turn on; green)
  c. Wait 6 minutes
  d. Select Roughing Valve button (turn off; red)
  e. Select Mech Pump button (turn off; red)
40. Finish filling out E-Beam Evaporator logbook

A.4 Hexamethyldisilazane (HMDS) Spin Coating

1. Place and center wafer on Laurell WS-400-6NPP Spin Coater chuck
2. Select Vacuum button to turn on vacuum
3. Select Program button to cycle through preset spin settings (adjust as needed)
  a. Program D
    i. Speed: 3000 rpm
    ii. Acceleration: 550 rad/s^2
    iii. Time: 10 sec
4. Blow surface clean with clean air or nitrogen gun
5. Dispense about 3-4 drops of HMDS onto center of wafer surface
6. Immediately close spin coater lid and select Run/Stop button
7. Close HMDS bottle
8. Open spin coater lid and inspect wafer once spin coating is complete
  a. If coating is not satisfactory, solvent clean wafer and bake in oven at 150 ⁰C for 8-10 min
  b. Repeat HMDS spin coating process
9. If not proceeding to photoresist spin coating, remove the wafer from the spinner
  a. Select Vacuum button to release wafer
  b. Remove wafer and place in storage case
  c. Use Acetone to remove excess photoresist from inside of spin coater

A.5 AZ 3330 (or AZ 2020) Spin Coating

1. Place and center wafer on Laurell WS-400-6NPP Spin Coater chuck
2. Select Vacuum button to turn on vacuum
3. Select Program button to cycle through preset spin settings (adjust as needed)
  a. AZ 3330 (Positive photoresist, including IDE and serpentine patterns)
    i. Speed: 5000-6000 rpm (usually 5000 rpm)
    ii. Acceleration: 5000-6000 rad/s^2
    iii. Time: 60 sec
  b. AZ 2020 (Negative photoresist, mainly just for small circles pattern)
    i. Speed: 2750 rpm
    ii. Acceleration: 2750 rad/s^2
    iii. Time: 60 sec
4. Spray surface clean with clean air or nitrogen gun
5. Dispense about ~40 drops of photoresist onto center of wafer surface

6. Immediately close spin coater lid and select Run/Stop button
7. Close photoresist bottle
8. Open spin coater lid and inspect wafer once spin coating is complete
   a. If coating is not satisfactory, solvent clean wafer and bake in oven at 150 °C for 8-10 min
   b. Repeat photoresist spin coating process
9. Select Vacuum button to release wafer
10. Remove wafer and place in storage case
11. Use Acetone to remove excess photoresist from inside of spin coater

A.6   Photoresist Exposure with 4" MA 150 CC Karl Suss Mask Aligner/Bonder

1. Good to ensure that aligner is powered on, gas valves are open, and desired channel wavelengths are available
   a. Channel 1: 365 nm (for negative photoresist)
   b. Channel 2: 405 nm (for positive photoresist)
   c. Note: If aligner is not powered on, follow Operating Instructions given on the cleanroom website (http://www.cleanroom.byu.edu/ma150.phtml)
2. If necessary, verify the lamp intensity
   a. Locate desired sensor in box and connect to output meter
      i. Positive photoresist: 405 nm sensor
      ii. Negative photoresist: 365 nm sensor
   b. Exit the Short Program
   c. Place sensor (on stand) in the center of the wafer chuck (chuck should be down)
   d. Select System
      i. Select Light Measure
      ii. Return (when done measuring)
   e. When new the output is 16-18 mW/cm
   f. Longer exposure times will be needed if below 13 mW/cm
      i. Note that at around 11 mW/cm an exposure of 20 seconds is needed for AZ 3330.
3. Set exposure parameters on aligner
   a. If load wafer screen is shown, select Cancel
   b. Select Change Program button
   c. Select Edit button
   d. Select Change Type
   e. If First Mask, select Hard Contact. If using Manual Align, select Soft Contact.
   f. Select Page 1 button
      i. Max Exposures (not relevant)
      ii. Set Exposure Time (12-20 sec for AZ 3330 [12 sec for new lamp, 20 sec for lamp intensity of 11 mW/cm] or 8 sec for AZ 2020)
      iii. Set Alignment Gap (50 μm)
      iv. Set Hard/Soft Contact Time (10 sec)
   g. Select Return button
   h. Select Page 2 button

        i.   Set Resist (Positive)
       ii.   Set Mode (First Mask for first exposure on mask or Manual Align if aligning mask to chromium features on wafer)
     iii.   Set WEC (Contact)
     iv.   Set Alignment Check (Off)
      v.   Set Prealigner Type (0)

    i. Select Return button
    j. Select Continue button
    k. Select Return button twice

4. Select Start button
5. Vacuum will release on mask panel, allowing for removal of mask if one is present
6. Select Continue button (wafer chuck will rise)
7. Place wafer onto chuck, ensuring that the flattened edge of the wafer is aligned with patterned edge on chuck
8. Use fingers around outer perimeter of chuck to center wafer
9. Select Vacuum: Off button (should now read Vacuum: On)
10. Select Continue button
11. Chuck will lower and panel will unclamp
12. Gently slide panel away from aligner about halfway along track (a 'click' should be heard, indicating the max recommended draw for the panel)
    a. Warning: Pulling panel any farther will cause panel to fall off of track
13. Gently place mask, chrome side down (dark, not shiny side), onto panel using alignment pins for centering. For alignment purposes, have the dicing lines on IDE masks closest to you and to the right.
    a. Note: a light solvent clean is recommended for mask prior to exposures
        i. Lightly rinse both sides of mask with Acetone, followed by IPA, and dry with clean air or nitrogen gun
14. Select Vacuum: Off button (should now read Vacuum: On)
15. Once vacuum is pulled on mask, gently apply pressure to mask with fingers to ensure that mask is securely held to panel
16. Firmly slide panel back into aligner until seated
17. Select Clamping: Off button (should now read Clamping: On)
18. Select Continue button
19. If doing a First Mask exposure, chuck will rise and press wafer against mask followed by exposure.
20. If doing a Manual Align exposure, the microscope will move into position
    a. The joysticks are used to control the movement of the microscope and the mask.
    b. Press the buttons on the left joystick to switch between moving just the microscope or moving both the microscope and the mask (both lit)
    c. The left joystick rotates the microscope/mask while the right joystick moves in the plane of the mask
        i. If the aligner freezes, press Ctrl + Alt + Delete on the keyboard under the machine (near your knees). The username to enter the system is "student".
    d. Move the microscope (Microscope button only) until one of the screens is focused on the outermost IDE pattern.

    e.   Twist the silver knob of the opposite microscope until it is over top the opposite outermost IDE pattern. Note that you may need to adjust the rotation of the microscope such that both IDEs can be seen by both microscopes.

    f.   After the microscope is positioned well, now move and rotate the mask (both microscope and mask lights lit) until the fingers are all aligned

    g.   Check alignment on top and bottom of IDE pattern.

    h.   Once aligned, turn off all the lights on the joysticks

        i.   The mask will come into contact with the wafer and you can check alignement.

    i.   Press the Exposure button near the right joystick (now lit up green)

        i.   It may ask to check the exposure, and press expose again if still looks good.

21. After exposure, chuck will lower and clamping will turn off
22. Gently slide panel away from aligner about halfway along track
23. Select Vacuum: On button (should now read Vacuum: Off) and remove mask
24. Gently place mask back in storage container
25. Firmly slide panel back into aligner until seated
26. Select Clamping: Off button (should now read Clamping: On)
27. Select Continue button
28. Chuck will rise and vacuum will turn off
29. Gently remove wafer and place in storage container, ensuring that wafer is not exposed to ultraviolet (UV) light until after subsequent bake and development processes
30. Once wafer is removed, select Cancel
31. Chuck will lower (aligner display will return to main screen)

A.7   Photoresist Development

1. If not already in cabinet, pour AZ developer (300 MIF) into crystallizing dish
2. Place wafer in the dish
3. Agitate developer gently for about 15-20 seconds. If taking longer than this, exposure times may need to be longer when using the aligner.
4. Monitor the progress of the development
5. Using wafer tweezers, remove wafer and hold under a gentle stream of deionized (DI) water in sink for several seconds and both sides of wafer
6. Place wafer onto cleanroom paper towel
7. Gently blow off water, beginning at center of wafer and moving radially outward, using clean air or nitrogen gun
8. Inspect wafer under optical microscope to ensure development completion
9. Repeat steps 3-9 with short development times if the development is incomplete
    a.   Note: If development becomes ruined, use aluminum wet etch as prescribed on cleanroom website (http://www.cleanroom.byu.edu/wet_etch.phtml)
10. Place wafer in storage container
11. Return 300 MIF to group cabinet or dispose of 300 MIF in labeled 300 MIF waste container using funnel if it has been used for several wafers (becoming dark).

A.8   Iron Deposition using Thermal Evaporator

1. Vent the chamber and raise the bell jar.
    a. The system should be in standby. Ensure the ion gauge is off and both the gate valve and roughing valve are closed.
    b. Open nitrogen tank with the regulator set to 20 psi.
    c. Open the vent valve to pressurize the chamber to 760 Torr. When the chamber is pressurized, the rubber seal should break, as can be verified by pushing against outside of the bell jar. Close the vent valve and nitrogen tank.
    d. Raise the bell jar by pressing the raise button.
2. Prepare sample and source material.
    a. Use Kapton tape to secure wafer on the target plate above the closed shutter.
    b. Secure iron evaporator boat between electrodes.
        i. Use lab's iron boat. If a new boat is needed, place one iron pellet in good contact with side of boat and perform run, turning power close to maximum until the iron melts and evaporation rate jumps significantly. Two iron pellets could also be used.
    c. Replace glass slide window if you can't see through it
3. Check the crystal monitor and set material properties on the INFICON deposition monitor.
    a. Turn on the monitor and press the "XTAL" button. If XTAL reading is 100%, replace the crystal.
    b. Press the PROG button to material properties. Set to Film 2 for iron by pressing the number 2 when film is selected. Ensure the density, z-ratio, and tooling factor are correct for iron:
        i. Density = 7.86
        ii. Z-Ratio = 0.349
        iii. Current tooling factor = 103.5%
    c. Press PROG to save changes.
4. Pump down the chamber.
    a. Lower the bell jar with the sealing surface centered.
    b. Make sure the vent valve is closed. Slowly open the roughing valve, keeping the foreline pressure (TC2) below 3×10^2 Torr.
    c. When the chamber pressure (TC1) reads 0.5×10^{-1} Torr, close the roughing pump valve. This should take around 6 minutes, record time in logbook.
    d. Open the gate valve.
    e. Turn on the ion gauge after 30 seconds by pressing the "EMIS" button on the VARIAN SenTorr.
        i. The filament should light up, and a pressure reading will be given on the SenTorr next to the IG label.
    f. Let the cryo pump reduce pressure to 1×10^{-5} Torr or less and record time in logbook.
5. Deposition.

a. Toggle the "FILAMENT" switch on the control panel to turn on the current supply.
b. Slowly ramp up the current supply with the VARIAC knob.
  i. To prevent thermal hardening of the boat, do not exceed a ramp speed of 20 V/min.
  ii. The current supply should never exceed 10 amps.
c. Increase the current until the deposition rate on the monitor reads about 0.5 angstroms/s (usually about 150 V or more).
d. Simultaneously open the shutter and press ZERO on the deposition monitor to reset and record sample thickness.
e. Close the shutter when the monitor reaches the desired thickness (7 nm or 70 angstroms (0.07 kAngstrom)).
f. Ramp down the current no faster than 30 V/min until at 0 V.
g. Close the gate valve
h. Wait at least 10 minutes for the system to cool before venting the chamber.

6. Vent chamber and remove samples.
a. Turn off ion gauge.
b. Open nitrogen tank and vent valve, as before.
c. When the rubber seal breaks at 760 Torr, close vent valve and nitrogen tank.
d. Raise the bell jar and remove your samples.

7. System standby.
a. Lower the bell jar with the seal centered.
b. Slowly open the roughing valve, being sure not to exceed 3×10^2 Torr for the foreline pressure.
c. Allow the pressure to reach 5×10^{-1} Torr. Close the roughing valve.

A.9   Dice Samples using Disco DAD-320 Dicing Saw

1. Time can be saved if the dicing saw is prepared while the wafer is sonicating in NMP after iron deposition
2. Ensure that the Disco DAD-320 Dicing Saw is turned on (should not be turned off)
3. Ensure that air and water supply to dicing saw are turned on (should not be turned off)
4. Turn on dicing saw monitor
  a. The Main Menu should be displayed. If not, select Exit until it appears.
5. Lift up on saw blade shield
6. Remove protector around blade holder by twisting screw
7. Use accompanying dicing saw chuck tool to loosen spindle set ring
8. Place dicing saw blade onto spindle and secure with spindle set ring using dicing saw chuck tool
9. Replace piece surrounding blade
10. Close saw blade shield
11. Using dicing saw control pad, select System Initialize (SYS INIT)
12. Once system initialization is complete, Select F5 from the main menu
13. Select F1 then F5 to change the blade type

14. Select blade from list (currently using 27HEFE) and select Enter
15. Select Setup key and confirm that the Blade Outer Diameter (2.187 in) and Chuck Table Size (6 in) are set to the correct values
16. Select Enter
    a. (Dicing saw will begin a testing procedure to validate the blade diameter value)
    b. If the machine gives an alarm, press the ALRM CLR button. Try blowing air under and around the wafer chuck and try the Setup again.
17. Once validation process is complete, select Spindle (this will stop spindle rotation)
18. Select Exit until returned to the Main Menu
19. Select F3
    a. Ensure that the Device Data Number is set to 100 and the Device ID is set to Silicon
20. Press Enter
21. The following parameters should be set:
    a. Cut mode should be A
    b. Round working shape (100 mm)
    c. Work Thickness: 0.65 mm
    d. Blade Height: 0.4 mm (this gives enough strength but allows easy breaking)
    e. Y Index (Ch1) is the first dimension to be cut.
        i. IDE dimensions are 16.1 x 8.0 mm
        ii. Circle mask dimensions are 16.93 x 16.93 mm
    f. Y Index (Ch2) is the second dimension to be cut after 90-degree rotation
22. Place wafer onto Ultron Systems, Inc. UH114 according to patterned outlined on stage
23. Place wafer ring onto stage, against alignment pegs
24. Pull adhesive sheet over wafer ring and use roller to ensure adhesion
25. Use razor blade to cut adhesive sheet away from roll
26. Gently pull up on applied adhesive sheet to free ring and wafer from stand
27. Using hands, pull up on a side of the adhesive sheet, pull tightly, and re-secure on ring
    a. Repeat this step along entire perimeter of ring such that the adhesive sheet is taut
28. Use razor blade to trim excess adhesive sheet along outer perimeter of ring
29. Place wafer onto dicing saw chuck table with sheet side down and position according to pattern on chuck
30. Select Vacuum (C/T VAC key) to secure wafer onto chuck
31. Select F7
32. Turn on the microscope light by turning the black knob above the emergency off switch.
33. Use the chuck orientation/positioning keys and optical cameras (displayed in the dicing saw monitor) to align the blade with the wafer pattern
    a. Use the Slow button to make fine adjustments
    b. Use the Index button to move cameras a preset distance (according to Index values set previously)
        i. Note: location of camera dictates cut position
34. Once aligned, enter the desired number of cuts (check this value each time)
35. With the Slow button activated, make sure the underlined movement keys (T and Y) are the last pressed keys
36. Select F5 to cut toward the rear or F10 to cut toward the front of the machine
37. Press the Cut/Water key and ensure water sprays on blade

38. Select Start/Stop to begin dicing process
    a. If cutting incorrectly, press the Start/Stop button again and the process will pause after finishing the current cut
39. After the first set of cuts is complete, press the Index button and then the theta button to turn the table 90 degrees
40. Verify the alignment after turning 90 degrees and proceed with remaining cuts
41. Once dicing process is complete, spray off wafer with accompanying air gun
42. Select Spindle to stop spindle rotation
43. Select Exit until back at the main menu
44. Press Vacuum button (C/T VAC)
45. Remove wafer and holder
46. Wafer can be carefully removed from adhesive tape in one piece and placed in carrying dish/case
47. Remove blade
48. Turn off monitor and microscope light
    a. Note: always leave machine, water, and air on
49. Record information in log sheet

A.10   Carbon Nanotube (CNT) Growth using Lindberg/Blue M Tube Furnace

1. Put on black, powder-free examination gloves
2. Pour N-Methyl-2-pyrrolidone (NMP) into solvent-resistant container, if not already in container below the fume hood
   a. Note that used NMP should be discarded in the large organic waste container in the fume hood after several uses (when the color is changing away from clear)
3. Carefully place diced samples into NMP container (with photoresist coating side up)
   a. If wafer is still in one piece, carefully fracture wafer along cut lines using the edge of the counter for stability. Multiple devices can be kept together during growth.
4. Sonicate for at least 5 min
5. After sonication, carefully remove sample with tweezers
   a. Now that the sample has no protective coating, use extra caution when transporting samples so as to not scratch the iron
6. Thoroughly rinse sample with ultrapure water and then leave a thin layer of water covering the sample
7. Blow off water using clean air (at fume hood) or nitrogen gun
8. Inspect sample for any visual flaws
9. Repeat steps 5-8 for each sonicated sample, if necessary
10. Ensure regulators on gas tanks (Hydrogen, Ethylene, Argon) are loose (turn counterclockwise)
11. Slowly open main valve on each tank
12. Slowly adjust regulator to bring outflow pressure on each tank to 20 psi
13. Under the tube furnace, set the Mass Flow Controller (MFC) to the desired flow parameters for CNT growth
    a. Ensure left switch for each gas is set to Off
    b. Using right switch for each gas, select Set
    c. Dial in desired setpoint percent (see part e)

d. Return right switch for each gas to Flow position
　　　e. Repeat steps a-d for each gas
　　　　　i. Hydrogen: 311 sccm (currently 46.9%)
　　　　　ii. Ethylene: 338 sccm (currently 37.7%)
　　　　　iii. Argon: Does not need adjusting (Typically 18.0%)
14. Unlatch and open furnace lid (to deactivate the heating element)
15. Turn on the furnace
16. Ensure that furnace has cooled sufficiently since last growth (below 250 °C)
17. Turn off air MFC (which should always be flowing when the furnace is not in use)
18. Remove the endcap (by the wing nut) and attached tubing and clean with acetone and IPA in the fume hood and replace at end of furnace tube
　　　a. Note: It is good to unscrew tubing from endcap and visually verify that nothing is clogging endcap
19. Open the inflow cap (by the wing nut) from glass tube
20. Use retrieval tool to slide quartz boat to end of tube and remove with large tweezers
21. If necessary, gently blow off particulate matter from samples using the nitrogen gun
22. Place samples on quartz boat
　　　a. Up to 8 IDEs can fit on the boat
23. Place quartz boat back into glass tube and position near center of tube with hole in boat toward the rear
　　　a. Note: Samples should be positioned about 1/4 before furnace thermocouple and 3/4 after thermocouple
24. Replace and tighten metal inflow cap on glass tube
25. Enter first setpoint temperature using digital gauge on front of furnace (750 °C)
26. Rotate mechanical valve to H_2 position (this allows flow of hydrogen and ethylene gases, while preventing flow of oxygen)
　　　a. This should only be done below 300 °C
27. Flow argon for at least 15 seconds, then turn off argon flow
　　　a. The argon MFC is broken so the argon must be turned on manually with the black dial on the argon line behind the furnace
28. Using left switch for hydrogen gas on MFC, select Manual (this will begin flow of hydrogen gas)
29. Ensure that bubbles begin to form in outflow beaker
　　　a. Note: If no bubbles are present, return MFC switches to Off position and inspect setup; make sure 3-way valve is set to (H_2) and that endcap was cleaned properly
30. Ensure that the ethylene valve behind the furnace (black dial, right side) is closed
31. Close and latch furnace lid (heating element will be activated)
32. Just before the set temperature is reached (747 °C), select Manual on left switch for ethylene gas on MFC then open the ethylene valve behind the furnace
　　　a. If trying to do a very short growth, open the valve before turning on the MFC so there is no pressure build up, which increases initial growth.
33. Start timer for growth
34. Once prescribed growth time is reached, select Off for ethylene gas on MFC (and close valve behind furnace)
　　　a. Typically, about 1 μm per second CNT height can be expected
35. Enter second setpoint temperature (900 °C) using digital gauge on front of furnace

36. Set the MFC to the desired flow parameters for CNT infiltration (hydrogen should still be flowing)
    a. Using right switch for each gas, select Set
    b. Dial in desired setpoint percent (see part e)
    c. Return right switch for each gas to Flow position
    d. For IDEs
        i. Hydrogen: Same as growth -- 311 sccm (currently 46.9%)
        ii. Ethylene: 193 sccm (lower than growth, currently 22.6%)
37. Once second setpoint temperature is reached, select Manual for ethylene gas on MFC and open the ethylene valve
38. Start timer for infiltration
39. Once prescribed infiltration time is reached, select Off for ethylene gas on MFC then close the ethylene valve behind the furnace
    a. Typically, 45 to 90 seconds for IDEs
40. Turn off the hydrogen flow by switching to off on the hydrogen MFC
41. Turn on the argon gas with the dial behind the furnace
42. Unlatch and open furnace lid to about a 45 degree angle until the temperature reaches 750 °C, after which the lid can be opened the remainder of the way
43. Cool furnace with fan starting at about 600 °C
44. Below 300 °C it is safe to remove samples
    a. Stop the argon flow
    b. Open and remove the front cap
    c. Use the retrieval tool to move quartz boat close to tube opening
    d. Use tweezers to carefully remove the boat (without touching it with your gloves)
        i. Note: Temperature of quartz boat is higher than that measured by thermocouple
    e. Slide samples off of boat
    f. Replace boat in furnace tube
    g. Slide boat to middle of tube
    h. Replace the front cap on the glass tube
45. Clean the tube by performing a burn-out process
    a. Rotate mechanical valve to Air position
    b. Ensure that no gases are flowing through tube by inspection of MFC and outflow beaker
    c. Select On for Air on MFC
    d. Close and latch furnace lid
    e. Carefully slide tube toward the front of the furnace, so that end cap is almost flush with back of furnace
    f. Once furnace temperature has reached 900 °C, allow about 1 min for burn-out
    g. Slide the tube to the opposite end (close to the front to remove entry particles)
    h. Return tube to normal, centered position
    i. Unlatch and open furnace lid all the way
        i. Note: If glass is not cleaned, continue burn-out process
    j. Allow furnace to cool by natural convection until 700 °C, after which the fan can be used to cool quicker
46. Allow furnace to cool below 250 °C

47. Turn off air MFC
48. Clean the end cap and tubing with acetone and IPA in the fume hood and replace at end of furnace tube
49. Turn on air MFC (to be left on while furnace is in standby)
50. Turn off furnace
51. Close and latch furnace lid
52. Reset ethylene MFC to standard conditions for next person (35.0%)
53. Turn off hydrogen, ethylene, and argon tanks in the sample prep room
    a. Loosen the regulator until loose
    b. Close the main tank valve
54. Write in growth log found at nano.byu.edu (under resources tab)

A.11 Oxygen Plasma Etch using PEII

1. Turn on vacuum pump
2. Turn on main power to PEII machine
3. Flip vent switch
4. Once vented, turn vent switch to off
5. Place sample in chamber, somewhat close to the center
6. Close lid and slowly open the roughing valve
7. Once pressure reads near zero on gage, turn on the O2 gas
    a. The ball on the meter should rise to about 10
8. Adjust power dial to 250 W
9. Turn on the generator power switch
    a. A purple/blue plasma should be visible thorugh the window
10. Start a timer
    a. IDEs are typically etched for 30 seconds (or longer for tall, close or heavy-infiltrated CNTs)
11. Turn off generator power switch
12. Turn off O2 gas switch
13. Close roughing valve
14. Turn on vent switch
15. Once vented, turn of vent switch and remove samples
16. Use a multimeter to check that resistance between contact pads is in the MΩ, preferably above the measuring capability of the multimeter (>40 MΩ)
17. If resistance is too low, repeat etching process for an additional 30 seconds
    a. Note that some devices may be shorted and will never reach above kΩ resistance
18. Close the lid and slowly open the roughing valve
19. Once the gage reads near zero, close the roughing valve.
20. Turn off the main power.
21. Turn off the vacuum pump

A.12 Static Pt Deposition onto CNT-MM

1. Note: Latex, or Nitrile gloves, should be worn for all following steps

2. Place chemical weighing boat on Mettler AE 240 Balance and tare
3. Ensure that the boat is centered on the scale
4. Weigh each carbon (C) sample and record mass
5. Note: combined mass of carbon samples in deposition will dictate Pt-C weight percent (% [w/w] Pt-C)
6. Weigh out chloroplatinic acid using Teflon-coated spatula
7. 30.0 mg is the standard target mass
8. The chloroplatinic acid will become "wet" over time, so limit the exposure to air, especially the contents inside the bottle
9. Suction required volume of ultrapure water into syringe (18.0 mL)
10. Use impinging jet from syringe to rinse chloroplatinic acid from weighing boat into empty 50 mL beaker
11. Suction required volume of formic acid (HCOOH) into syringe (2.0 mL)
12. Dispense formic acid into beaker
13. If desired, a calibrated pH meter may be used to measure pH of solution
14. Note: Sodium Hydroxide additives can be used to increase pH for variation in deposition time and resultant Pt morphology
15. Use tweezers to dip a Teflon stand into solution and gently stir
16. The Teflon should bubble when initially submerged
17. Remove Teflon stand and slightly dry with Kimwipes
18. Carefully secure CNT filter structure in Teflon stand and place in beaker
19. Close beaker opening using Parafilm sheet
20. Allow time for deposition to occur
21. Note: Deposition process is finished once amber-like colored solution becomes clear (about 12-18 hours typically)

A.13   Fluorescence Microscopy with Olympus FluoView FV1000

Information about the fluorescent microscope can be found at https://confocal.byu.edu/. The microscope operates through the Department of Physiology and Developmental Biology under the direction of Dr. Michael Stark and is located in room 3057 of the Life Science Building.

1. Turn on all of the machines in the order which they are labeled (1 through 7)
2. Log into computer and open the Fluoview software (FV logo)
3. With the magnification set at 4x and sample holder pushed all the way closed, place the VACNT device face down on the holder, supported at the edges, without a cover glass
4. Use the joystick to move the stage to approximately line up the device with the microscope lens
5. Select the dye such that the correct lasers will be used
    a. Dye: Alexa 405 (uses 405 nm laser) good for Atto 425 streptavidin
    b. Dye: Alexa 568 (uses 568 nm laser) good for Atto 568 biotin
6. Set the parameters as follows:
    a. Laser percentage: 12%
    b. HV (intensity): 750
    c. Gain: 1
    d. Offset: 6

e. Aperture: 200
7. Start the laser and adjust the stage height to find the sample
8. Change magnification to 10x or 20x to better view the sample
    a. Note that at 20x the lens can bump into the sample or sample holder and should not be brought too close to the wall edge
9. For tall VACNTs, the focal plane will need to be adjusted to view the top of the structure versus the substrate
10. Capture the desired image and export as TIFF
11. Return magnification to 4x and remove sample
12. Turn off all devices starting at 7 and going down to 1, except the laser (turn keys only) which needs to cool for a couple minutes before turning off.

A.14 Cyclic Voltammetry and Electrochemical Impedance Spectroscopy

1. Make a testing solution that is 5 mM ferricyanide, 5 mM ferrocyanide, and 100 mM KCl in 1X PBS (typically stored in a 15 or 50 mL test tube)
2. Connect the working (green) electrical lead from the CHI 660e potentiostat to one of the micro-manipulation probe leads
3. Connect both the counter (red) and the reference (white) electrical leads from the potentiostat to the lead of another micro-manipulation probe
4. Using a multimeter, verify that the electrical resistance across the contact pads of the IDEs is sufficiently large (typically greater than 40 MΩ)
5. Using tweezers, press a small rolled piece of parafilm over the electrical leads (between the VACNTs and the exposed contact pads) to contain the solution droplet close to the IDEs
6. Remove the parafilm and verify that a thin barrier layer has formed on the wafer
7. Set the IDE contact pads underneath the micro-manipulation probes to connect the IDE to the potentiostat
8. Turn on the power to the CHI 660e potentiostat (electrochemical analyzer)
9. Open the CHI66e Electrochemical Workstation program on the computer
10. Select the technique button (the "T" in the top menu).
    a. If already previously saved, open a past experiment to expedite the next steps
11. For cyclic voltammetry (CV), select "CV – Cyclic Voltammetry" and then set the following parameters:
    a. Init E: 0.6
    b. High E: 0.6
    c. Low E: -0.6
    d. Final E: 0.6
    e. Initial Scan Polarity: Negative
    f. Scan Rate: 0.15 to 1.25
    g. Sweep Segments: 6
    h. Sample Interval: 0.01
    i. Quiet Time: 0
    j. Sensitivity: 0.001
    k. Bottom options: unchecked
    l. iR compensation (separate button on menu): have "iR compensation for Next Run" box checked, select Always, select Manual, and input the resistance obtained from running EIS at high frequencies (the resistance of the electrical leads)
12. For electrochemical impedance spectroscopy (EIS), select "IMP – A.C. Impedance" and then set the following parameters:

a. Init E: 0
b. High Frequency: 1e5
c. Low Frequency: 0.1
d. Amplitude: 0.01
e. Quiet Time: 1
f. Sensitivity Scale Setting: Automatic (checked)
g. Measurement Mode Above 100 Hz: Single Freq. (selected)
h. Avrg/Cycles: 2 (for each frequency range)
i. Points/Decade Freq: 6 (for each frequency range)
j. Bias DC Current During Run: Off
13. Using a micropipette, dispense 50 µL of ferricyanide solution onto the VACNT IDE fingers
14. Start the experiment by pressing the Run button (black triangle); the time remaining in the experiment will be shown in the top right
    a. Note: start the experiment soon after placing the droplet to reduce the effects of evaporation; the solution droplet should be replaced between each experiment
15. Once the experiment is complete, press the Data Plot button
16. Save the data to the group folder on the J drive as both *.bin and *.csv files
    a. Save the *.bin file before starting the next experiment or the data will be lost
17. Remove the IDE from underneath the contact probes and gently spray a stream of ultrapure water to rinse the fingers
18. Place a 50 µL droplet of PBS onto the VACNTs when the electrodes are not in use to prevent the fingers from drying out and potentially peeling off the substrate
19. Proceed with the functionalization of streptavidin or binding of biotin
20. After soaking in a PBS droplet for the required time, gently rinse with a stream of ultrapure water and then shake off the excess water
21. For the next experiment, place the droplet of ferricyanide solution onto the VACNTs before the water completely evaporates from the electrodes and then begin the experiment
22. Compare different data sets by selecting New Overlay Plots in the Graphics tab and opening a previously saved experiment (or several experiments)
23. To obtain the peak current and voltage from CV, go to manual results and draw a line extending from the baseline current at the same slope
    a. Accuracy can be improved by having a higher sampling rate during CV or by interpolation (under the Data Processing tab)
    b. To measure different segments, plot only the desired segment under Graph Options (segment range)
    c. Ensure that the curser is set to free (not locked to data points) or a line will not be formed
24. Typical procedure:
    a. EIS (to obtain ohmic resistance)
    b. CV (at different scan rates)
    c. EDC/NHS
    d. 20 minute PBS soak
    e. EIS
    f. Streptavidin soak
    g. 40 minute PBS soak
    h. EIS
    i. 1 minute PBS soak
    j. EIS
    k. Biotin soak (at different concentrations)
    l. EIS
    m. 1 minute PBS soak
    n. EIS

APPENDIX B. SIMULATED CONCENTRATION PROFILE WITHIN VACNT MICROCHANNEL

Computational fluid dynamic (CFD) analysis was performed with COMSOL to estimate the mass transfer behavior within VACNT microchannels. Figure B-1 shows the concentration profile for a 100 µM solution flowing through a 16 µm diameter channel (250 µm long) at three different flow rates with corresponding average velocities of 1.7, 3.4, and 6.8 mm/s. The 3.4 mm/s average velocity corresponds to a 6 mL/min flow rate in the large flow cell, which was the flow rate used in much of the analysis of hydrogen peroxide and glucose. At 3.4 mm/s, the model predicts complete detection of the species by the end of the microchannel, but at 6.8 mm/s, the model estimates that some the species would not react before reaching the end of the microchannel. Thus, for complete detection at higher average velocities, either longer microchannels or smaller channel diameters would be needed, such as the 4 µm diameter channels used for comparison with hydrogen peroxide. Experimental data with hydrogen peroxide did not show any advantage with 4 µm diameter channels at moderate flow rates, but at higher flow rates the better mass transfer would likely help react more of the species. For simplicity, the model used a solid wall (although VACNTs would have a porous wall) with a wall concentration of zero (assuming all of species can react when contacting the wall).
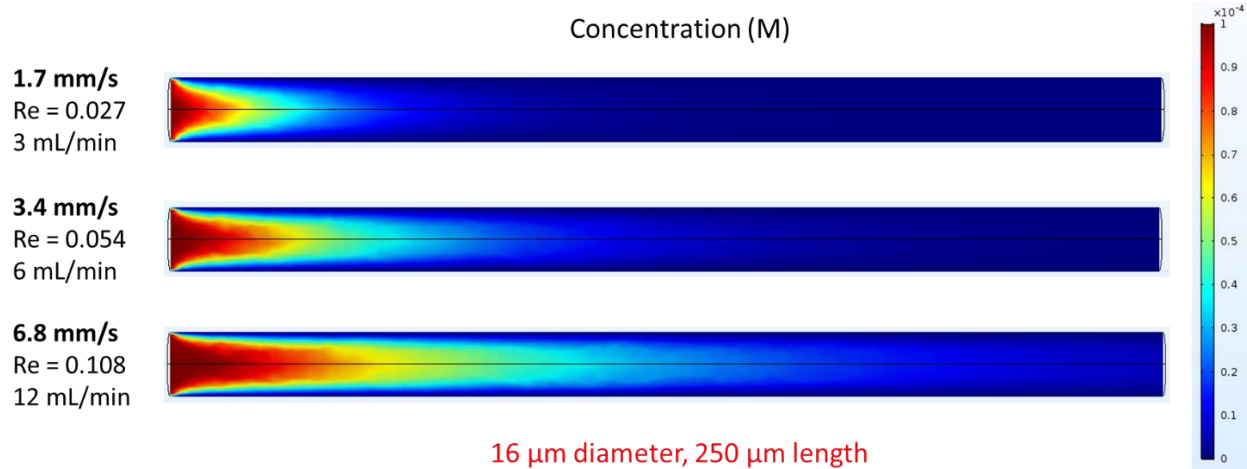
Figure B-1: Simulated concentration profile (100 µM inlet) within a VACNT microchannel (16 µm diameter, 250 µm length) at three flow rates with corresponding average velocities of 1.7, 3.4, and 6.8 mm/s.

APPENDIX C.   FLUID VELOCITY IN STIRRED BEAKER

The rotational flow of liquid in a beaker caused by a magnetic stir bar can be modeled by theoretical vortices. A solid-body rotation assumes that the entire fluid acts as a solid-body and the velocity profile is,

$$V_\theta = \omega r$$

where V_θ is the tangential velocity, ω is the angular velocity and r is the radius. This assumes that velocity increases linearly with radius, as is illustrated in Figure C-1A. An irrotational or free vortex is an ideal vortex given by,

$$V_\theta = \frac{\Gamma}{2\pi r}$$

where V_θ is the tangential velocity, Γ is the circulation and r is the radius. This vortex varies inversely proportional to the radius, resulting in a velocity that would approach infinity near the axis of rotation (Figure C-1B). The Rankine vortex is a combination of the solid body rotation vortex and the irrotational vortex,

$$V_\theta = \begin{cases} \dfrac{\Gamma r}{2\pi r_o^2} & r \leq r_o \\ \dfrac{\Gamma}{2\pi r} & r > r_o \end{cases}$$

where r_o is the radius of maximum velocity and V_θ, Γ, and r are the same as previously defined. This combination of profiles is illustrated in Figure C-1C. The Lamb-Oseen vortex is the exact

solution to the Navier-Stokes equations, providing a smooth and continuous equation for the velocity profile that is illustrated in Figure C-1D.

$$V_\theta = \frac{\Gamma}{2\pi r}\left(1 - \exp\left(-\frac{r^2}{r_o^2}\right)\right)$$
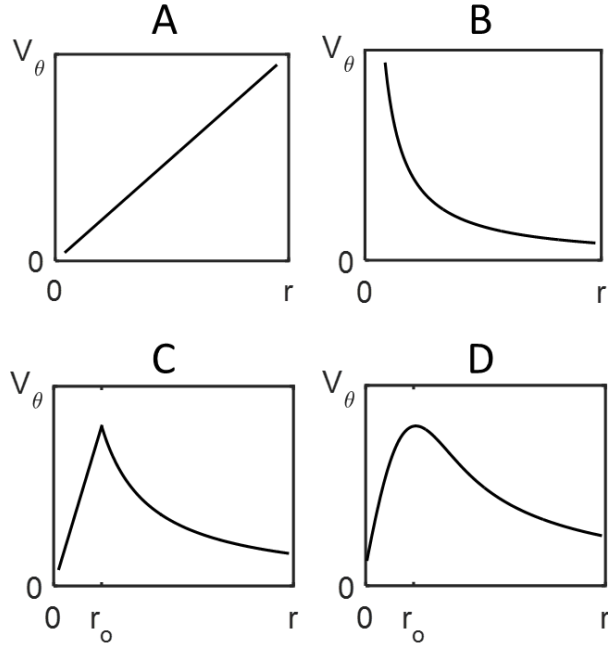

Figure C-1: Representative plots of the tangential velocity profiles from various theoretical vortices. (A) Solid-body rotation vortex. (B) Irrotational vortex. (C) Rankine vortex. (D) Lamb-Oseen vortex.

The velocity profiles were experimentally estimated with low-cost PIV using the test setup in Figure C-2A. A 50 mL beaker (which has an inner diameter of 39 mm and a height of 54 mm) held 48 mL of ultrapure water that was seeded with a small amount of titanium dioxide (TiO_2) powder, which enabled the flow visualization during the experiments. The seeded water came to a height of about 43 mm from the bottom of the beaker. A Kodak Carousel 760H slide projector was used as the light source, with the end of the lens being placed about 35 mm from the edge of

the beaker. A Sony DSC-RX100 IV high speed camera was positioned directly over top the beaker, perpendicular to the slide projector. The end of camera lens was about 50 mm above the top surface of the beaker. A Thermo Scientific Super-Nuova stir plate provided the driving force to magnetically stir the fluid with a 25 mm long and 8 mm diameter stir bar at the bottom of the beaker.
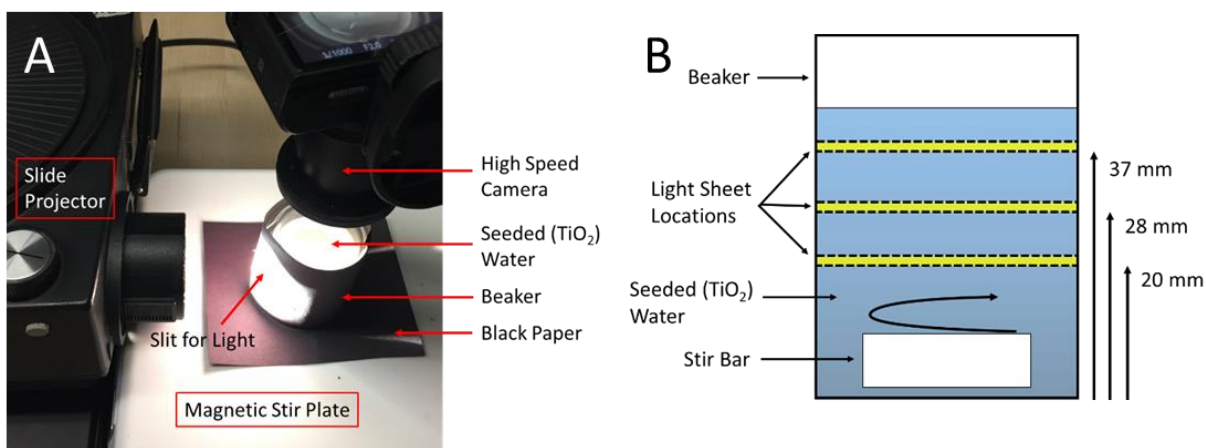

Figure C-2: (A) Experimental setup of continuous-light PIV with a magnetically stirred flow in a beaker. (B) Schematic of beaker used in experimental set up showing the sheet of light locations (approximately to scale).

The amount of light entering the beaker was restricted by wrapping the beaker in a thick black paper that had a 1.5 mm horizontal slot cut-out at 20, 28, and 37 mm (one slot at tested at a time) from the bottom of the beaker as shown in Figure C-2B. This ensured that a horizontal sheet of light was formed and only the particles of interest were illuminated in the beaker. A stir speed of 200 rpm was investigated.

The average velocity fields (over 897 image pairs) for a light location of 37 mm are shown in Figure C-3A. The directional velocity component is overlaid on top of a color map of the overall magnitude of the velocity to allow for easier visualization of the flow field. A white circle on each

image shows the approximate location of the beaker walls and a dashed red line on each image indicates the approximate location below which velocity data could not be trusted. The fluid velocity is nearly zero at the center of the vortex and then increases to a maximum velocity before decreasing back down to zero at the beaker wall (from no-slip conditions at the wall). Theoretically, the vortex would be symmetrical, but due to variations in the stir bar location and in the spinning of the stir bar itself (along with normal experimental error) this was not always the case from the experiment.

The centerline (horizontal) absolute velocity profile is shown in Figure C-3B. Also plotted is the expected velocity of the solid-body rotation of the stir bar (red line on plot). The experimental data very closely approximates the both the shape and magnitude of the solid-body rotation of the stir bar for the inner core of the vortex. The curvature of the profile between the max velocity and the wall resembles an irrotational vortex. The overall velocity profile is fairly close to the Rankine vortex or the Lamb-Oseen vortex.
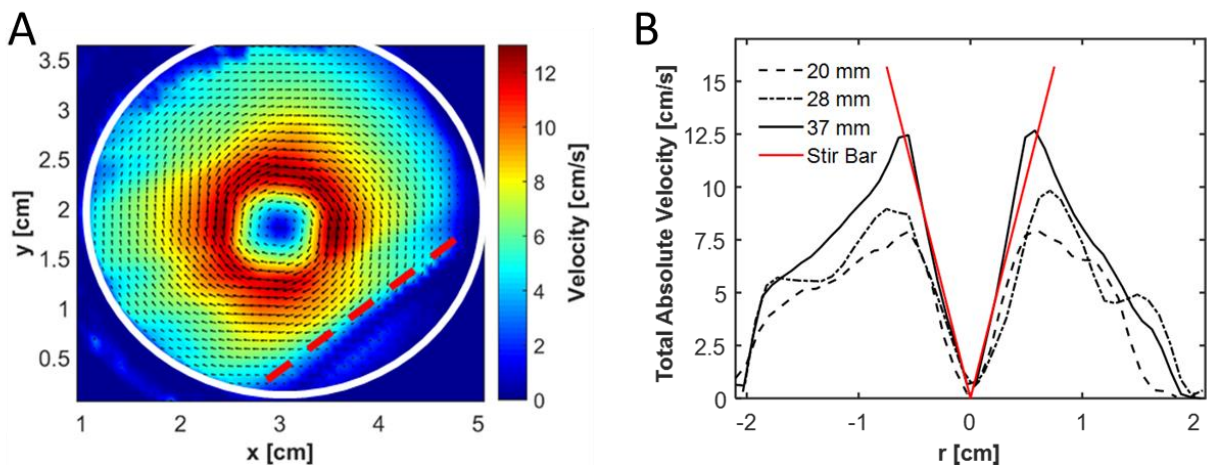

Figure C-3: (A) Velocity field for 200 rpm with sheet light heights of 37 mm. The white circle represents the beaker wall and the red dashed line indicates a region of poor light. (B) Velocity profiles along the centerline of velocity field and the expected solid-body rotation of the stir bar.

APPENDIX D.   SUPPLEMENTARY/SUPPORTING INFORMATION

D.1   Improving Sensitivity of Electrochemical Sensors with Convective Transport in Free-Standing, Carbon Nanotube Structures

Platinum (Pt) was important to the oxidation of hydrogen peroxide at the CNT electrode. Devices without Pt had a very low response with <2% of the measured oxidation rate of PN-CNT sensors at 100 µL s^{-1} (see Figure D-1).
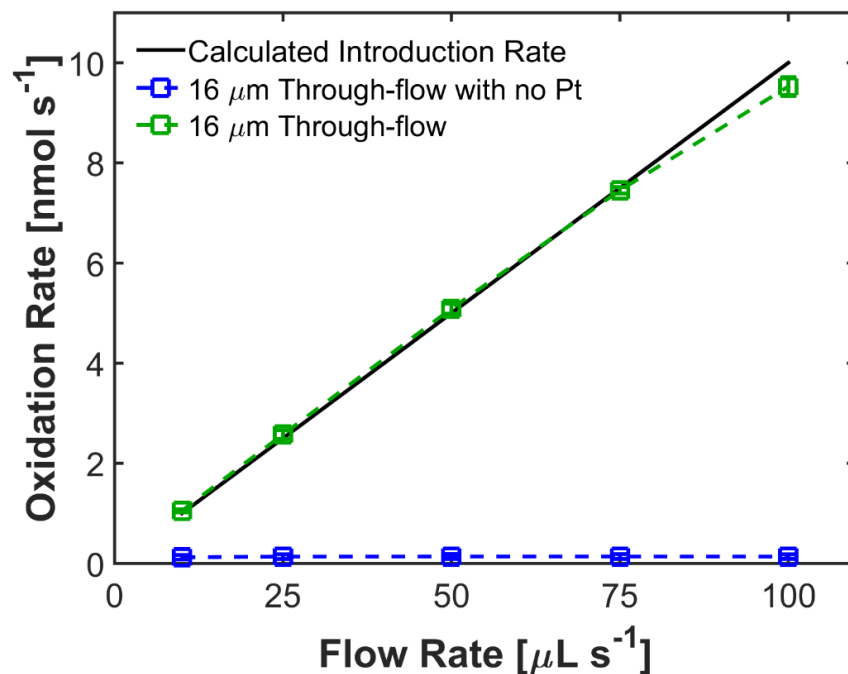

Figure D-1: Through-flow oxidation rates in response to 100 µM H$_2$O$_2$ at different flow rates for 16 µm diameter channels with and without Pt are compared to the calculated introduction rates of H$_2$O$_2$.

D.2 3D Interdigitated Vertically Aligned Carbon Nanotube Electrodes for Electrochemical Impedimetric Biosensing

Cyclic voltammograms for each of the VACNT electrode geometries are shown in Figure D-2. The IDE curves transition to a sigmoidal shape at 150 mV/s, while the SE curve still have a slight peak at 150 mV/s, indicating that the SEs do not have the same effectiveness as a microarray. Figure D-2D shows the CV data for a tall (80 µm), closely spaced ($w_g = 15$ µm) IDE, which has the highest peak current and the highest non-peak current, suggesting high surface area that was more effective than the $w_g = 25$ µm IDE.

Figure D-3 shows a representative Nyquist plot with the x-axis and y-axis on the same scale. By having the axes on an equivalent scale, the depression of the semi-circles is evident and the need to use CPEs in the equivalent circuit model is confirmed.

Figure D-4 shows a Nyquist plot of EIS data for a 5 µm tall VACNT IDE fit to three equivalent circuits. The traditional Randle's circuit is shown in the inset, where the W represents either the semi-infinite Warburg impedance and the finite-length Warburg impedance. The semi-infinite Warburg does not produce a semi-circular shape, but stays linear in the low frequencies on the right side of the plot, resulting in a poor overall fit. The finite-length Warburg element does provide curvature in the prediction but did not produce an overall good fit to the data. The data goes above the one-to-one linear slope produced by the Warburg elements from about 500 to 750 Ω on the x-axis, suggesting additional capacitive effects that are likely caused by the porosity of the VACNT electrode. To better fit the measured data, two CPEs each in parallel with a resistor were used to model the diffusive and capacitive behavior of the VACNT IDEs at low frequencies.
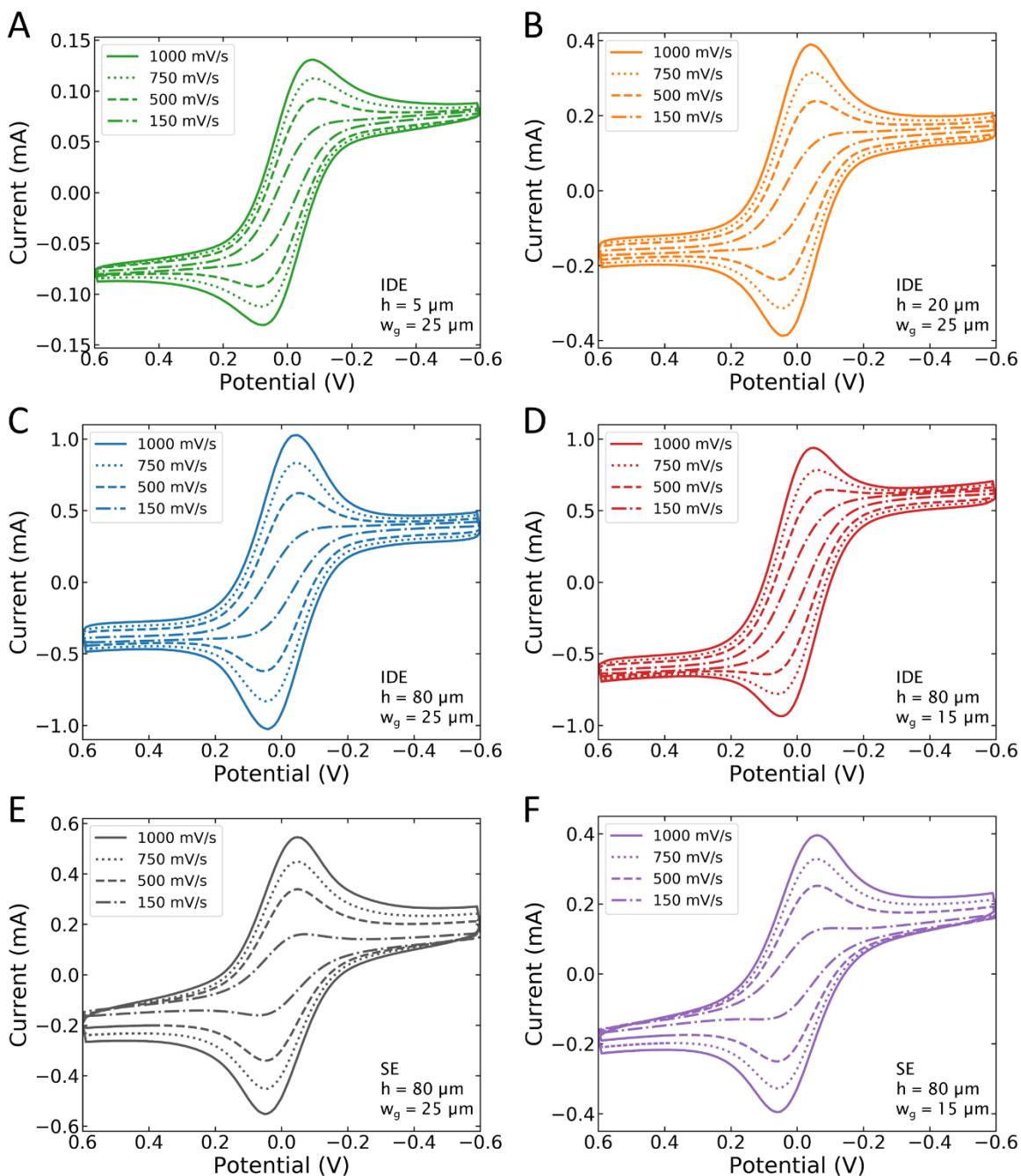
Figure D-2: Cyclic voltammograms of different VACNT electrode geometries in ferricyanide solution at scan rates of 1000, 750, 500, and 150 mV/s. (A) IDE, h = 5 µm, w_g = 25 µm (B) IDE, h = 20 µm, w_g = 25 µm (C) IDE, h = 80 µm, w_g = 25 µm (D) IDE, h = 80 µm, w_g = 15 µm (E) SE, h = 80 µm, w_g = 25 µm (F) SE, h = 80 µm, w_g = 15 µm.
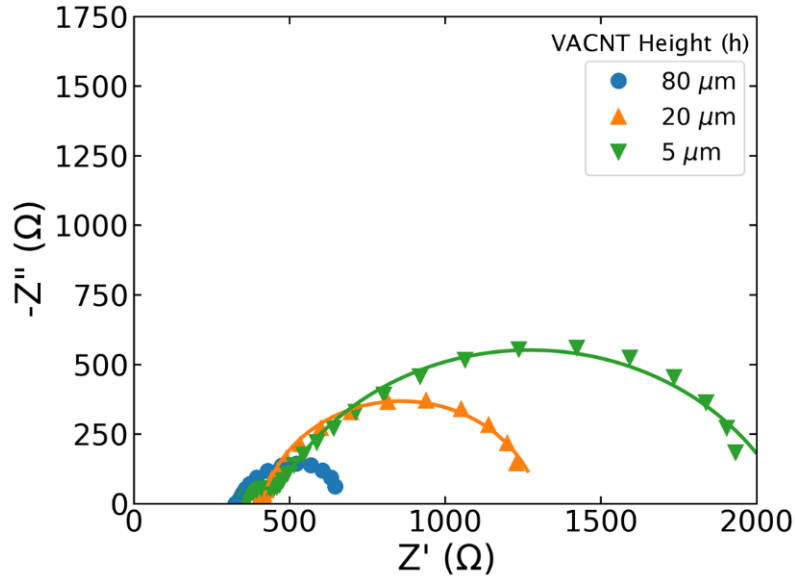
Figure D-3: Equivalent axes scale of Nyquist plots with experimental (markers) and simulated (lines) EIS data for VACNT IDEs ($w_g = 25$ µm) with heights of 80, 20, and 5 µm and no streptavidin/biotin.

Figure D-4: Nyquist plot of EIS data for a 5 µm tall VACNT IDE fit to three equivalent circuits: a traditional Randle's circuit (inset) fit with a semi-infinite Warburg element, a Randle's circuit fit with a finite-length element, and two CPEs each in parallel with a resistor.

The circuit element values of curve fit experimental EIS data for VACNT IDE heights of 5, 20, and 80 µm are shown in Table D-1. Signifi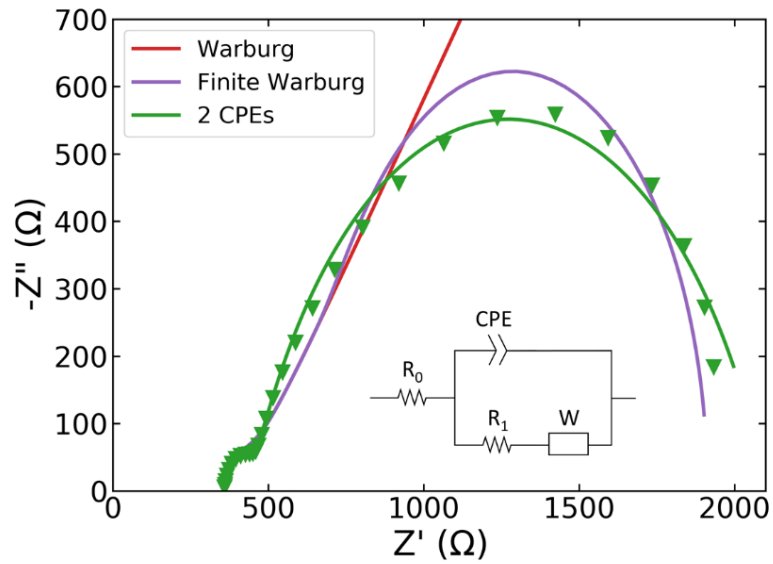cant changes in R_1, R_2, Q_1, and Q_2 were observed at different VACNT electrode heights. Note that the impedance of the constant phase element (CPE) has the form:

$$Z_{CPE} = \frac{1}{Q(\omega i)^n}$$

Table D-1: Circuit elements of curve fit experimental EIS data
for VACNT IDEs of 5, 20, and 80 µm.

Element	5 µm	20 µm	80 µm
R_0	359	396	329
R_1	85.1	16.6	8.6
R_2	1657	892	339
Q_1	6.30×10^{-6}	2.63×10^{-5}	3.15×10^{-5}
n_1	0.935	0.887	0.921
Q_2	0.00016	0.00036	0.00106
n_2	0.747	0.879	0.896

The 3D printed channel in Figure D-5 was printed with a resin-based Anycubic LCD Photon 3D printer. After rinsing the channels with isopropyl alcohol, the 3D printed part was further cured in UV light for 3 minutes. The resulting channel was clamped over the silicon chip, forming a 250 µm tall channel with the VACNT electrode protruding up to 80 µm into the flow. The sensor was accessed by probing the exposed chromium electrical leads.

Figure D-6A and B show fluorescent microscopy images of VACNT IDEs covered with fluorescently tagged streptavidin and biotin deposited in static conditions, as was the case for the results of this work. Figure D-6A and B can be compared with Figure D-6C and D, where the deposition of streptavidin and biotin were carried out under flowing conditions in the microfluidic

channel presented in Figure D-5. The flowing conditions produced brighter fluorescence, indicating better coverage of the fluorescent molecules on VACNT electrodes than static conditions. The microfluidic channel could potentially increase the sensitivity of the sensor and future work could implement and optimize flowing functionalization and binding.
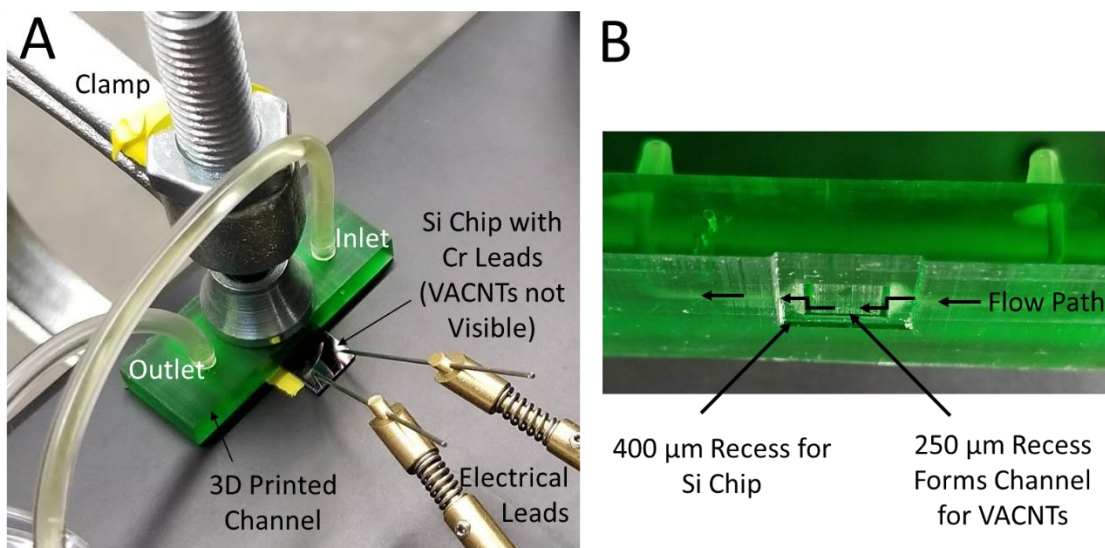

Figure D-5: (A) 3D printed microfluidic flow channel clamped over VACNT sensor with Cr leads remaining exposed for electrical contact. (B) Close up of channel design showing a 400 μm recess for the Si chip and an additional 250 μm recess that forms the microchannel for VACNT electrodes when clamped. The flow path is also represented.

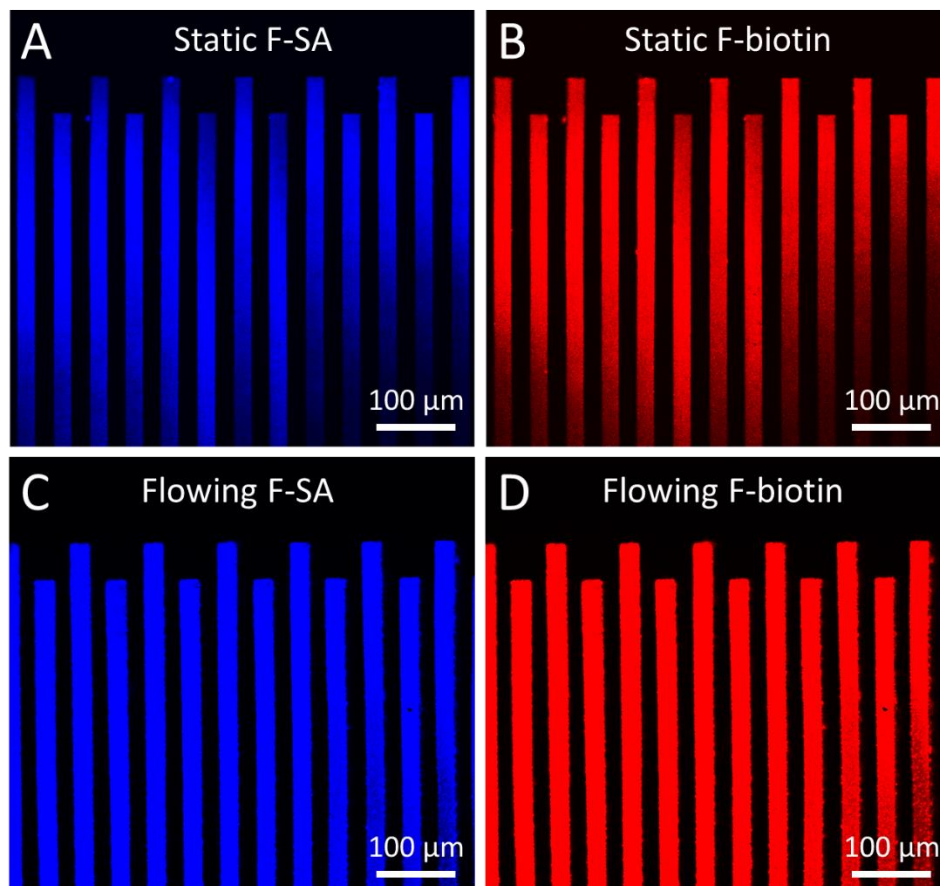Figure D-6: Fluorescent microscopy images comparing coverage of molecules bound to 80 µm tall VACNT IDEs by static and flowing depositions. (A) Static deposition of 500 µg/mL F-SA (blue). (B) Static deposition of 100 µg/mL F-biotin (red) bound to F-SA. (C) Flowing deposition of 500 µg/mL F-SA (blue). (D) Flowing deposition of 100 µg/mL F-biotin (red) bound to F-SA.

APPENDIX E.   DIFFERENCES BETWEEN INTERDIGITATED AND

SERPENTINE ELECTRODES

Interdigitated electrode (IDE) design is shown in Figure E-1A and serpentine electrode design in Figure E-1B. Each IDE finger is 2.95 mm long and 0.025 mm wide, with 0.025 mm spacing between each finger and 0.05 mm spacing at the electrode tip. Each IDE sensor has 61 total fingers that fit within a 3.025 mm x 3 mm area, and have a total design area of 4.50 mm^2. The odd number of fingers means that one electrode has 31 fingers and the other has 30 fingers, such that the red electrode in Figure E-1A has an electrode at the top and bottom of the sensor.

The serpentine sensors fit within the same 3.025 mm x 3 mm area and have a slightly higher total design area of 4.54 mm^2 because the spacing is 25 µm in all dimensions, unlike the IDE which has 50 µm spacing at the tips. If the IDEs fingers were 2.975 mm, the areas would be equal. Although the area is the same, the odd number of fingers in the design resulted in two consecutive fingers from the same electrode, as shown at the bottom of Figure E-2B. This may introduce an error up to 1.7% compared to having no consecutive fingers of the same electrode.
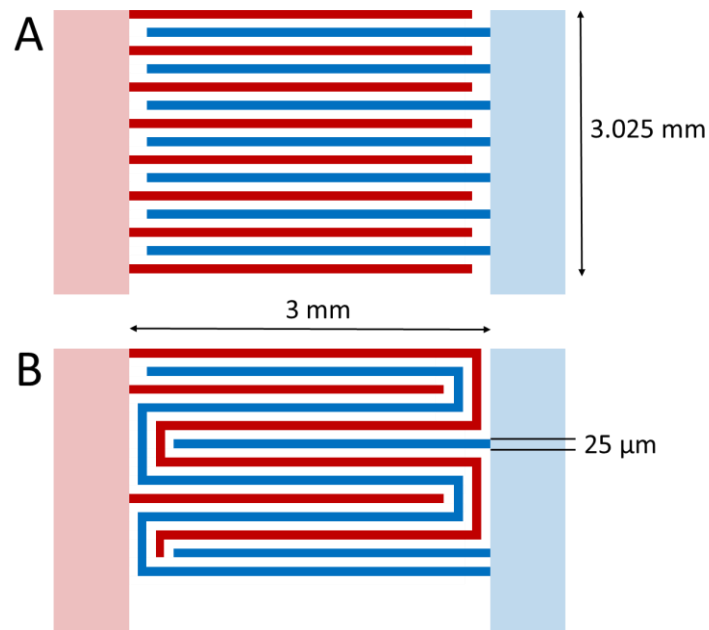
Figure E-1: Schematic of (A) interdigitated and (B) serpentine electrode designs. Red and blue distinguish the different electrodes in the sensor, with the dark colors representing VACNTs and light colors representing tungsten under alumina. Note that these are not to scale and do not show all fingers.

APPENDIX F.   CNT GROWTH STABILITY

The stability of CNTs on the silicon substrate is dependent on the ratio of the ethylene flow rate to the hydrogen flow rate during carbon infiltration. At higher ethylene flow rates, the stress induced during the infiltration causes the CNTs to be loosely connected to the substrate or come off all together. This is advantageous for the flow-through sensors because it allows for a simple way to remove the device from the substrate. However, with the IDEs it is important that the CNTs stay on the substrate so as to maintain constant spacing between the electrode fingers and to ensure that the fingers do not touch one another.

It was also observed that the location within the tube furnace during growth and infiltration also had an influence on the stability of the CNTs. The devices toward the front of the furnace were more stable than the devices further along the tube, as seen in Figure F-1. This is likely due to the temperature gradient along the tube. Near the center of the furnace the temperature is set to 900 °C, but the temperature of the gases would be lower before this point and higher after. The first device in Figure F-1 had one finger that slid out of place (on the far left of the image) after the oxygen plasma etch, signifying that there was still too much carbon being infiltrated.

To increase the stability of the CNTs, the ethylene flow rate during infiltration was lowered from the typical growth flow rate. The same effect would be possible by increasing the hydrogen flow rate, but the gas flow rates were already reasonably high, so lowering the ethylene flow rate made more sense than raising the hydrogen.
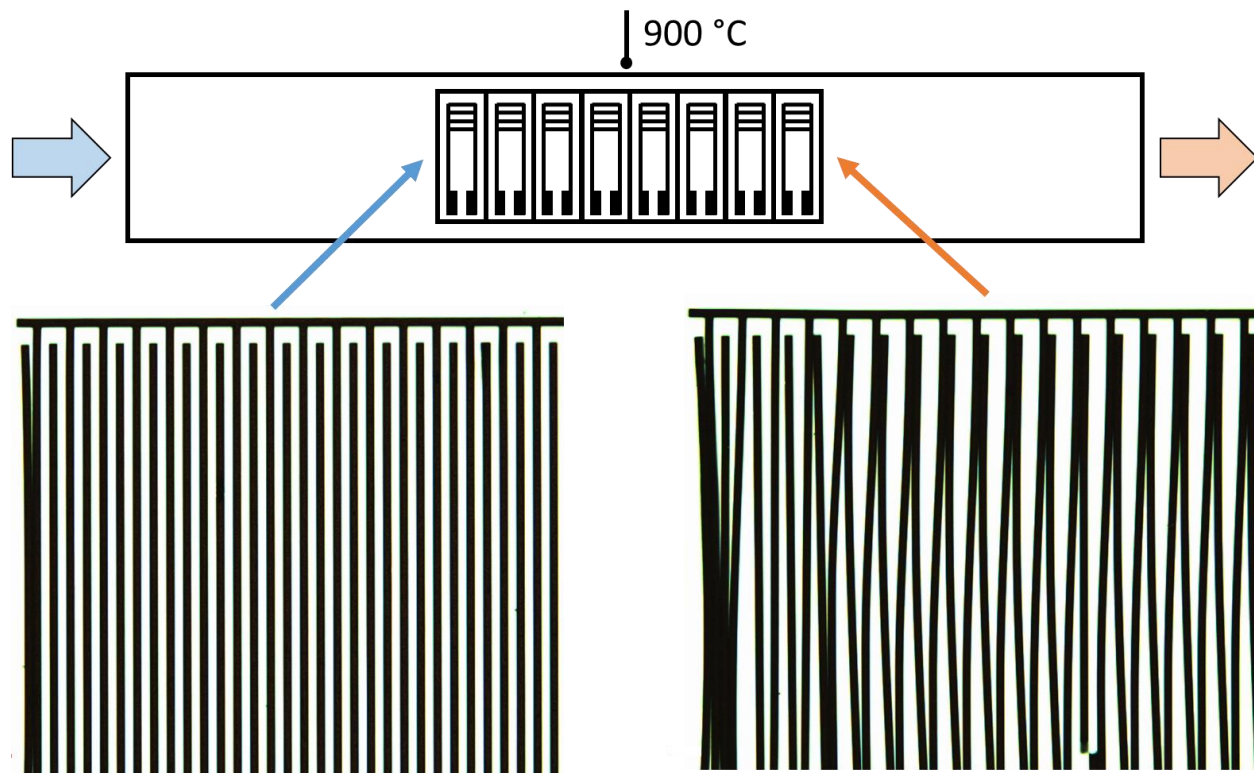
Figure F-1: Schematic of CNT growth furnace and the resulting microscope images of IDE devices after oxygen plasma etching. The IDEs at the front of the furnace were more stable than those toward the end.

One possible adverse effect of lowering the ethylene flow rate is that less carbon is added to the CNTs. One of the purposes of infiltrating is to increase the strength of the CNT structure. Thus, by having less carbon added, the structures themselves become more fragile, as was evident when the contact pads were probed with a multimeter. To overcome this challenge, the infiltration time was increased, but at a certain point the same problems started occurring again. Figure F-2 shows IDEs that were infiltrated for 3 minutes and 4 minutes (1.5 and 2 times longer than the previous 2 minute infiltration time). Both devices were at the end of the furnace and then oxygen plasma etched followed by an overnight soaking in PBS. The 3 minute devices remained

completely intact, whereas the 4 minute devices were disoriented. If a device remained intact after

soaking, usually it meant the device would be good for biofunctionalization.

It should also be noted that devices infiltrated at the lower ethylene flow rate did not require

the same length oxygen plasma etch to remove the carbon floor layer between the fingers (to make

them electrically insulated from each other). The reduction of etch time from 2 minutes to 45

seconds likely also increased the stability of the devices as the etching may have been caused the
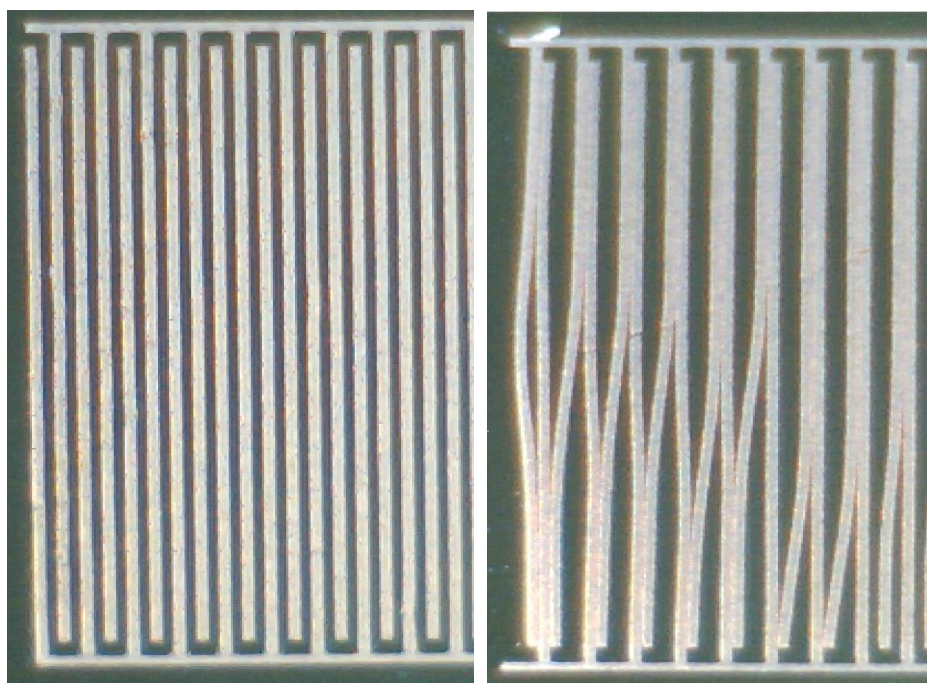
stability to decrease further.

Figure F-2: Microscope images of IDE devices after oxygen plasma etch and overnight soaking in PBS. Both devices were at the very end of the growth furnace tube (see Figure F-1). The device on the left was infiltrated for 3 minutes and the device on the right was infiltrated for 4 minutes.

APPENDIX G.   CNT SENSOR COST ANALYSIS

G.1   Material Costs

The cost per sensor before functionalization was determined by summing the lines in Table A-1. Before functionalization, the material cost per sensor was determined to be $0.80. This is based on 50 sensors per wafer, with the wafer contributing the most to the sensor cost. HMDS assumes using three 50 μL drops. Photoresist assumes 2 g for each coating, with each wafer coated 3 times. Photoresist developer assumes 50 mL per 5 wafers. Cost of photoresist and developer based on rates at microfab.ku.edu/rate-fees. Aligner lamp assumes life of 6 months being used 5 times per day. The amount of tungsten, alumina, and iron need for deposition was estimated from the hemisphere surface area of 75 cm radius using the material calculator at https://www.lesker.com/materials-calculators.cfm. Tungsten can deposit four wafers, alumina three wafers and iron one wafer per run. NMP was estimated to be 100 mL per 5 wafers. The iron boat and dicing blade were both assumed to last for 50 runs. A hydrogen cylinder was assumed to last 200 runs, with the historical log estimating 200 to 400 runs and theoretical of 1200 runs (using $V_{atm} = P_{cyl}*V_{cyl}/P_{atm}$ in combination with the flow rate). An ethylene cylinder was assumed to last 1000 runs, with the historical log estimating 500 to 1000 runs and theoretical of 3000 runs. An argon cylinder was assumed to last the same length as the hydrogen, as it is only used for cooling and hydrogen is used during heating and growth. The historical log was not an accurate representation because it is also used for an argon gun and likely contains leaks, but the theoretical

was 2000 runs. The oxygen cylinder for the plasma etch had negligible impact on the price. The nitrogen cylinder considers bringing vacuum systems back to atmospheric pressure, with the tungsten, alumina, and iron systems assuming a 200 L chamber filled twice. MES, EDC, and NHS each use 50 µL per device.

Table G-1: Cost per device of each material used in CNT sensor fabrication.

Item	Quantity	Cost ($)	Devices	Cost/device ($)
Oxidized Silicon Wafer	1 wafer	25	50	0.500
HMDS	1 L	285	300000	0.001
Photoresist	1 g	0.30	8	0.036
Aligner Lamp	1 lamp	372	50000	0.007
Photoresist Developer	1 g	0.01	5	0.002
Tungsten	3"x0.25"	333	18600	0.018
NMP	1 gal	148	9463	0.016
Alumina	100 g	100	7500	0.013
Iron	100 g	130	25000	0.005
Iron Boat	1 boat	75	2500	0.030
Dicing Blade	1 blade	10	2500	0.004
Hydrogen Cylinder	1 (2000 psi)	48	1600	0.030
Ethylene Cylinder	1 (1000 psi)	238	8000	0.030
Argon Cylinder	1 (2200 psi)	80	1600	0.050
Oxygen Cylinder	1 (2000 psi)	20	250000	0.0001
Nitrogen Cylinder	1 (2000 psi)	20	519	0.039
MES	5 L	144	100000	0.001
EDC	5 g	69	5208	0.013
NHS	25 g	42	43478	0.001

Total per device (no protein) = 0.796

Perhaps the most significant material cost is the protein or antibody that is being functionalized onto the VACNTs. As an example, for the protein streptavidin, costing about $100 per mg, it costs $2.50 per device if using 50 µL at 500 µg/mL. This cost can vary by protein and can be lowered greatly by using lower concentrations during functionalization.

G.2   Labor Time and Cost

The estimated time for each fabrication step for 4 wafers (200 sensors) is given in Table A-2. While processing multiple wafers, the process time is shortened per wafer. For example, the sputtering machine can process four wafers at a time and during lift off the wafers can all be sonicated at the same time. The longest process by far is the CVD growth of the carbon nanotubes. This is due to the fact that only 8 sensors can be processed each run, which takes about 90 minutes. The per device time of fabrication was calculated to be 17 minutes, with 65% of that time going toward VACNT growth. If a full-wafer furnace were used, this time would be shortened considerably. At \$12/hr, labor costs \$3.40 per sensor. Thus, under current conditions the total cost per sensor, including material and labor, is \$6.70.

Table G-2: Labor per fabrication process for 4 wafers.

Process	Time (min)
Photolithography	90
Tungsten	90
Lift off	60
Photolithography	120
Alumina	100
Iron	360
Lift off/Dicing	150
CNT Growth	2250
O2 Etch	20
Functionalization	200
Total (4 Wafers)	3440
Total per device	17

APPENDIX H. EIS SYSTEM CHECK

The procedures to check EIS system performance were obtained from the Gamry Instruments website (https://www.gamry.com/application-notes/EIS/quick-check-of-eis-system-performance/) and instructions are given here briefly.

1 kΩ Resistance Check

1. Obtain a resistor with approximately 1 kΩ resistance.
2. Connect working electrode to one side and the reference and counter electrodes to the other side of the resistor, keeping about 4 cm distance between clips.
3. Measure EIS spectrum using 20 mV amplitude and zero DC voltage from 0.2 to 1e6 Hz.

100 Ω Resistance Check

1. Obtain a resistor with approximately 100 Ω resistance.
2. Connect the working electrode to one side and the reference and counter electrodes to the other side of the resistor, placing the alligator clips as close to the resistor as possible, with the reference lead being placed between the resistor and the counter lead.
3. Measure EIS spectrum using 20 mV amplitude and zero DC voltage from 0.2 to 1e6 Hz.

10 kΩ Resistance Check

1. Obtain a resistor with approximately 10 kΩ resistance.
2. Connect the working electrode to one side and the reference electrode to the other side of the resistor, placing the alligator clips as far from the resistor as possible.
3. Connect the counter lead to the reference lead clip.
4. Measure EIS spectrum using 20 mV amplitude and zero DC voltage from 0.2 to 1e6 Hz.

Open Leads Test

1. Connect the counter and reference leads.
2. Separate the counter and reference leads at least 20 cm from the working lead.
3. Measure EIS spectrum using 50 mV amplitude and zero DC voltage from 0.025 to 1e6 Hz.

Shorted Leads Test

1. Connect all leads together.
2. Change the EIS setting to galvanostatic (instead of the typical potentiostatic, listed as single frequency in CHI program).
3. Measure EIS spectrum using 0.3 V amplitude and zero DC voltage from 0.1 to 10,000 Hz.

The magnitude of an ideal resistor remains constant with frequency and has a zero-degree phase shift. As seen in Figure H-1, the CHI system (A) had a non-neglegible shift in phase and impedance for all three resistors above 10^5 Hz, while the Gamry system (B) had little change in impedance and less than two percent change in phase. This suggests that CHI EIS measurements should only be run up to 10^5 Hz to avoid unwanted shifts in data.
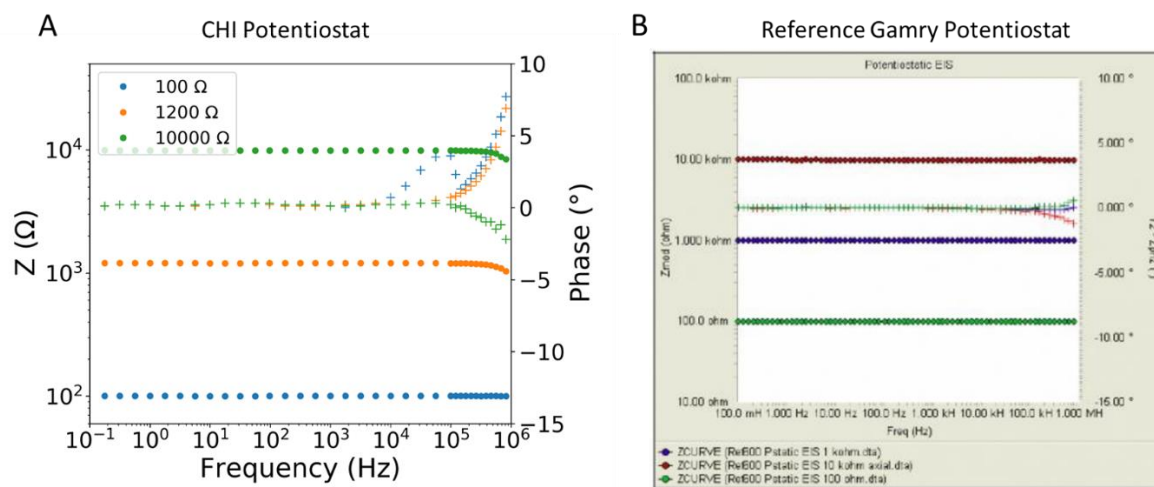

Figure H-1: Impedance and phase angle with frequency during EIS measurement for three separate resistances using A) CHI potentiostat and B) Gamry potentiostat. In both plots, circles represent impedance and crosses represent phase angle.

The highest impedance that the EIS system can measure is determined by the open leads test. The results for the open leads test are shown in Figure H-2. The reference Gamry system has approximately one order of magnitude greater impedance than the CHI system.
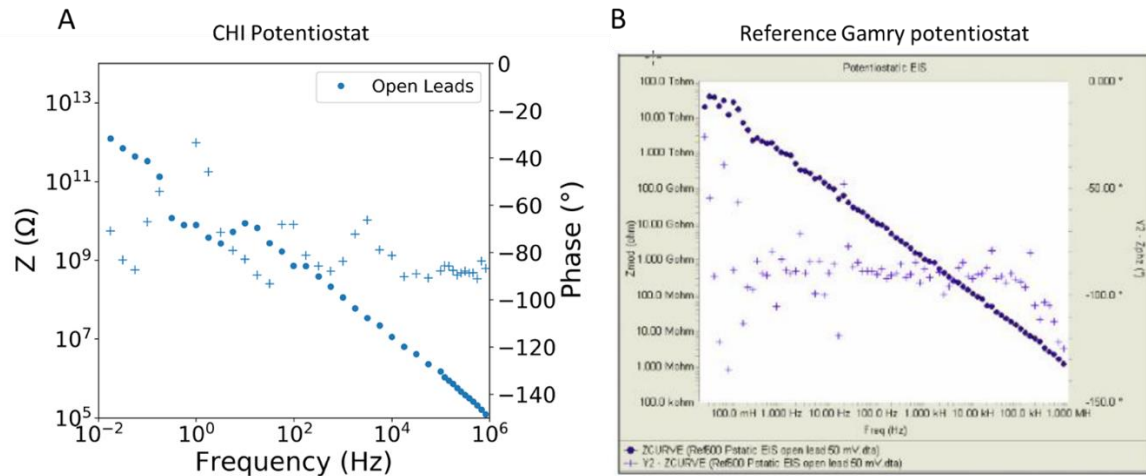
Figure H-2: Impedance and phase angle for an open lead system for A) CHI potentiostat and B) Gamry potentiostat.

The lowest impedance that an EIS system can measure is determined by the shorted leads test. A comparison of the CHI potentiostat and the Gamry potentiostat are shown in Figure H-3. The difference between the CHI and the Gamry potentiostats is larger for the shorted test than for the others system tests. While the impedance for the CHI is several orders magnitude higher than that of the Gamry, it is still below 1 Ω and is able to measure much lower impedance than the range of interest for the CNT biosensors.
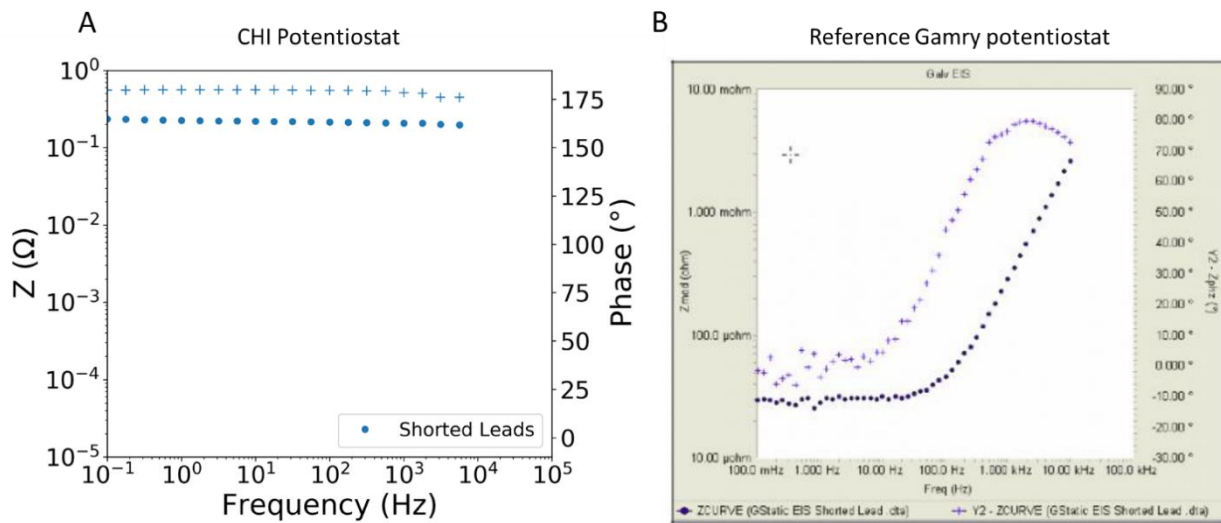
Figure H-3: Impedance and phase angle for a shorted lead system for A) CHI potentiostat and B) Gamry potentiostat.

APPENDIX I.   CIP2A DATA

Figure I-1 shows data from collaborative work done with Iowa State University [105]. VACNT IDEs were functionalized with anti-CIP2A and then incubated with increasing concentrations of CIP2A. The sensor was capable of sensing CIP2A across a wide concentration range from 5 pg/mL to 400 pg/mL in phosphate buffer solution and from 1-100 pg/ml in saliva supernatant (Figure I-1A). The gray shaded area in in Figure I-1A indicates the sensing range of a typical human CIP2A ELISA kit (0.156-10 ng/mL); the VACNT IDE sensing platform demonstrates higher sensitivity and a lower sensing range in both PBS and saliva supernatants than the corresponding ELISA. Nyquist plots of impedance measurements for the detection of CIP2A in saliva supernatant are shown in Figure I-1B, where the magnitude of each semi-circle on the left increased in magnitude with increasing CIP2A concentration. The linear CIP2A sensing range was calculated using linear regression analysis and is shown in Figure I-1C. Functionalized VACNT IDEs were also tested in saliva with increased incubation times (30, 45, 60, 90, and 120 mins) and increased BSA concentrations (0.5%, 1% and 2%), from which the impedance measurements indicated minimal interference and high stability in the complicated biological environment (see Figure I-1D). This implies the feasibility of applying VANTA IDEs toward early stage detection of oral cancers.
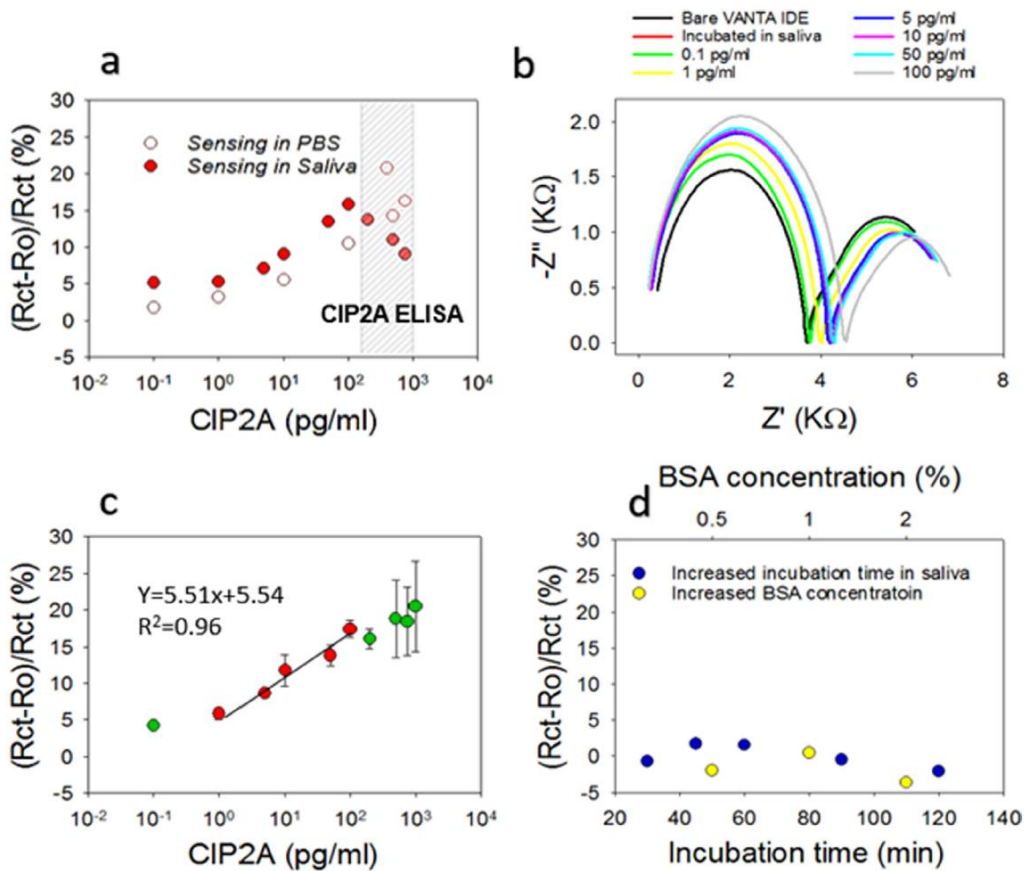
Figure I-1: CIP2A calibration plots with the anti-CIP2A VACNT IDEs. (a) Sequential CIP2A concentration increases in PBS and in saliva. The first data points are acquired as a baseline without CIP2A. Grey shaded region shows the sensing range of a typical human CIP2A ELISA kit. (b) CIP2A Nyquist plots acquired in saliva supernatant. The black (Bare VANTA IDE) and red (Incubated in saliva) lines are overlaid. (c) CIP2A calibration plots of anti-CIP2A functionalized VANTA IDEs tested in saliva. Four VANTA IDEs were tested and the standard deviations are plotted to indicate the repeatability and reproducibility (n=4). Regression analysis reveals the linear sensing range (red dots, between 1 and 100 pg/mL). (d) The anti-CIP2A functionalized VANTA IDEs were also tested in saliva with increased incubation times and increased BSA concentrations. Data and images from reference [105].